SAPIENZA
UNIVERSITÀ DI ROMA

FACOLTÀ DI INGEGNERIA CIVILE E INDUSTRIALE
Dipartimento di Ingegneria Meccanica e Aerospaziale
DOTTORATO DI RICERCA
IN MECCANICA TEORICA E APPLICATA
XXXII CICLO

Ph.D. Thesis

Advanced control algorithm applied to the Guidance Navigation & Control of complex dynamic systems

September 2019

Tutor:
Gianluca Pepe

Head Professor:
Antonio Carcaterra

Candidate:
Dario Antonelli

Clarence "Kelly" Johnson referring to the SR-71
"Everything about the aircraft had to be invented"

Wernher Magnus Maximilian von Braun
"I have learned to use the word 'impossible' with the greatest caution"

Elon Reeve Musk
"Persistence is very important. You should not give up unless you are forced to give up"

Anthony "Tony" Edward Stark interviewed by Christine Everhart
Ms. Everhart: "you've been called the da Vinci of our time. What do you say to that ?"
Mr. Stark: "Absolutely ridiculous. I don't paint"

"Dedicated to the Engineering Pioneers"

Index of contents

List of Figures

List of Tables

Abstract

In this Thesis a new Optimal control-based algorithm is presented, FLOP is part of a new class of algorithms the group of Mechatronic and Vehicle Dynamic Lab of Sapienza is developing under the name of Variational Feedback Controllers (VFC). The proposed method starts from classical optimal variational principles, usually part of the Pontryagin's or Bellman's methods, but it provides the user with the possibility to implement a feedback control, even in the presence of nonlinearities. In fact, even though Pontryagin approach provide the best solution for the considered system, it has an engineering weakness, since the identified solution is a feedforward control law.
The control program form of the solution presents an engineering weakness, that is they use only one single information on the system state: the initial condition. This approach would be natural if the system's model is not affected by any error, the state of the system is perfectly known, and all the environment forces are known in advance. Under these conditions, the system response for any future time depends only on the initial information provided by the initial condition. However, engineering practice and real world meet a different scenario. Models of the controlled process have some degree of approximation, because the real dynamics is only roughly represented by the estimated differential equations, and the environment external disturbance is generally unknown. In this context, use of measurements by sensors is of great value and feedback control strategies use the valuable support of measurements. Variation Feedback Control is aimed at using the power of variational functional calculus to state a well posed optimality principle, but using the information coming from sensors, integrating in this way the available information contained into initial conditions, the only one used in the context of control programs, providing a more reliable controlled system. This chance is obtained by changing the optimality principle used in the classical approach. FLOP approach, respect to classical nonlinear controls, such as Sliding Mode, Lyapunov and feedback linearization controls, presents a great advantage because of the chance of a more flexible specification of the objective function. In this work the FLOP algorithm is applied to define new techniques for Guidance Navigation and Control (GN&C) of complex dynamic systems. Autonomy requires as a main task to be able to self-perceive and define the best way to reach the desired part of the state space, in which the considered system moves by applying different strategies and modification of the applied algorithms to perform the task, whatever the considered dynamic system. Model based control techniques such as LQR, SDRE and MPC have the advantage of being aware of the system dynamics, but in general they present some drawbacks, in fact LQR and SDRE algorithms require linear dynamics or a linearized form of the real dynamics, as well as limitations in terms of penalty function, while MPC, in their nonlinear formulation namely NMPC, can deal with nonlinear dynamics and strong constraints, moreover they can introduce strong constraints for the system state as well as for the control actuation, the major drawback of these techniques is that the online optimization process requires a huge computational effort especially when the dynamics of the system is very complicated, or the system presents an high number of degrees of freedom, moreover time for convergence is strictly connected to the convexification of the considered cost function that has to be minimized, especially in presence of constraints in terms of the state and or of the control.
The present technique is applied in complex engineering applications, the autonomous car, an autonomous marine craft for rescue purposes, rocket landing problem, and finally to the control of a micro-magnetic robot, actuated by a Magnetic Resonance Imaging (MRI) for non-invasive surgery. will be discussed, this research projects are part of the activities developed by the group of Mechatronic and Vehicle Dynamic Lab of Sapienza.

Chapter 1

State of the art for control strategies

1.1 Overview of the control literature

Multiple human activities and devices require the "control" or "regulation" of some system's properties. For instance, the temperature control of a room as well as in an industrial production process, the autonomous control for terrestrial, marine, and aerospace vehicles, and the control of Financial trading. Control theory is concerned with mathematical models of physical or biological systems of this kind.
Control systems are usually classified in different ways, one preliminary classification can be done considering "feedforward" or "open" loop control strategies and "feedback" or "closed" loop control strategies [1-8].
In open-loop systems we wish to provide, in advance, to the system the proper sequence of control inputs that will generate the desired output of the controlled variable. This means that the control strategy will not take into the account the actual behavior of system, or the so called Plant, disregarding any measurements coming from the sensors, this approach holds under the unrealistic assumptions, that the model which describes the dynamic of the Plant is perfect, and that no disturbances affect the evolution of the controlled variable. However, reality meats a different scenario, in fact models are always an approximation of the real system, and disturbances are not known a priori. Therefore, the feedforward approach is affected by an engineering weakness and results to be non-effective if directly applied to the system.
Instead in the closed-loop of feedback formulation, the control algorithm is evaluated iteratively at each loop, in the basis of the actual state of the system, i.e. taking into the account the estimation of the controlled variable, obtained applying sensor estimation algorithm to the data provided by the sensors as shown in Fig. 1

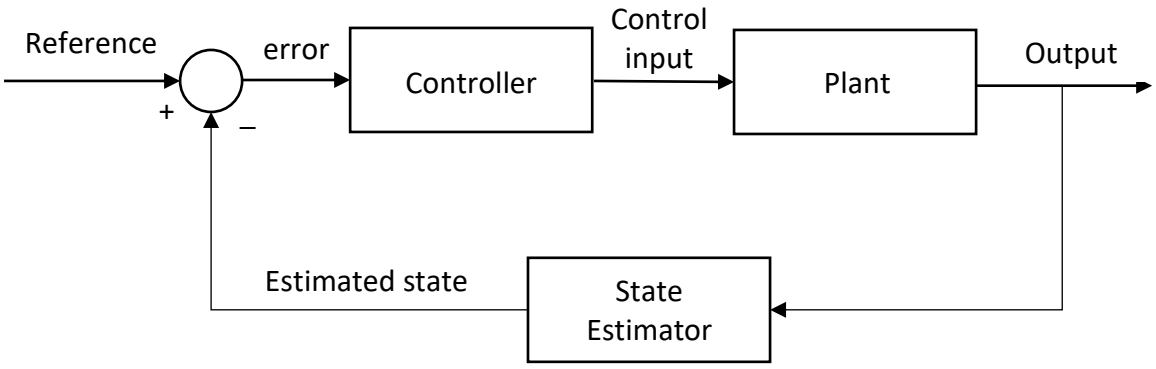

Figure 1: Feedback or closed-loop control scheme.

The aim of the Controller block is to generate a control input to reduce the error between the measured output of the Plant and the reference signal provided by the user [1-8]. The controller will guarantee

the desired response of the system if the overall controlled system is stable [1-8], and therefore stability is a mandatory property for the system.
Several control techniques have been developed through the years, with different advantages and weakness, among these the controllers that belong to the class of the Optimal Control Theory are of great interest for the researchers, even though they were initially formulated during the 1950s.
The Optimal control theory applies mathematical tools to identify a control law for a dynamical system over a time horizon such that a performance index is optimized. It is widely used in several scientific fields as well as many Engineering applications.
Optimal control is based on the calculus of variations, this is a mathematical optimization technique, the origin of this mathematical tool is commonly associated to the brachistochrone problem (from Ancient Greek βράχιστος χρόνος (brákhistos khrónos) meaning 'shortest time'), posed by Johann Bernoulli in 1696.
The well-known mathematician asked to find the curve, lying in the vertical plane between a point A and a lower point B, where B is not directly below A, on which a frictionless bead slides under the influence of a uniform gravitational field to a given end point in the shortest possible time.
The method has been applied for deriving control policies [9-16] thanks to the work of Lev Pontryagin and Richard Bellman in the 1950s, after contributions to calculus of variations [9,10]. The solution provided by the Optimal control theory can be used as control strategy in control theory.
As stated in [11]:

"The objective of Optimal control theory is to determine the control signals that will cause a process to satisfy the physical constraints and at the same time minimize (or maximize) some performance criterion."

In other word, Optimal control deals with the problem of the proper control law, i.e. the proper sequence of inputs, for a given system, such that a certain optimality criterion is achieved. A control problem includes a cost functional that is a function of state and control variables.
The optimal control statement is represented by the Hamilton-Jacobi-Bellman set of differential equations, obtained applying the variational calculus, these provide the paths for the control inputs that minimize the index of performance *J*

$$J = \int_0^T E(x,u) + \lambda\big(\dot{x} - f(x,u)\big)\, dt \tag{1}$$

Where $E\big(x(t),u(t)\big)$ represents the cost functions, and $\dot{x} = f\big(x(t),u(t)\big)$ the dynamic equations of the considered system. The control set can be identified using the Pontryagin's minimum principle [12-16], subject to the initial condition $x(0) = x_0$ and the terminal value for the Lagrangian multiplier $\lambda(T) = 0$, this is also known as two boundary conditions problem [12].
The solution provided by Pontryagin's minimum principle represents the optimal trajectory $x^*(t)$ and the associated optimal control set $u^*(t)$, however this is an open loop solution, known as control program technique. It is clear that a major drawback affects these techniques, in fact since they cannot rely on the sensors measurements and considering the model approximation and the unpredictability of the random disturbances that usually affect the system's dynamic, the optimal set of control $u^*(t)$ cannot be directly used as control input to the real system.
Several techniques to solve this weakness have been proposed, such as Linear Quadratic Regulator (LQR), State Dependent Riccati Equation (SDRE) and Model Predictive Control (MPC).

If the system dynamics are described by a set of linear differential equations and the cost is described by a quadratic function the problem is called LQ. In these cases, the solution for the controlled system is provided by the linear–quadratic regulator (LQR), this is a feedback optimal based controller.
The finite horizon, linear quadratic regulator (LQR) is given by [6]:

$$\begin{aligned} \dot{x} &= Ax + Bu \qquad x \in \mathbb{R}^n, u \in \mathbb{R}^m \\ J &= \frac{1}{2}\int_0^T (x^T Q x + u^T R u)\, dt + \frac{1}{2} x^T(T) P_1 x(T) \end{aligned} \tag{2}$$

where $Q \geq 0, R > 0, P_1 \geq 0$ are symmetric, positive (semi-) definite matrices. This can be solved applying the minimum principle which leads to:

$$\begin{aligned} H &= x^T Q x + u^T R u + \lambda^T (Ax + Bu) \\ \dot{x} &= \left(\frac{\partial H}{\partial \lambda}\right)^T = Ax + Bu \qquad x(0) = x_0 \\ -\dot{\lambda} &= \left(\frac{\partial H}{\partial x}\right)^T = Qx + A^T\lambda \qquad \lambda(T) = P_1 x(T) \\ 0 &= \left(\frac{\partial H}{\partial u}\right) = Ru + B^T\lambda \implies u = -R^{-1}B^T\lambda \end{aligned} \tag{3}$$

If one is now able to solve the two boundaries conditions problem obtains the optimal solution, but in general is not easy to be solved. Instead the LQR techniques proposes for the costate $\lambda(t) = P(t)x(t)$ which provide a solution using the Time Varying Riccati equation:

$$\begin{aligned} \dot{\lambda} &= \dot{P}x + P\dot{x} = \dot{P}x + P(A - BR^{-1}B^T P)x \\ -\dot{P}x - PAx + PBR^{-1}B^T Px &= Qx + A^T Px \end{aligned} \tag{4}$$

Simplifying the x, one obtains the Time Varying Riccati equation, the solution to this can be found using the terminal condition $P(T) = P_1$, even though is not easy:

$$-\dot{P} = PA - PBR^{-1}B^T P + Q + A^T P$$

The solution found for the control, is still time dependent $u = -R^{-1}B^T P(t)x$ which is undesirable, since its is not a feedback control. Otherwise if the time horizon is extended to $T = \infty$ the algebraic Riccati equation must be considered, i.e. $\dot{P} = 0$, the LQR technique provide an optimal feedback control law for the considered system and cost function:

$$u = -R^{-1}B^T Px \tag{5}$$

Even though the LQR provide an optimal based feedback control, this optimality is guaranteed only for linear systems, and quadratic cost functions. Different techniques can be used to introduce the nonlinearities of the considered model into the controller, such as approximation or numerical

schemes, that will produce a feedback control as close to optimal as possible. One direct formula for nonlinear systems is almost impossible to be formulated, therefore several suboptimal techniques have been developed, as well as the one that will be discussed throughout this work.
One chance to take into the account the nonlinearities of the controlled system, providing a suboptimal feedback control is represented by the SDRE technique, this is based on the algebraic Riccati equation, used to find the optimal solution for the LQR in the linear dynamic cases. The SDRE approach extends this method also to nonlinear dynamic systems by allowing the matrices involved in the Riccati algebraic equation to vary with respect to the state variables and possibly the controls as well [17-20]. The early work on the SDRE was done by Pearson [18] Garrand, McClamroch and Clark [19], Burghart [20] and Wernli and Cook [21]. More recent works on SDRE have been done by Krikelis and Kiriakidis [22], and Cloutier, D'Souza and Mracek [23].
This technique considers a system dynamic described by the affine system class:

$$\dot{x} = f(x) + B(x)u \tag{6}$$

Where state nonlinearities are present, and the control inputs depends linearly by the system state.
Wernli and Cook [10] introduced a more general case for the SDRE technique, i.e.:

$$\dot{x} = f(x, u) \tag{7}$$

Since dynamic system often exhibits nonlinearities also in terms of the control input, Wernli and Cook provided different techniques to deal with this more general class of systems, this can be done modifying the structure of the dynamic system rewriting it with constant and state dependent matrices and introducing a power series formulation as in [17-20].
A different approach is represented by introducing the control nonlinearities through a cheap formulation, i.e. introducing them into the state nonlinearities, by adding other differential equations which described the nonlinear dynamic of the actuators [23].
Another technique to introduce nonlinearities as well as more general penalties function is represented by the Model Predictive Control (MPC), also referred to as Receding Horizon Control and Moving Horizon Optimal Control. This approach was initially developed for the oil industries and has been widely adopted in industry because of its effectiveness and the ability to deal with multivariable constrained control problems, and nonlinear problems [24-29]. The origin of the MPC can be traced back to the 1960s [26], but the real interest for this technique started in the 1980s with the papers [27,28], The scheme of MPC is depicted in Fig. 2.
The idea behind the MPC is to use a model (Plant) to predicts the future behavior of the Process (real system), the output provided by the Process is used as actual condition of the system, while the predicted output produced by the Plant is used as feedback for the Optimizer, which performs an optimization process to determine which is the best control input to be applied to the Process to make it tracks the desired Reference. The control set determined by the Optimizer is applied according to a receding horizon philosophy: At time t only the first input of the optimal set of control is applied to the Plant. The other commands of the optimal set are discarded, and a new optimal control problem is solved at time t + 1. As new measurements are collected from the plant at each time t, the receding horizon mechanism provides the controller with the desired feedback characteristics.

The optimization process guarantees the optimality of the solution provided by the controller, at the cost of a high computational effort, especially when several constraints have to be respected and the Process exhibits a strong nonlinear behavior.

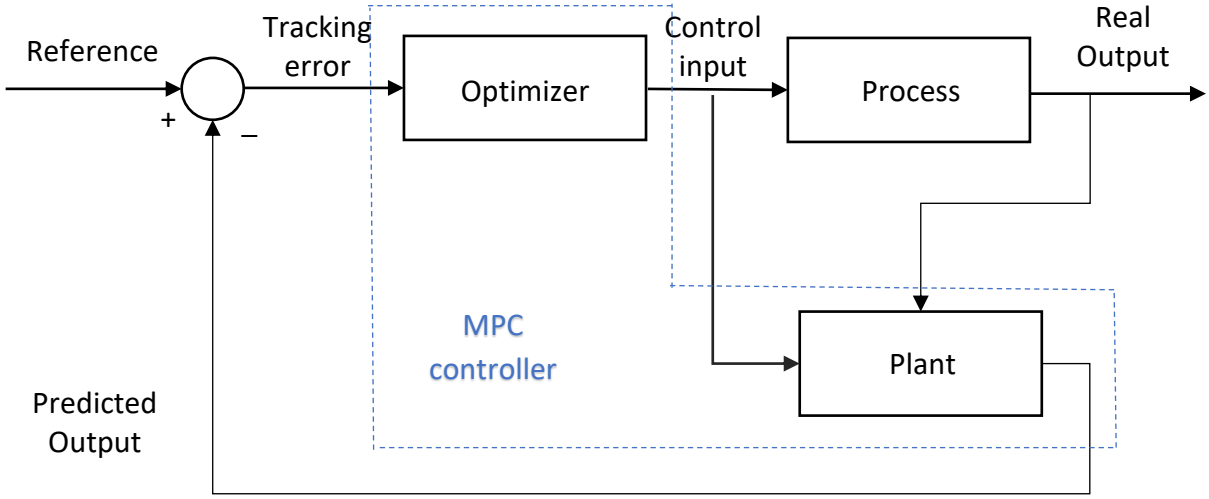

Figure 2: MPC controller.

Unmanned and autonomous vehicles, terrestrial, naval, and aerial, are one of the most active field of research of these days Fig.3, in fact this devices permits to reduce the action of the human in the vehicle control, with different degrees of autonomy, from basic systems that only support the human in controlling the vehicle, to advanced algorithms operating a complex set of actuators and sensors, with the aim to remove the human in the control loop.

Figure 3: Examples of autonomous vehicles, from the left top in clockwise sense, Roborace autonomous racecar, Lockheed-Martin SR-72 autonomous surveillance hypersonic plane, SpaceX Falcon heavy booster autonomous rocket landing, DARPA Sea-hunter autonomous marine vessel.

Four applications of the proposed control will be presented in this work, regarding, autonomous car, autonomous marine vehicle, rocket vertical landing and MRI actuated micro robots. The autonomous car idea is usually supported by the fact that human beings are poor drivers [30,31]. However, is not easy to design and build a perception-control system that drives better than the average human driver. The 2007 DARPA Urban Challenge [32] was a landmark achievement in robotics, when 6 of the 11 autonomous vehicles in the finals successfully navigated an urban environment to reach the finish line. The success of this competition generated the idea, that fully autonomous driving task was a "solved problem", and that it was only a matter of time, to have fully functional autonomous cars on our roads. Eventually reality faces a different scenario, in fact today, fifteen years later, the problems of localization, mapping, scene perception, vehicle control, trajectory optimization, and higher-level planning decisions associated with autonomous vehicle development is not still completely solved yet. In fact, the most advanced commercial vehicles still need a human supervisor responsible for taking control during periods where the AI system is "unsure" or unable to safely proceed remains the norm [31,32].

The history of model-based ship control starts with the invention of the *gyrocompass* in 1908, which allowed for reliable automatic yaw angle feedback. The gyrocompass was the basic instrument in the first feedback control system for heading control and today these devices are known as autopilots. The next breakthrough was the development of local positioning systems in the 1970s. Global coverage using satellite navigation systems was first made available in 1994. Position control systems opened for automatic systems for waypoint tracking, trajectory tracking and path following [53].

Complex, high-performance, high-cost rocket stages and rocket engines were usually wasted after the launch. These components fall back to Earth, crashing on ground or into the Oceans. Returning these stages back to their launch site has two major advantages cost saving, and reduction of the impact of space activities on the environment. However, early reusability experience obtained by the Space Shuttle and Buran vehicles enlighten all the difficulties of this task [54-59]. Therefore, rocket vertical landing represent an interesting and challenging test case for new control algorithms.

Untethered mobile robots have opened new methods and capabilities for minimally invasive biomedical applications [76-80]. The minimally invasive surgeries reduce the surgical trauma, leading to fast recovery time and increase in the comfort of patients. However, surgeons have no direct line-of-sight at these operations, and therefore, such opera- tions require an intraoperative medical imaging modality to monitor the state of the surgery deep in the tissue. Without such feedback information, the surgeon would not have visual feedback and could not continue the operation safely and reliably.

Chapter 2

FLOP Control algorithm (Feedback Local Optimality Principle)

2.1 Introduction

Nowadays technology advances produce mechanical systems with constantly increasing complexity, in order to provide higher performance nonlinear behavior arises and cannot be neglected, moreover electronics devices are no more only accessories in them, but have changed them into Mechatronics systems able to act smarter than in the past times [1-29]. These development leads to all new possibilities that are strictly related to the necessity of automation of these systems, requiring to them the capability of autonomously act in rather complex scenarios, interact with the environment and other agents acting within it. Navigation guidance and control represent the main capability for an autonomous vehicle especially when it has to move properly within other vehicles or cooperate with other agents. Control algorithm become determinant to reach the required standards in terms of safety, task succeeding, reliability, fuel consumption, pollution and fail-safe, especially when human being is involved as in autonomous driving car, autonomous industrial robots and machineries, flying and floating vehicles [30-59]. Optimal based control strategies can consider multiple task and nonlinearities, but a main drawback is present, the Pontryagin optimal control theory, provides feedforward control law [9-16].
The control program form of the solution presents an engineering weakness, that is they use only one single information on the system state: the initial condition. This approach would be natural if the system's model is not affected by any error, the state of the system is perfectly known, and all the environment forces are known in advance. Under these conditions, the system response for any future time depends only on the initial information provided by the initial condition. However, engineering practice and real world meet a different scenario. Models of the controlled process have some degree of approximation, because the real dynamics is only roughly represented by the estimated differential equations, and the environment external disturbance is generally unknown [60-75].
In this context, use of measurements by sensors is of great value and feedback control strategies use the valuable support of measurements. Variation Feedback Control is aimed at using the power of variational functional calculus to state a well posed optimality principle, but using the information coming from sensors, integrating in this way the available information contained into initial conditions, the only one used in the context of control programs, providing a more reliable controlled system [9-16], [60-75].
In this work the FLOP capabilities are shown for two research projects developed by the group of Mechatronic and Vehicle Dynamic Lab of Sapienza, devoted to the realization of two autonomous vehicles that will be discussed in detail within this thesis; the autonomous car, starting from a production series city car and a joint research project, named Secure Platform, devoted to the design an autonomous marine craft vehicle, for rescue purposes.

2.2 Theoretical Foundations, Local Optimality Principle

Optimal control problems, based on variational approach, are constituted by three main elements as stated in 1, the cost function $E\big(x(t), u(t)\big)$, evolution equation $\dot{x} = f\big(x(t), u(t)\big)$, and the optimality principle. The FLOP principle is based on the variational approach and modifies the optimality

principle, by changing it from a global optimality, to a local one, this modification gives the chance to formulate a feedback control law.
Optimal control theory relies on the minimization (or maximization) of a performance index J, subject to the equation of the controlled process $\dot{x} = f(x,u,t)$ with its initial condition $x(0) = x_0$, the evolution equation is introduced by the Lagrangian multiplier $\lambda(t)$ leading to the following:

$$J = \int_0^T E(x,u) + \lambda\big(\dot{x} - f(x,u)\big)\, dt = \int_0^T \mathcal{L}(\dot{x},x,u,\lambda)dt, \tag{8}$$

The solution of the problem is represented by optimal trajectory $x^*(t)$ associated to the optimal control trajectory $u^*(t)$. The Pontryagin's equations can be derived by applying the variational calculus to the (8)

$$\begin{cases} \dfrac{\partial E}{\partial x} - \lambda \dfrac{\partial f}{\partial x} - \dot{\lambda} = 0 \\ \dfrac{\partial E}{\partial u} - \lambda \dfrac{\partial f}{\partial u} = 0 \\ \dot{x} = f(x,u,t) \\ x(0) = x_0 \\ \lambda(T) = 0 \end{cases} \tag{9}$$

The general structure solution is represented by the function $v^* = (x^*, u^*)$ that provides the minimum (maximum) $J^*(x^*, u^*)$, this can be written as:

$$v^* = (x^*, u^*) = V(x_0, T, t) \tag{10}$$

Where the function V represents the general solutions structure, since once E and f are given, the solution depends only by the time horizon T and by the initial condition x_0.
FLOP approach considers a modification of the optimality criterion, passing from the global approach to a local approach, leading to a suboptimal solution $v(x,u)$ that compared to the general solution provided by Pontryagin's theory provides a cost function $J(x,u)$:

$$\forall\, v \neq v^* \ ,\ J(x,u) \geq J(x^*,u^*) \tag{11}$$

this is done considering a time partition of the time interval $[0,T]$ into N-subintervals of the cost function integral:

$$\begin{aligned} J &= \int_0^T \mathcal{L}(\dot{x},x,u,\lambda)dt \\ &= \int_{\tau_0}^{\tau_1} \mathcal{L}(\dot{x},x,u,\lambda)dt + \int_{\tau_1}^{\tau_2} \mathcal{L}(\dot{x},x,u,\lambda)dt + \cdots + \int_{\tau_{N-1}}^{\tau_N} \mathcal{L}(\dot{x},x,u,\lambda)dt \end{aligned} \tag{12}$$

Now in order to obtain a formulation that will be useful for the algorithm developed in following section, it is considered a set of solutions $v_i^* = (x_i^*, u_i^*)$ which, for each subinterval $[\tau_{i-1}, \tau_i]$, minimizes only the related integral, in the place of the optimal solution v^* that solve the problem (9) for the entire time interval $[0, \mathrm{T}]$

$$min\, J_i = \int_{\tau_{i-1}}^{\tau_i} \mathcal{L}(\dot{x}, x, u, \lambda) dt \tag{13}$$

For each integral is required to satisfy the boundary conditions for the related Pontryagin's equations so that:

$$\begin{gathered} x_{i-1}(\tau_{i-1}) = x_i(\tau_{i-1}) \\ \lambda_i(\tau_i) = 0 \end{gathered} \tag{14}$$

Because of the first condition, a piecewise function of class C^0 is generated along the entire interval $[0, T]$.
Now it is possible to express every solution for each interval through the function V defined above, written for the specific integral i, hence with its own initial condition for the state $x_i^*(\tau_{i-1})$ and its time horizon τ_i:

$$v_i^* = V(x_{i-1}^*(\tau_{i-1}), \tau_i, t) \tag{15}$$

The remarkable element of the suggested strategy is that the structure of each of the v_i^* solution is the same for all integrals, except for the parameters $x_{i-1}^*(\tau_{i-1}), \tau_i$, since E and f are the same for each interval and equal to the one assigned for the problem (9).
The new criterion of optimality expressed by (13) leads to:

$$J'^* = \sum_{i=1}^{N} \int_{\tau_{i-1}}^{\tau_{i-1}+\Delta\tau_i} \mathcal{L}(v_i^*) dt \tag{16}$$

In general, cost functions J^* and J'^* differs, and given the modification of the optimality criterion

$$J^* \leq J'^* \tag{17}$$

Nevertheless, problem (9) provides the chance, under some conditions, to formulate a feedback control law, that cannot be provided by solving directly the equations. Hence Local optimality principle offers important advantages respect to the original problem (1).

2.3 FLOP Principle formulation

In the following analysis a constant timestep $\Delta\tau$ is considered, hence the $i-th$ timestep $\Delta\tau_i$ is expressed as function of the overall time horizon T and the number of steps N, hence $\Delta\tau_i = \Delta\tau = T/N$. J'^* is can be re-written as:

$$J'^* = \int_{LB_1}^{UB_1} \mathcal{L}(v_1^*)dt \; + \cdots + \int_{LB_i}^{UB_i} \mathcal{L}(v_i^*)dt \; + \cdots + \int_{LB_N}^{UB_N} \mathcal{L}(v_N^*)dt \,. \tag{18}$$

where $LB_i = (i-1)\Delta\tau$ and $UB_i = i\Delta\tau$.
The solution to the problem can be evaluated by applying the transversality condition $\lambda_i = \lambda|_{UB_i} = 0$ and the continuity condition $x_{LB_i} = x_{UB_{i-1}}$ for each integral, given the initial condition $x_{LB_1} = x_0$, as expressed in (14).
For each integral the following set of equation can be written, these will provide the solution for the $i-th$ timestep:

$$\begin{cases} \dfrac{\partial E}{\partial x_i} - \lambda_i \dfrac{\partial f}{\partial x_i} - \dot{\lambda}_i = 0 \\ \dfrac{\partial E}{\partial u_i} - \lambda_i \dfrac{\partial f}{\partial u_i} = 0 \qquad \forall \; t \in [LB_i, UB_i] \\ \dot{x}_i = f(x_i, u_i, t) \end{cases} \tag{19}$$

This set of equation provides the functions $x_i^*, \lambda_i^*, u^*{}_i, \; i = 1, \dots, N$. The FLOP approaches the method of solution using a discretized version of equations (19). Namely, the time-step discretization is purposely chosen as $\Delta\tau$. Now applying the Euler first-order approximation for $\dot{x}_i$ and $\dot{\lambda}_i$, by neglecting second order terms, one has:

$$\begin{cases} \left.\dfrac{\partial E}{\partial x}\right|_{LB_i} - \left.\left(\lambda \dfrac{\partial f}{\partial x}\right)\right|_{LB_i} - \dfrac{\lambda_{UB_i} - \lambda_{LB_i}}{\Delta\tau} = 0 \\ \left.\dfrac{\partial E}{\partial u}\right|_{LB_i} - \left.\left(\lambda \dfrac{\partial f}{\partial u}\right)\right|_{LB_i} = 0 \qquad \forall \; i \in [1, N] \\ \dfrac{x_{UB_i} - x_{LB_i}}{\Delta\tau} = f\left(x_{LB_i}, u_{LB_i}\right) \end{cases} \tag{20}$$

The solution technique of these equations goes through the following steps:

- from the first interval, $i = 1$, one sets $x_{LB_i} = x_0$ and $\lambda_{UB_i} = 0$. The equations (20) become a system of three equations in three unknowns, $x_{UB_1}, \lambda_{LB_1}, u_{LB_1}$.
- Once (20) is solved, x_{UB_1} is used as initial condition for the interval $i = 2$ which, together with $\lambda_{UB_2} = 0$, produces again a system of three equations in the three unknowns $x_{UB_2}, \lambda_{LB_2}, u_{LB_2}$.
- The process is iterated for all the following intervals up to $i = N$, and it produces the set of desired solutions $x_i^*, \lambda_i^*, u_i^*$, over the whole-time interval $[0, N\Delta\tau]$.

The following figure illustrates the process steps:

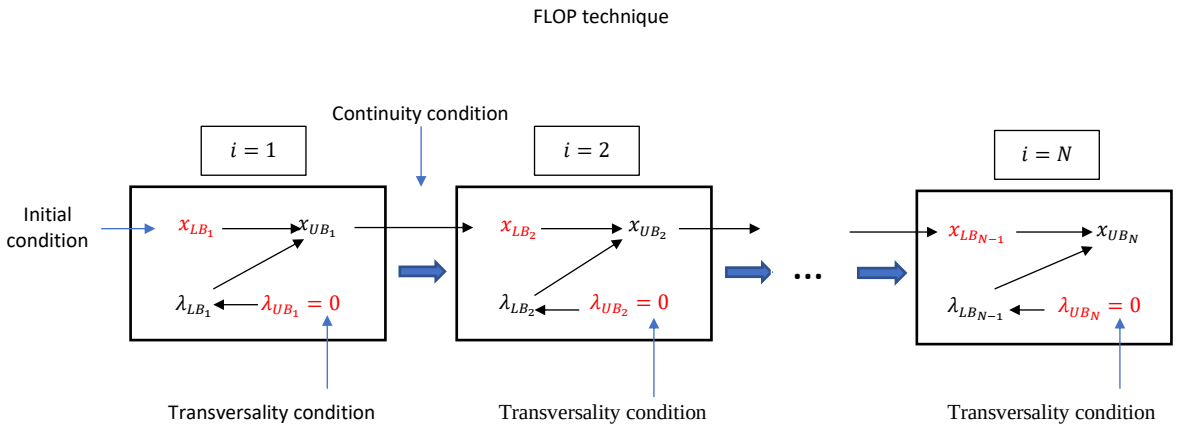

Figure 4: FLOP first two iterations workflow, red quantities are known at each step.

It is important to notice that $\Delta\tau$ plays a special role in the FLOP technique since, it changes the degree of accuracy of the solution. Since it acts as free parameter to be tuned, it is expected that the choice of its value can be suitably selected to obtain the best performance of the present method, as will be shown in the next section, some remarkable considerations can be done to set boundaries value for this parameter.

2.4 FLOP feedback solution technique 1 DOF systems

The local formulation of the optimality as stated by the equation (16), should provide, in general, a solution that performs worse than the solution of the Pontryagin's method. It will be shown that for a problem described by a linear evolution equation $f(x,u)$ and a quadratic cost function $E(x,u)$, the FLOP method described in section 2.3, that relies on the local optimality principle described in section 2.2, will provide the same solution of the Pontryagin's method, given a suitable choice for the length of the time interval $\Delta\tau$.

From equation (20) $\dot{\lambda}_i \cong \frac{\lambda_{UB_i} - \lambda_{LB_i}}{\Delta\tau}$, and the local transversality condition, $\lambda_{UB_i} = 0$, is used. This implies $\dot{\lambda}_i \cong -\frac{\lambda_{LB_i}}{\Delta\tau}$. Looking at the continuous counterpart of this equation, it seems natural to assume $\dot{\lambda} = -\frac{\lambda}{\Delta\tau} = G\lambda$.

This leads to a reformulation of the Pontryagin's problem in the following augmented form:

$$\begin{cases} \dfrac{\partial E}{\partial x} - \lambda\dfrac{\partial f}{\partial x} - \dot{\lambda} = 0 \\ \dfrac{\partial E}{\partial u} - \lambda\dfrac{\partial f}{\partial u} = 0 \\ \dot{x} = f(x,u,t) \\ \dot{\lambda} = G\lambda \end{cases} \quad \forall\ t \in [0,T] \tag{21}$$

This formulation is characterized by the presence of an augmented set of variables, that includes, besides x, u, λ the new variable G. This equation form reveals some important advantages with respect to the classical form (5).
Let solve first the augmented equation (21) under the hypothesis of linearity:

$$\begin{cases} qx - \dot{\lambda} - a\lambda = 0 \\ ru - \lambda b = 0 \\ \dot{x} = ax + bu \\ \dot{\lambda} = G\lambda \end{cases} \tag{22}$$

The set of equation (22) might provide the chance to determine a feedback solution for the control u, at the cost of introducing a new equation for the costate λ that is not directly provided by the variational calculus applied to the integral that defines J. This can be obtained considering a different approach that provides a similar set of equations, but considers a different formulation for the performance index integral, this has been modified as follows:

$$J = \int_0^T \left[\frac{1}{2}q(x - X)^2 + \frac{1}{2}r(u - U)^2 + \lambda(\dot{x} - \phi - bu) + \lambda\dot{g} + \frac{1}{2}\lambda g^2\right] dt \tag{23}$$

The new performance index J now depends on four variables x, u, λ, g, these must be differentiated to minimize the integral J. The functions X, U are time dependent and can be determined, as will be discussed further in this section. Now the (22) representing the Euler-Langrange set of equations can be written as:

$$\begin{cases} q(x - X) - \dot{\lambda} - \lambda\phi_x = 0 \\ r(u - U) - \lambda b = 0 \\ \dot{x} - \phi - bu + \dot{g} + \frac{1}{2}g^2 = 0 \\ \dot{\lambda} - g\lambda = 0 \end{cases}$$

with:

$$\begin{matrix} x(0) = x_0 \\ \lambda(T) = 0 \\ g(0) = g_0 \end{matrix} \tag{24}$$

From the second of the (24) it's possible to express the control u as a function the costate λ:

$$u = \frac{b}{r}\lambda + U$$

Now plugging this back into the Hamilton-Jacobi-Bellman set of equation one obtains

$$\begin{cases} \dot{\lambda} = q(x - X) - \lambda\phi_x \\ \dot{x} + \dot{g} = \phi + \frac{b^2}{r}\lambda + bU - \frac{1}{2}g^2 \\ \dot{\lambda} = g\lambda \end{cases} \tag{25}$$

That is a set of differential equation in the variables x, g, λ. The resulting is system is bad conditioned, because it doesn't respect the Cauchy Theorem, this can be easily proved wrtiting it in it's matricial form by calling $\psi = [\dot{x}, \dot{g}, \dot{\lambda}]^T$:

$$\begin{bmatrix} 0 & 0 & 1 \\ 1 & 1 & 0 \\ 0 & 0 & 1 \end{bmatrix} \psi = \rho(x, g, \lambda) \tag{26}$$
$$A\psi = \rho(x, g, \lambda)$$

The coefficients matrix A has two repeated rows and hence it is not invertible, this means that there is no solution for the system. Beside this, it is possible to eliminate the variable λ, this produces a system of differential equation in the variables x, g. The new system instead does satisfy the Cauchy Theorem and hence a solution for the control is supported. Substituting the third into the first of the (26) one obtains:

$$g\lambda + \lambda\phi_x = q(x - X) \tag{27}$$

Solving for λ:

$$\lambda = \frac{q(x - X)}{g + \phi_x} \tag{28}$$

This permits to express the control u in function of the two variables x e g, this means that the control law is still non feedback, since other dependeces are present.

$$u = \frac{qb}{r}\frac{x - X}{g + \phi_x} + U \tag{29}$$

the (28) can also be used to evaluate $\dot{\lambda}$, that can be substituted into the third of the (26)

$$\dot{\lambda} = q\frac{\dot{x}}{g + \phi_x} - q\frac{x - X}{(g + \phi_x)^2}(\dot{g} + \phi_{xx}\dot{x}) = gq\frac{x - X}{g + \phi_x} \tag{30}$$

Now plugging this last and introducing the (28) into the second and the third equations of the (26), produce the following set of differential equations:

$$\begin{cases} \dot{x} + \dot{g} = \phi + \dfrac{b^2}{r}\dfrac{q(x - X)}{g + \phi_x} + bU - \dfrac{1}{2}g^2 \\ q\dfrac{\dot{x}}{g + \phi_x} - q\dfrac{x - X}{(g + \phi_x)^2}(\dot{g} + \phi_{xx}\dot{x}) = g\dfrac{q(x - X)}{g + \phi_x} \end{cases} \tag{31}$$

After some manipulations and considering the cases in which $g \neq \phi_x$ the resulting set of equations is:

$$\begin{cases} \dot{x} + \dot{g} = \phi + \dfrac{b^2}{r}\left(q\dfrac{x - X}{g + \phi_x}\right) + bU - \dfrac{1}{2}g^2 \\ \dfrac{1}{g + \phi_x}\left[\dot{x} - \dfrac{(x - X)(\dot{g} + \phi_{xx}\dot{x})}{g + \phi_x} - g(x - X)\right] = 0 \end{cases} \tag{32}$$

This can also be written as

$$\begin{cases} \dot{x} + \dot{g} = \phi + \frac{b^2}{r}\left(q\frac{x-X}{g+\phi_x}\right) + bU - \frac{1}{2}g^2 \\ \dot{x}[g + \phi_x - \phi_{xx}(x-X)] - \dot{g}(x-X) = g(x-X)(g+\phi_x) \end{cases} \tag{33}$$

The system of differential equation (33) has two equations in the two unknowns x, g, and hence the chance to find a solution is supported. It is important to enlight one theoretical observation for the costate λ, in fact even though the formulation $\dot{\lambda} = g\lambda$ suggests an exponential behaviour for this variable, its evolution depends on the system state x, therefore the system evolution has to be described in the two variables x, g. The two euqations of the (39) can now be written in matricial form calling $\dot{\tilde{x}} = [\dot{x}, \dot{g}]^T$ as follows:

$$\begin{bmatrix} 1 & 1 \\ [g + \phi_x - \phi_{xx}(x-X)] & -(x-X) \end{bmatrix}\begin{bmatrix} \dot{x} \\ \dot{g} \end{bmatrix} = \begin{bmatrix} \phi + \frac{b^2}{r}\left(q\frac{x-X}{g+\phi_x}\right) + bU - \frac{1}{2}g^2 \\ g(x-X)(g+\phi_x) \end{bmatrix} \tag{34}$$

$$A\dot{\tilde{x}} = \rho(\tilde{x})$$

To satisfy the conditions of the Cauchy Theorem, the matrix A has to be non-singular and hence its determinant has to be non-zero, i.e. invertible. This holds when the following condition is satisfied:

$$[\phi_{xx}] \neq \frac{(x-X)}{(x-X)} + \frac{(g+\phi_x)}{(x-X)} \quad \rightarrow \quad \phi_{xx} \neq 1 + \frac{(g+\phi_x)}{(x-X)} \tag{35}$$

The system (40) when the condition (41) holds provide the chance to find solution. This solution has one limit, in fact it depends on the variable g that depends on time t, this generate a solution for the costate λ that depends on the system's state x but also by the time t through the variable g. This solution might be interesting, but for the robustness of the controlled system, it is preferrable to find an approximated feedback form of the control $u = \frac{b}{r}\lambda(x, g_0)$, where the the variable g is considered to be constant and hence $g(t) = g_0 = cost$, now using this solution for the system (36) one obtains:

$$\begin{cases} \dot{x} = \phi + \frac{b^2}{r}\left(q\frac{x-X}{g_0+\phi_x}\right) + bU - \frac{1}{2}g_0^2 \\ \dot{x}[g_0 + \phi_x - \phi_{xx}(x-X)] = g_0(x-X)(g_0+\phi_x) \end{cases} \tag{36}$$

This formulation introduces an error, in fact the system's state x is required to satisfy two different differential equations. This error appears evident by substituing the first of the (36) into the second:

$$[g_0 + \phi_x - \phi_{xx}(x-X)]\left[\phi + \frac{b^2}{r}\left(q\frac{x-X}{g_0+\phi_x}\right) + bU - \frac{1}{2}g_0^2\right] = g_0(x-X)(g_0+\phi_x) \tag{37}$$

This formulation can be discussed introducing under the hipothesis:

$$\left|\frac{(g_0+\phi_x)}{(x-X)}\right| \gg |\phi_{xx}| \tag{38}$$

That coupled with the (34) defines the renge of apllicability of the FLOP technique. With the (38) the (37) can be simplified as:

$$(g_0 + \phi_x)\left[\phi + \frac{b^2}{r}\left(q\frac{x-X}{g_0+\phi_x}\right) + bU - \frac{1}{2}g_0^2\right] = g_0(x-X)(g_0+\phi_x) \tag{39}$$

And considering the condition $g \neq \phi_x$ applied in the (39):

$$\phi + \frac{b^2}{r}\left(q\frac{x-X}{g_0+\phi_x}\right) + bU - \frac{1}{2}g_0^2 = g_0(x-X) \tag{40}$$

This last equation, supports the choice for the variable $g(t) = g_0$ to be constant, in fact this approximation holds as long as is possible to admit that the first and the second members of the (40) are equal. In fact the (40) states that the first member, that depends on the state x nonlinearly, can be approximated as a linear function of x, this hypothesis is supported for specific cases and for specific values of g_0.

This can also be shown performing a first order Taylor series of the first member of the (40):

$$\begin{aligned} &\phi + \frac{b^2}{r}\left(q\frac{x-X}{g_0+\phi_x}\right) + bU - \frac{1}{2}g_0^2 \;\cong \\ &\cong \phi(X) - \frac{1}{2}g_0^2 + bU + \left(\phi_x(X) + \frac{b^2}{r}\left(q\frac{1}{g_0+\phi_x(X)}\right)\right)(x-X) \end{aligned} \tag{41}$$

Now since the equality of this expression and of the second member of the (40) has to hold, g_0 and the function $U = U_0$ that is also assumed to be constant, have to satisfy the following conditions:

$$\begin{cases} \phi(X) - \frac{1}{2}g_0^2 + bU_0 = 0 \\ g_0 = \phi_x(X) + \frac{b^2}{r}\left(q\frac{1}{g_0+\phi_x(X)}\right) \end{cases} \tag{42}$$

This produce for U_0:

$$U_0 = -\frac{\phi(X)}{b} + \frac{g_0^2}{2b} \tag{43}$$

While the second of the system (42) produces:

$$\begin{aligned} &g_0\big(g_0 + \phi_x(X)\big) = \phi_x(X)\big(g_0 + \phi_x(X)\big) + \frac{b^2}{r}q \\ &g_0^2 = \phi_x^2(X) + \frac{b^2}{r}q \\ &g_0 = \pm\sqrt{\phi_x^2(X) + \frac{b^2}{r}q} \end{aligned} \tag{44}$$

This provides two solutions, but only one of the is correct, the negative one. In fact considering the differential equation $\dot{\lambda} = g\lambda$ and the required final condition for the costate $\lambda(T) = 0$, defined in the

Optimal Control Theory, λ will be zero for T sufficiently high, if and only if $g = g_0 = const$ is negative.

$$g_0 = -\sqrt{\phi_x^2(X) + \frac{b^2}{r}q} \tag{45}$$

It has to be noted that the validity of the (43) is supported only in those cases where the state x and the reference for the state X, are sufficiently close, otherwise the linearization process described so far, wouldn't hold anymore due to errors $o(x - X)^2$ and higher orders.

This means that the minimization of the performance index J defined in (23) can be performed effectively, when the function $g = g_0$ is assumed to be constant, only for reduced intervals, i.e. locally.

This shows that the technique guarantees the minimization of each sub-interval, where g_0 is choosen, but this does not guarantee the global minimization, i.e. for the whole interval $[0, T]$.

This explains the local minima provided by the feedback control technique proposed, that provides the following control law, when g is set to be constant:

$$u(x) = \frac{b}{r}q\frac{x - X}{g_0 + \phi_x} + U_0 \tag{46}$$

Moreover the (44) suggests updating periodically the value for g_0, if this update is not performed the error increases but the procedure validity is still supported.

The method described so far can be synthetically summarized and written in more general form, introducing the general cost function $q(x)$ for the state, as follows: minimization of the integral that provides the performance index J

$$J = \int_0^T \left[q(x) + \frac{1}{2}r(u - U_0)^2 + \lambda\left(\dot{x} - \phi - bu - \frac{1}{2}g_0^2\right)\right]dt \tag{47}$$

Means that is possible to use the following form of the control law:

$$u = \frac{b}{r}\frac{q_x}{g_0 + \phi_x} + U_0 \tag{48}$$

For the dynamic system $\dot{x} = \phi(x) + bu - \frac{1}{2}g_0^2$, this holds only under the conditions:

$$\phi_{xx} \neq \frac{q_{xx}}{q_x}(g + \phi_x) + 1 \;\; ; \;\; \left|\frac{(g_0 + \phi_x)}{(x - X)}\right| \gg |\phi_{xx}| \tag{49}$$

Moreover, the considered time interval $[0, \mathrm{T}]$ must be sufficiently small, such that the linearization (40) holds.

Now if the considered dynamic equation is of the form $\dot{x} = \phi(x) + bu - \frac{1}{2}g_0^2$, i.e. the term $-\frac{1}{2}g_0^2$ is taken into the account, the minimized integral will be:

$$J_0 = \int_0^T \left[q(x) + \frac{1}{2}r(u - U_0)^2\right]dt \tag{50}$$

Instead if the considered dynamic is $\dot{x} = \phi(x) + bu$ the locally minimized integral will then be:

$$J_1 \cong J_0 + \int_0^T \frac{1}{2} g_0^2 dt \tag{51}$$

Here the approximation is related to the fact that since a different dynamic is used, the first term of J_1 will be exactly J_0 plus an added term due to the choice of the dynamic expression. The error $e_{relative}$ introduced by this assumption can be measured a posteriori through the following ratio:

$$e_{relative} = \frac{\frac{1}{2}\int_0^T g_0^2 dt}{J_0} \tag{52}$$

The locally nature of the FLOP technique is stated by the equation (40), this demonstrates that the effectiveness of the FLOP approach is enhanced whenever the whole-time interval $[0, T]$ is divided into sufficiently small sub intervals $[0, \Delta\tau]$, in fact for each of them $|x - X|$ is small and the assumption $g(t) = g_0$ holds. This means that the overall minimization of J is here obtained through the minimization of the small sub-intervals, where $|x - X|$ is small, and g_0 can be properly choosen for each of them. The solutions obtained will also minimize J. Therefore, the equation (40) supports the initial hypothesis in the FLOP technique, related to the local optimality, in the place of the global criteria that belongs to the Optimal Control Theory.

2.5 A simple 1 DOF case

In order to show FLOP method capabilities, a simple 1 DOF test case will be discussed, the system is highly nonlinear as shown by its dynamic equation $f(x, u) = \dot{x} = x \tanh x + u$. The performance provided by the FLOP will be compared to that provided by the LQR, this is an interesting comparison, since LQR controller class provides, under suitable assumptions, the feedback solution to the Optimal control problems, these assumptions constraint the dynamic equation $f(x, u)$ to be linear and a quadratic cost function $E(x, u)$. Given the highly nonlinearity of the system the LQR needs the linearization of the system about x_T, u_T, in order to be applied:

$$\left.\frac{df(x,u)}{dx}\right|_{x_T,u_T} = tanh\, x_T - x_T(tanh^2\, x_T - 1) = a \tag{53}$$

such that the linear dynamics is:

$$\dot{x} = a(x - x_T) + u_{LQR} - u_T \tag{54}$$

The variable u_T can be determined through the dynamic equation, as follows:

$$\dot{x_T} = 0 = \phi(x_T) + u_T \implies u_T = -\phi(x_T) \tag{55}$$

A quadratic cost function is defined as:

$$E(x, u) = qx^2 + ru^2 \tag{56}$$

The stability of the linearized system depends on the sign of x_T. For $x_T < 0$ the real part of system's eigenvalue is negative providing a stable system, while a positive real part of the eigenvalue is given when $x_T > 0$, leading to an unstable system. The control law provided by the LQR is:

$$u_{LQR} = K(x - x_T) - \phi(x_T) \tag{57}$$

where K is the solution of the steady Riccati's equation. The application of the FLOP technique described in the previous section through equations (84), with $S = 0, g(x) = 0, B = 1$, produces:

$$u_{FLOP} = r(\Phi(x) + G)^{-1} q(x - x_T) - \phi(x_T) \tag{58}$$

where $G = -\frac{1}{\Delta\tau}$.

The values for q and r are identical for both the methods, FLOP and LQR, and the comparison is performed for the values reported in table 1.

Symbol	Value
x_0 :	-1
x_t :	1
q :	1
r :	0.1

Tab 1: Set of values

The conditions for x_0 and x_T are chosen such that the system has to go through the origin, passing from the stable region $(x < 0)$ to the unstable region $(x > 0)$. In Figure , the values of the functional J, the state variable, and the control variable both for the LQR and the FLOP cases are compared.

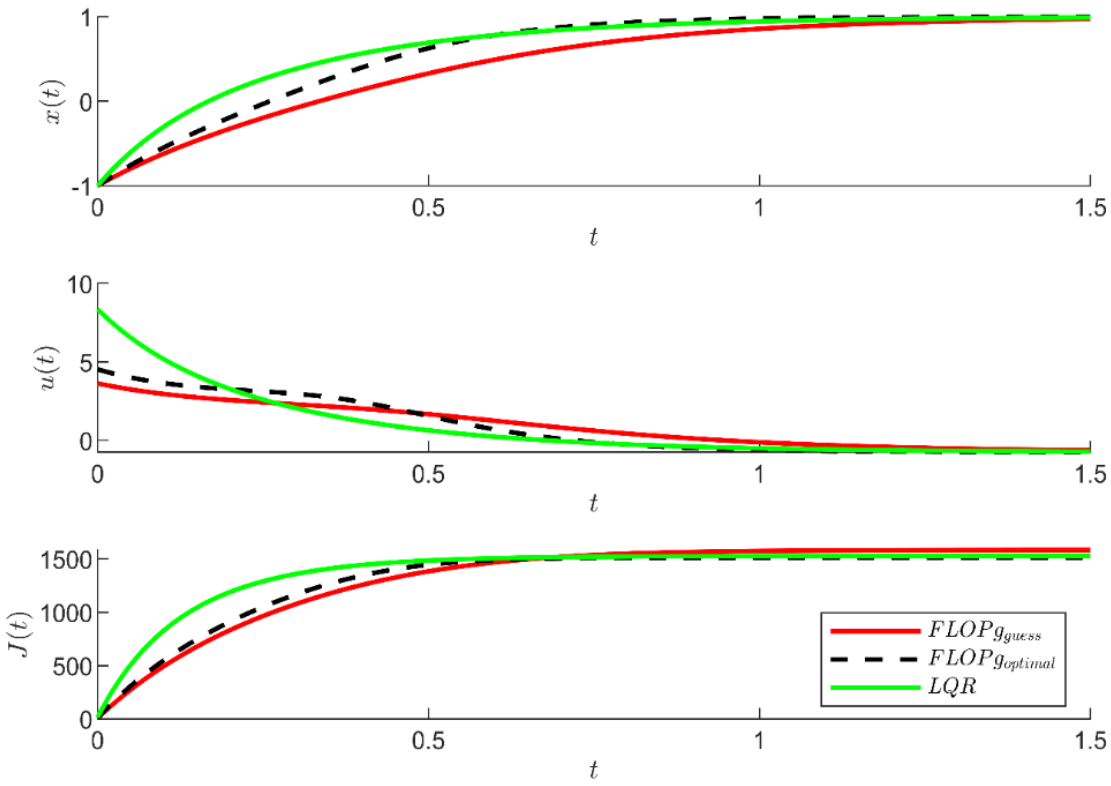

Figure 5: Evolution of the system's state x, of the control u and of cost function, for the LQR controller and for two different choice of the tuning parameter g for the FLOP controller, the first value is selected using the function proposed in the previous paragraph, the second is chosen by iterative tests until the best performance is reached.

In Fig. 5 an interesting performance has to be noticed that for the $g_{optimal}$ case $J_{FLOP}(t) < J_{LQR}(t)\ \forall\ t$ a desired result. Moreover, the system controlled using the FLOP approach, reaches the target in advance with respect to the one controlled by the LQR, showing the superiority of the FLOP, when a proper value for g is selected, with respect to the LQR in this nonlinear case. Moreover, the graph related to the control action u shows that the FLOP control is sensitive to the presence of the nonlinearity, exhibiting a slope variation when passing from the stable to the unstable region, while the LQR is insensitive since it is based on a linearized formulation. Even though the performance provided by the case in which the parameter g is selected using the formula (50) are slightly poorer compared to the other two controllers, it's interesting that the performance is comparable, meaning that the guessed value for g represents a good starting point for fine tuning the FLOP control.
This advantage is clearly shown by the Fig. 6, This represent the overall performance index J for different values of the tuning parameter g, showing that the guessed value lays very close to the basin of $g's$ that provide the best performance, and hence it provides an important indication for the controller tuning process, and fasten the whole process.

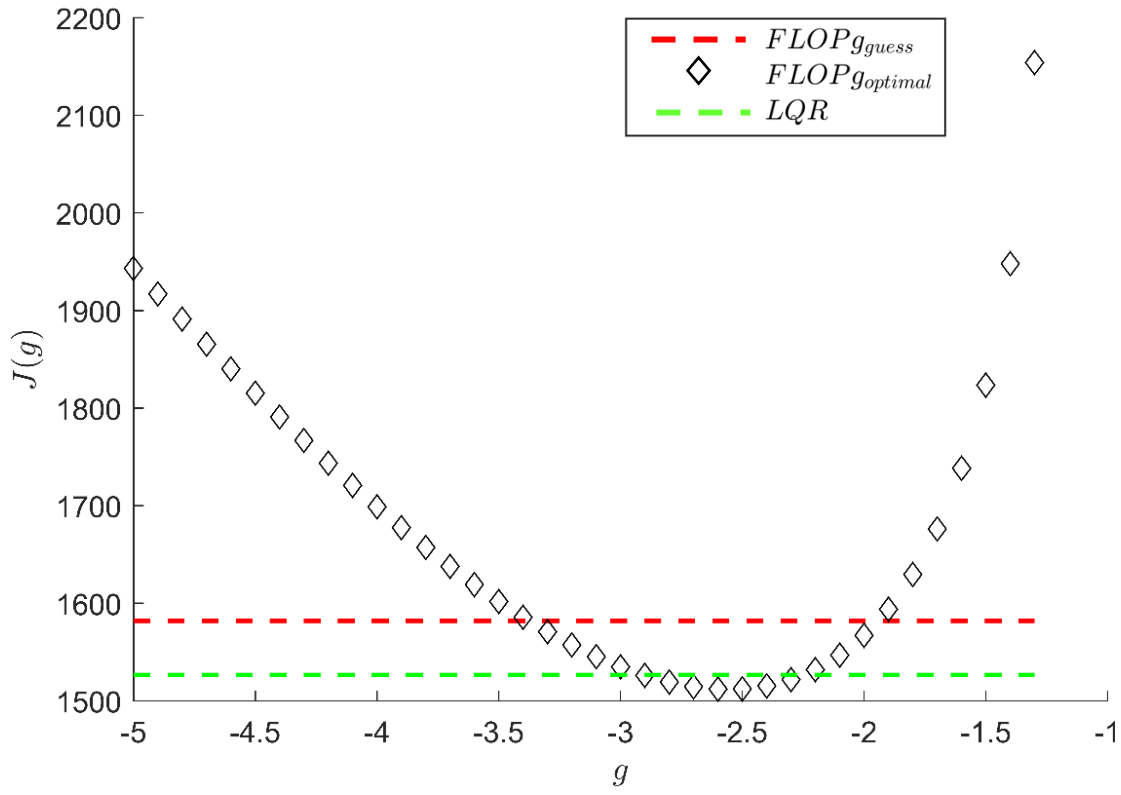

Figure 6: Performance index J provided by different choices of the tuning parameter g, these are compared with the value g_{guess} evaluated by the formula (52) and with the LQR technique.

2.6 FLOP technique formulation for N-DOF systems

Following the same procedure applied in the 1 DOF case, the method can be easily extended to the n-DOF linear case. Starting from the definition (23) of the performance index J, similar calculation of section 3.4 is performed, but this time in n-DOF case:

$$J = \int_0^T \frac{1}{2}(\boldsymbol{x}-\boldsymbol{X})^T\boldsymbol{Q}(\boldsymbol{x}-\boldsymbol{X}) + \frac{1}{2}(\boldsymbol{u}-\boldsymbol{U})^T\boldsymbol{R}(\boldsymbol{u}-\boldsymbol{U}) + \boldsymbol{\lambda}^T(\dot{\boldsymbol{x}}-\boldsymbol{\phi}-\boldsymbol{B}\boldsymbol{u}) + \boldsymbol{\lambda}^T\dot{\boldsymbol{g}} + \frac{1}{2}\boldsymbol{g}^T\boldsymbol{\Lambda}\boldsymbol{g}\,dt \tag{59}$$

Where is a diagonal matrix $\boldsymbol{\Lambda} = diag(\boldsymbol{\lambda})$ generated by the vector $\boldsymbol{\lambda} = [\lambda_1, \dots, \lambda_n]^{\boldsymbol{T}}$ with n dimension of the state of the system $\boldsymbol{x}$.
Analogously, the constant vector $\boldsymbol{g} = [g_1, \dots, g_n]^{\boldsymbol{T}}$ generates a diagonal matrix $\boldsymbol{G}$, that as in the 1 DOF case represents a gains matrix, $\boldsymbol{G} = diag(\boldsymbol{g})$.
Therefore, the added scalar term in the integrand of the (59) can be written as:

$$\boldsymbol{\lambda}^T\dot{\boldsymbol{g}} + \frac{1}{2}\boldsymbol{g}^T\boldsymbol{\Lambda}\boldsymbol{g} = \sum_{\boldsymbol{i}}\lambda_i\dot{g}_i + \sum_{\boldsymbol{i}}\lambda g_i^2 \tag{60}$$

Applying the variational calculus to this term produces the n-dimensional counterpart of the auxiliary equation $\dot{\lambda} = g\lambda$.

$$\int_0^T \frac{\partial}{\partial g_r}\left(\sum_{\boldsymbol{i}}\lambda_i\dot{g}_i + \sum_{\boldsymbol{i}}\lambda g_i^2\right)\delta g_r + \frac{\partial}{\partial \dot{g}_r}\left(\sum_{\boldsymbol{i}}\lambda_i\dot{g}_i + \sum_{\boldsymbol{i}}\lambda g_i^2\right)\delta\dot{g}_r\,dt = \int_0^T (\lambda_r g_r - \dot{\lambda}_r)\delta g_r + [\lambda_r\delta g_r]_0^T \tag{61}$$

Following the same steps performed in the 1 d.o.f. formulation, the third of the set (24) becomes:

$$\dot{\boldsymbol{x}} - \boldsymbol{\phi} - \boldsymbol{B}\boldsymbol{u} + \dot{\boldsymbol{g}} + \frac{1}{2}\boldsymbol{G}\boldsymbol{g} = \boldsymbol{0} \tag{62}$$

Analogously the (40) is modified into:

$$\left[\boldsymbol{\phi} + \boldsymbol{B}\boldsymbol{R}^{-T}\boldsymbol{B}^T[(\boldsymbol{G} + \boldsymbol{\phi}_{\boldsymbol{x}}^T)^{-1}\boldsymbol{Q}^T(\boldsymbol{x}-\boldsymbol{X})] + \boldsymbol{B}\boldsymbol{U} - \frac{1}{2}\boldsymbol{G}\boldsymbol{g}\right] = \boldsymbol{G}(\boldsymbol{x}-\boldsymbol{X}) \tag{63}$$

As in the one-dimensional case optimal values for $\boldsymbol{G} = \boldsymbol{G}_0$ or $\boldsymbol{g}_0$ can be determined using:

$$\boldsymbol{G}_0 - \boldsymbol{\phi}_{\boldsymbol{x}}(\boldsymbol{x}) = \boldsymbol{R}^{-1}\boldsymbol{B}^T\left(\boldsymbol{g}_0 + \boldsymbol{\phi}_{\boldsymbol{x}}^T(\boldsymbol{x})\right)^{-1}\boldsymbol{Q} \tag{64}$$

The (64) represents an implicit matricial equation in $\boldsymbol{G}_0$, the solution can be determined considering $\boldsymbol{G}_0$ to be diagonal, and therefore, in general no exact solution for it can be determined. To simply solve this implicit equation, another assumption can be considered, the structure of the matrix $\boldsymbol{G}_0$ can be assumed more than diagonal, i.e. $\boldsymbol{G}_0 = \boldsymbol{g}_0\boldsymbol{I}_{n\times n} = -\frac{1}{\Delta\tau}\boldsymbol{I}_{n\times n}$ which means that all the terms of the matrix diagonal are assumed to be equal and negative. Under this hypothesis the (64) becomes:

$$-\frac{1}{\Delta\tau}\boldsymbol{I}_{n\times n} - \boldsymbol{\phi}_{\boldsymbol{x}}(\boldsymbol{x}) - \boldsymbol{R}^{-1}\boldsymbol{B}^T\left(-\frac{1}{\Delta\tau} + \boldsymbol{\phi}_{\boldsymbol{x}}^T(\boldsymbol{x})\right)^{-1}\boldsymbol{Q} = \epsilon(\boldsymbol{g}_0) \tag{65}$$

With $\epsilon(\boldsymbol{g}_0)$ an error matix, the error is due to the simplification on the structure of the $\boldsymbol{G}_0$ matrix.

After fixing a structure for $\epsilon(\boldsymbol{g}_0)$ and also a norm for it $||\epsilon(\boldsymbol{g}_0)||$ it is possible to find numerically $\boldsymbol{g}_0$ such that :

$$\boldsymbol{g}_0 : \min\ ||\epsilon(\boldsymbol{g}_0)|| \tag{66}$$

The (66) can now be used as a useful instrument to properly select $\boldsymbol{g}_0$ and hence $\Delta\tau$ to minimize the norm of the error $||\epsilon(\boldsymbol{g}_0)||$ and therefore improve the performance**.** In general better solutions can be otbained from the (64), if some of the assumptions made are removed, for instance, if the elements of the diagonal of $\boldsymbol{G}_0$ are not considered all euqual to $\boldsymbol{g}_0$.
One procedure to identify the best value for $\boldsymbol{G}_0$ taking into the account only the assumptions made on its structure can be the following. The equation (70) can be rewritten as:

$$\boldsymbol{I}\boldsymbol{g}_0 = \boldsymbol{\phi}_{\boldsymbol{x}}(\boldsymbol{x}) + \boldsymbol{R}^{-1}\boldsymbol{B}^T\left(\boldsymbol{g}_0 + \boldsymbol{\phi}_{\boldsymbol{x}}^T(\boldsymbol{x})\right)^{-1}\boldsymbol{Q} \tag{67}$$

Now calling the second member of the () $\boldsymbol{A}(\boldsymbol{g}_0)$:

$$\boldsymbol{I}\boldsymbol{g}_0 = \boldsymbol{A}(\boldsymbol{g}_0) \tag{68}$$

The technique is iterative, in fact since $\boldsymbol{A}(\boldsymbol{g}_0)$ depends on $\boldsymbol{g}_0$ it is possible to choose an initial guess for it $\boldsymbol{g}_0^{(1)}$, for instance a vector with all elements equal to 1. Then the matrix $\boldsymbol{A}$ can be calculated as:

$$\boldsymbol{A}\left(\boldsymbol{g}_0^{(1)}\right) = \boldsymbol{\phi}_{\boldsymbol{x}}(\boldsymbol{x}) + \boldsymbol{R}^{-1}\boldsymbol{B}^T\left(\boldsymbol{g}_0^{(1)} + \boldsymbol{\phi}_{\boldsymbol{x}}^T(\boldsymbol{x})\right)^{-1}\boldsymbol{Q} \tag{69}$$

It is possible to evaluate for $\boldsymbol{A}$ its matrix of the eigenvalues $\boldsymbol{\Lambda}_{\mathbf{A}}$ that is diagonal. Now because of the (68) and because the matrix $\boldsymbol{G}_0 = \boldsymbol{I}\boldsymbol{g}_0$ is assumed diagonal, the second guess for it will be equal to the matrix $\boldsymbol{\Lambda}_{\mathbf{A}}$:

$$\boldsymbol{I}\boldsymbol{g}_0^{(2)} = \boldsymbol{\Lambda}_{\mathbf{A}}\left(\boldsymbol{g}_0^{(1)}\right) \tag{70}$$

The procedure can be performed several times, and can be generalized as follows:

$$\boldsymbol{I}\boldsymbol{g}_0^{(i+1)} = eig\left(\boldsymbol{\phi}_{\boldsymbol{x}}(\boldsymbol{x}) + \boldsymbol{R}^{-1}\boldsymbol{B}^T\left(\boldsymbol{g}_0^{(i)} + \boldsymbol{\phi}_{\boldsymbol{x}}^T(\boldsymbol{x})\right)^{-1}\boldsymbol{Q}\right) \tag{71}$$

This provide a chance to overcome the assumption that all the elements of the diagonal of $\boldsymbol{G}_0$ are equal, even though the convergence of the technique is not guaranteed, in that case the use of the (66) is recommended.
Now the variational calculus provides the following Hamilton-Jacobi-Bellman set of differential equations:

$$\begin{cases} \boldsymbol{Q}_{\boldsymbol{x}} - \boldsymbol{\phi}_{\boldsymbol{x}}^T\boldsymbol{\lambda} = \dot{\boldsymbol{\lambda}} \\ \boldsymbol{R}^T(\boldsymbol{u} - \boldsymbol{U}) - \boldsymbol{B}^T\boldsymbol{\lambda} = \boldsymbol{0} \\ \dot{\boldsymbol{x}} - \boldsymbol{\phi} - \boldsymbol{B}\boldsymbol{u} + \dot{\boldsymbol{g}} + \frac{1}{2}\boldsymbol{G}\boldsymbol{g} = \boldsymbol{0} \\ \dot{\boldsymbol{\lambda}} - \boldsymbol{G}\boldsymbol{\lambda} = \boldsymbol{0} \end{cases}$$

with:

$$\begin{gathered} \boldsymbol{x}(0) = \boldsymbol{x_0} \\ \boldsymbol{\lambda}(T) = \boldsymbol{0} \\ \boldsymbol{G}(0) = \boldsymbol{G_0} \end{gathered} \tag{72}$$

The control u can be expressed as:

$$\boldsymbol{u} = \boldsymbol{R}^{-T}\boldsymbol{B}^T\boldsymbol{\lambda} + \boldsymbol{U}$$

When the control law is plugged inside the system (72), the set of equations becomes:

$$\begin{cases} \boldsymbol{\lambda} = (\boldsymbol{G} + \boldsymbol{\phi}_x^T)^{-1} Q_x \\ \boldsymbol{u} = \boldsymbol{R}^{-T}\boldsymbol{B}^T[(\boldsymbol{G} + \boldsymbol{\phi}_x^T)^{-\mathbf{1}} Q_x] + \boldsymbol{U} \\ \dot{\boldsymbol{x}} - \boldsymbol{\phi} - \boldsymbol{B}\boldsymbol{u} + \dot{\boldsymbol{g}} + \frac{1}{2}\boldsymbol{G}\boldsymbol{g} = \mathbf{0} \\ \dot{\boldsymbol{\lambda}} = \boldsymbol{G}\boldsymbol{\lambda} \end{cases} \tag{73}$$

Performing the variations both with the LQR test function and with the FLOP test function, it follows:

$$\begin{cases} \boldsymbol{Q}^T\boldsymbol{x} - \boldsymbol{A}^T\boldsymbol{\lambda} = \dot{\boldsymbol{\lambda}} \\ \boldsymbol{R}^T\boldsymbol{u} - \boldsymbol{B}^T\boldsymbol{\lambda} = 0 \\ \dot{\boldsymbol{x}} = \boldsymbol{A}\boldsymbol{x} + \boldsymbol{B}\boldsymbol{u} \\ \boldsymbol{\lambda} = \boldsymbol{P}\boldsymbol{x} \end{cases} \tag{74}$$

In the LQR case, and:

$$\begin{cases} \boldsymbol{Q}^T\boldsymbol{x} - \boldsymbol{A}^T\boldsymbol{\lambda} = \dot{\boldsymbol{\lambda}} \\ \boldsymbol{R}^T\boldsymbol{u} - \boldsymbol{B}^T\boldsymbol{\lambda} = 0 \\ \dot{\boldsymbol{x}} = \boldsymbol{A}\boldsymbol{x} + \boldsymbol{B}\boldsymbol{u} \\ \dot{\boldsymbol{\lambda}} = \boldsymbol{G}\boldsymbol{\lambda} \end{cases} \tag{75}$$

in the FLOP case. As in the 1 DOF case is interesting to compare the LQR's gain with the FLOP's one. In order to do that, from set of equations (74) and (75) input vectors, respectively $\boldsymbol{u_{LQR}}$ and $\boldsymbol{u_{FLOP}}$ are evaluated, so that:

$$\boldsymbol{u_{LQR}} = \boldsymbol{K_{LQR}}\boldsymbol{x} = -\boldsymbol{R}^{-T}\boldsymbol{B}^T\boldsymbol{P}\boldsymbol{x} \tag{76}$$

and

$$\boldsymbol{u_{FLOP}} = \boldsymbol{K_{FLOP}}\boldsymbol{x} = \boldsymbol{R}^{-T}\boldsymbol{B}^T(\boldsymbol{A}^T + \boldsymbol{G})^{-1}\boldsymbol{Q}^T\boldsymbol{x} \tag{77}$$

By equalizing two gains it follows:

$$\boldsymbol{G} = (\boldsymbol{Q}^T\boldsymbol{P}^{-1} + \boldsymbol{A}^T) \tag{78}$$

From set of equations (75) it is possible to obtain

$$\boldsymbol{A}^T\boldsymbol{G} + \boldsymbol{G}\boldsymbol{G} = \boldsymbol{Q}^T\boldsymbol{A}\boldsymbol{Q}^{-T}\boldsymbol{A}^T + \boldsymbol{Q}^T\boldsymbol{A}\boldsymbol{Q}^{-T}\boldsymbol{G} + \boldsymbol{Q}^T\boldsymbol{B}\boldsymbol{R}^{-T}\boldsymbol{B}^T \tag{79}$$

By plugging in (79) the (78) and by doing some evaluation, it results:

$$\boldsymbol{P}\boldsymbol{A} - \boldsymbol{P}\boldsymbol{B}\boldsymbol{R}^{-\boldsymbol{T}}\boldsymbol{B}^{\boldsymbol{T}}\boldsymbol{P} + \boldsymbol{Q}^{\boldsymbol{T}} + \boldsymbol{A}^{\boldsymbol{T}}\boldsymbol{P} = \mathbf{0} \tag{80}$$

which is exactly the Riccati's equation.
Now as already shown, the augmented formulation can be used by introducing:

$$\dot{\boldsymbol{\lambda}}(t) = \boldsymbol{G}\boldsymbol{\lambda}(t) \tag{81}$$

The solution for the optimal FLOP control and independently of the structure of G, is provided by:

$$\dot{\boldsymbol{x}} = \boldsymbol{A}\boldsymbol{x} + \boldsymbol{B}\boldsymbol{u}$$
$$\boldsymbol{u}_{\boldsymbol{FLOP}} = \boldsymbol{K}_{\boldsymbol{FLOP}}\boldsymbol{x} = \boldsymbol{R}^{-T}\boldsymbol{B}^{T}(\boldsymbol{A}^{T} + \boldsymbol{G})^{-1}\boldsymbol{Q}^{T}\boldsymbol{x} \tag{82}$$

Following the same finding of the 1DOF system, i.e. $\dot{\lambda} = -\frac{\lambda}{\Delta\tau} = G\lambda$, the form of G can be adopted $\boldsymbol{G} = -\frac{\boldsymbol{I}}{\Delta\tau}$, where the value for $\Delta\tau$ is not provided at this stage of the method, and part of a tuning process described later.

2.7 Affine systems class, dealing with nonlinearities

A straight generalization to nonlinear multiple DOF systems is possible, the solution provided by the FLOP approach seen so far is limited to the class of control-affine systems $\dot{\boldsymbol{x}} = \boldsymbol{\phi}(\boldsymbol{x}) + \boldsymbol{B}\boldsymbol{u} + \boldsymbol{C}$ with $\boldsymbol{\phi}(\boldsymbol{x})$ general differentiable nonlinear function, this formulation implies that, in general, nonlinearities that involve the control vector $\boldsymbol{u}$ has to be linearized, further in this section a technique to deal with these kind of nonlinearities is proposed. The cost functional is:

$$J = \int_{0}^{T} \frac{1}{2}\boldsymbol{x}^{T}\boldsymbol{Q}\boldsymbol{x} + \frac{1}{2}\boldsymbol{u}^{T}\boldsymbol{R}\boldsymbol{u} + g(\boldsymbol{x}) + \boldsymbol{\lambda}^{T}\left(\dot{\boldsymbol{x}} - (\boldsymbol{\phi}(\boldsymbol{x}) + \boldsymbol{B}\boldsymbol{u})\right) dt \tag{83}$$

where the cost function $E(\boldsymbol{x},\boldsymbol{u}) = \frac{1}{2}\boldsymbol{x}^{T}\boldsymbol{Q}\boldsymbol{x} + \frac{1}{2}\boldsymbol{u}^{T}\boldsymbol{R}\boldsymbol{u} + g(\boldsymbol{x})$ includes the very general nonlinear differentiable term $g(\boldsymbol{x})$, besides the standard quadratic forms. While nonlinear functions of the control variables $g(\boldsymbol{u})$, provide a set of equation that in general, don't provide an explicit expression for $\boldsymbol{u}$.
Applying the FLOP method to equation (83), one obtains

$$\dot{\boldsymbol{x}} = \boldsymbol{\phi}(\boldsymbol{x}) + \boldsymbol{B}\boldsymbol{u}$$
$$\boldsymbol{u} = (\boldsymbol{R}^{T})^{-1}\boldsymbol{B}^{T}[\boldsymbol{\Phi}(\boldsymbol{x})^{T} + \boldsymbol{G}]^{-1}[\boldsymbol{Q}^{T}\boldsymbol{x} + \boldsymbol{\gamma}^{T}(\boldsymbol{x})] \tag{84}$$

where:

- $\boldsymbol{G} = -\frac{1}{\Delta\tau}\boldsymbol{I}$
- $\boldsymbol{\Phi}(\boldsymbol{x}) = \boldsymbol{\nabla}_{\boldsymbol{x}}\boldsymbol{\phi}(\boldsymbol{x})$
- $\boldsymbol{\gamma}(\boldsymbol{x}) = \boldsymbol{\nabla}_{\mathbf{x}} g(\boldsymbol{x})$

In equation (83), the introduction of $\boldsymbol{g}(\boldsymbol{x})$ provides the chance of introducing sharp local variations of the cost function, these are suitable to constraint the system's state into specific and generally unstable, regions of the reachable dynamics, moreover they can be used for obstacle avoidance purposes as well as for target reaching.
A more general class of controlled system is represented by $\dot{\boldsymbol{x}} = \boldsymbol{f}(\boldsymbol{x},\boldsymbol{u}) = \boldsymbol{\phi}(\boldsymbol{x}) + \boldsymbol{\psi}(\boldsymbol{u}) + \boldsymbol{C}$, where the function $\boldsymbol{\psi}(\boldsymbol{u})$ is nonlinear in one or more control variables represented by the vector $\boldsymbol{u}$, in order to apply the FLOP approach, a linearization of $\boldsymbol{\psi}(\boldsymbol{u})$ is required, in order to obtain a dynamic equation that belongs to the class of control-affine systems $\dot{\boldsymbol{x}} = \boldsymbol{\phi}(\boldsymbol{x}) + \boldsymbol{B}\boldsymbol{u} + \boldsymbol{C}$. A chance to consider this class of dynamic systems without introducing linearization of the control dependent function is obtained by adding to the system, a number p of first order linear differential equation, with $p = m - l$ number of degrees of control that affect the system response through a nonlinear function, given m number of control variables i.e. length of the vector $\boldsymbol{u}$ and l number of control variable from which the system linearly depends. This set of differential equation can be designed to mimic the actuators dynamic response, or in a more general case to approximate it. The set of the p control variables can

be grouped in the vector $\boldsymbol{q}$, while the l variable can be grouped in the vector $\boldsymbol{t}$, hence the $\boldsymbol{\psi}(\boldsymbol{u})$ can be written as:

$$\boldsymbol{\psi}(\boldsymbol{u}) = \boldsymbol{B}_{\boldsymbol{\psi}}\boldsymbol{t} + \boldsymbol{\chi}(\boldsymbol{q}) \tag{85}$$

As stated above the system will result into its augmented form $\boldsymbol{x}_a^T = [\boldsymbol{x}; \boldsymbol{q}]^T$ this causes the function $\boldsymbol{\chi}(\boldsymbol{q})$ that is the nonlinear control part of the $\boldsymbol{\psi}(\boldsymbol{u})$ can be summed to the $\boldsymbol{\phi}(\boldsymbol{x})$ since now $\boldsymbol{q}$ is part of the augmented state $\boldsymbol{x}_a$, leading to a new $\boldsymbol{\phi}'(\boldsymbol{x}, \boldsymbol{q})$:

$$\boldsymbol{\phi}'(\boldsymbol{x}, \boldsymbol{q}) = \boldsymbol{\phi}(\boldsymbol{x}) + \boldsymbol{\chi}(\boldsymbol{q}) \tag{86}$$

The set of first order linear differential equation are written in terms of the control variables $\boldsymbol{q}$ in terms of the new control variables $\boldsymbol{v}$ as follows:

$$\dot{\boldsymbol{q}} = -\boldsymbol{K}(\boldsymbol{q} - \boldsymbol{v}) \tag{87}$$

With $\boldsymbol{K}$ diagonal matrix $p \times p$ constituted by the positive coefficients, in order to have eigenvalues with negative real part, hence stable dynamics for the actuators. Finally, the system can be assembled in its augmented form given by in the augmented state $\boldsymbol{x}_a$ and new control vector $\boldsymbol{u}_a = [\boldsymbol{t} \quad \boldsymbol{v}]^T$

$$\dot{\boldsymbol{x}}_a = \begin{bmatrix} \boldsymbol{\phi}(\boldsymbol{x}) & \boldsymbol{\chi}(\boldsymbol{q}) \\ \boldsymbol{0}_{p\times n} & -\boldsymbol{K}\boldsymbol{q} \end{bmatrix} + \begin{bmatrix} \boldsymbol{B}_{\boldsymbol{\psi}} \\ \boldsymbol{K} \end{bmatrix} \begin{bmatrix} \boldsymbol{t} \\ \boldsymbol{v} \end{bmatrix} + \begin{bmatrix} \boldsymbol{C} \\ \boldsymbol{0}_{p\times 1} \end{bmatrix} \tag{88}$$

It is easy to notice that the augmented systems belongs to class of the control-affine systems seen previously, hence introducing $\boldsymbol{\phi}_a(\boldsymbol{x}_a)$ in the place of the state dependent matrix, calling $\boldsymbol{B}_a = [\boldsymbol{B}_{\boldsymbol{\psi}} \quad \boldsymbol{K}]^T$ and $\boldsymbol{C}_a = [\boldsymbol{C} \quad \boldsymbol{0}_{p\times 1}]^T$:

$$\dot{\boldsymbol{x}}_a = \boldsymbol{\phi}_a(\boldsymbol{x}_a) + \boldsymbol{B}_a\boldsymbol{u}_a + \boldsymbol{C}_a \tag{89}$$

Now the FLOP approach can be used, without any linearization for the control variable, moreover the actuators dynamic can be considered, but the dimension of the system is growth, causing a higher computational effort for simulation.

2.8 Inverted Pendulum case

The inverted pendulum is one of the challenging benchmarks used to test control algorithms [16, 20, 21, 23, 24]. The system is schematically represented in Figure :

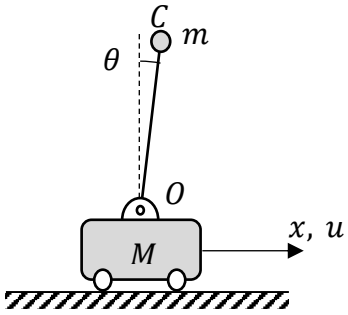

Figure 7: inverted pendulum

The variable used are described in Table :

Symbol	Description
M	Mass of the cart 0.5 [kg]
m	Mass of the pendulum 0.2 [kg]
l	Length of the pendulum 0.3 [m]
x	Position of the cart [m]
θ	Angular rotation [rad]
u	Force on the actuator [N]
g	Gravity Acceleration $[m/s^2]$

Table 2: Symbols and values used

The dynamical system is represented by the two coupled equations:

$$\begin{aligned}(m+M)\ddot{x} + ml\ddot{\theta}\cos\theta - ml\dot{\theta}^2\sin\theta = u \\ l\ddot{\theta} + \ddot{x}\cos\theta = g\sin\theta\end{aligned} \tag{90}$$

that reduced to the first order canonical form produces:

$$\dot{\boldsymbol{x}} = \boldsymbol{\phi}(\boldsymbol{x}) + \boldsymbol{h}(\boldsymbol{x})u \tag{91}$$

where:

$$\begin{aligned}&\boldsymbol{x} = \left[x, \theta, \dot{x}, \dot{\theta}\right]^T \qquad \boldsymbol{\phi}(\boldsymbol{x}) = \begin{bmatrix}\dot{x} \\ \dot{\theta} \\ \boldsymbol{M}(\boldsymbol{x})^{-1}\boldsymbol{P}(\boldsymbol{x})\end{bmatrix} \qquad \boldsymbol{h}(\boldsymbol{x}) = \begin{bmatrix}0 \\ 0 \\ \boldsymbol{M}(\boldsymbol{x})^{-1}\boldsymbol{d}\end{bmatrix} \\ &\boldsymbol{M}(\boldsymbol{x}) = \begin{bmatrix}M+m & ml\cos(\theta) \\ \cos(\theta) & l\end{bmatrix} \quad \boldsymbol{P}(\boldsymbol{x}) = \begin{bmatrix}ml\dot{\theta}^2\sin(\theta) \\ g\sin(\theta)\end{bmatrix} \quad \boldsymbol{d} = \begin{bmatrix}1 \\ 0\end{bmatrix}\end{aligned} \tag{92}$$

The FLOP requires $\boldsymbol{h}(\boldsymbol{x})$ linear, and a linearization about the final target position, i.e. $\boldsymbol{x}_T = \boldsymbol{0}$ is required, producing the simplified form:

$$\dot{\boldsymbol{x}} = \tilde{\boldsymbol{\phi}}(\boldsymbol{x}) + \boldsymbol{B}u + \boldsymbol{C}$$

with:

$$\begin{aligned}&\boldsymbol{B} = \boldsymbol{h}(\boldsymbol{x}_T) \\ &\tilde{\boldsymbol{\phi}}(\boldsymbol{x}) = \boldsymbol{\phi}(\boldsymbol{x}) + \boldsymbol{\mathcal{A}}\boldsymbol{x} \\ &\boldsymbol{\mathcal{A}} = \boldsymbol{\nabla}_{\boldsymbol{x}}(\boldsymbol{h}(\boldsymbol{x})u)|_{\boldsymbol{x}_T, u_T} \\ &\boldsymbol{C} = -\boldsymbol{\nabla}_{\boldsymbol{x}}(\boldsymbol{h}(\boldsymbol{x})u)|_{\boldsymbol{x}_T, u_T}\,\boldsymbol{x}_T \\ &u_T = 0\end{aligned} \tag{93}$$

2.8.1 Swing up controller

The functional to be minimized is:

$$J = \int_0^T \frac{1}{2}\boldsymbol{x}^T\boldsymbol{Q}\boldsymbol{x} + \frac{1}{2}\dot{\boldsymbol{x}}^T\boldsymbol{S}\dot{\boldsymbol{x}} + \frac{1}{2}Ru^2 + g(\boldsymbol{x}) + \boldsymbol{\lambda}^T\left(\dot{\boldsymbol{x}} - \left(\widetilde{\boldsymbol{\phi}}(\boldsymbol{x}) + \boldsymbol{B}u + \boldsymbol{C}\right)\right)\,dt \tag{94}$$

where $g(\boldsymbol{x})$ is suitably chosen θ-dependent to better perform the swing up manoeuvre. The $g(\boldsymbol{x})$ shaping is aimed at introducing a local potential-attractive function at the upward position of the pendulum, and a local potential-repulsive function at the downward pendulum position. The sum of three Gaussian-like functions is useful to obtain this goal:

$$g(\theta) = -k_1 e^{-\alpha_1\theta^2} + k_2 e^{-\alpha_2(\theta+\boldsymbol{\pi})^2} + k_3 e^{-\alpha_3(\theta-\boldsymbol{\pi})^2} \tag{95}$$

The last two terms are due to the downward position that can be reached for clockwise or anti-clockwise rotations, and k_i and α_i are used as tuning parameters.

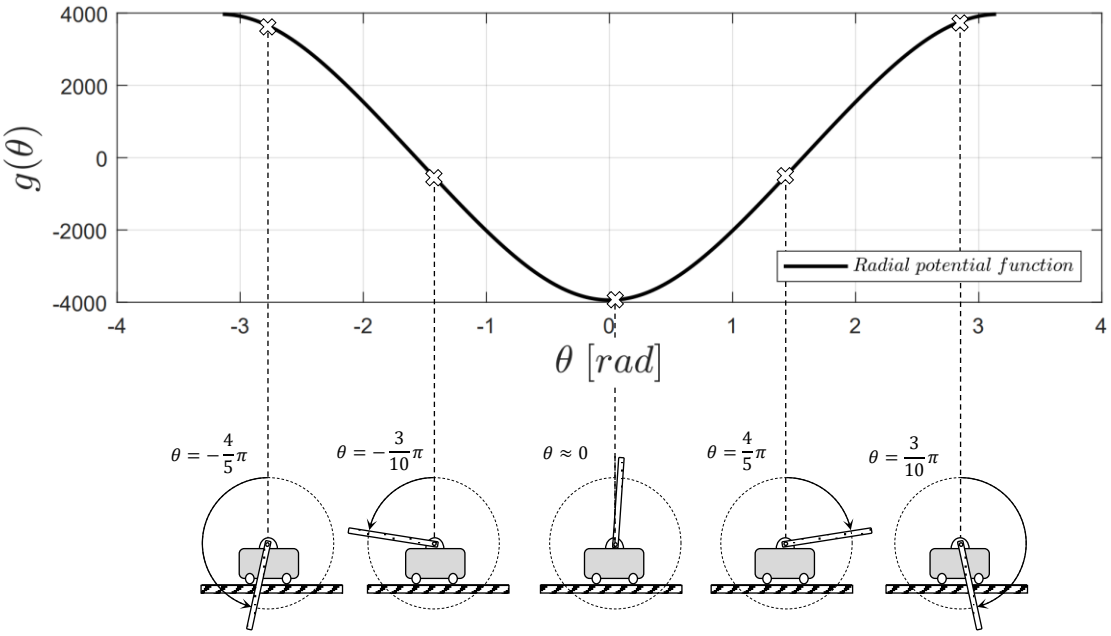

Figure 8: inverted pendulum penalty function

The FLOP formulation (84) leads to a control feedback:

$$u^* = f(\boldsymbol{Q}, \boldsymbol{S}, \boldsymbol{R}, \boldsymbol{G}, g(\theta), \boldsymbol{x}) \tag{3}$$

specifically:

$$u^* = (\boldsymbol{R}^T + \boldsymbol{B}^T\boldsymbol{S}\boldsymbol{B})^{-1}\,\boldsymbol{B}^T\left(\boldsymbol{\lambda} - \boldsymbol{S}\widetilde{\boldsymbol{\phi}}(\boldsymbol{x}) - \boldsymbol{S}\boldsymbol{B}\boldsymbol{u}_T - \boldsymbol{C}\right) + \boldsymbol{u}_T$$

with

$$\begin{aligned}
&\boldsymbol{u}_T = -\boldsymbol{B}^+\left[\widetilde{\boldsymbol{\phi}}(\boldsymbol{x}_T) + \boldsymbol{C}\right] \\
&\boldsymbol{\Phi}(\boldsymbol{x}) = \boldsymbol{\nabla}_{\boldsymbol{x}}\widetilde{\boldsymbol{\phi}}(\boldsymbol{x}) \\
&\boldsymbol{\gamma}(\boldsymbol{x}) = \boldsymbol{\nabla}_{\boldsymbol{x}} g(\boldsymbol{x})
\end{aligned} \tag{97}$$

$$\boldsymbol{\lambda = \widetilde{A}^{-1}\Big[Q^T(x - x_T) + \gamma^T(x - x_T) + \Phi(x)^T S\big[\widetilde{\phi}(x) - B\big[R_1^{-1}B^T\big(S\widetilde{\phi}(x) + SBu_T + C\big) - u_T\big] + C\big]\Big]}$$

$$\boldsymbol{R_1 = R^T + B^T SB}$$

$$\boldsymbol{\widetilde{A} = [\Phi(x)^T(I - SBR_1^{-1}B^T) + G]}$$

$$\boldsymbol{G = -\frac{1}{\Delta\tau}I}$$

As usual in optimal control, also the FLOP method needs an optimization procedure to determine the best values for $\boldsymbol{Q, S, R, G}$ k_i and α_i, that are tested analysing the control features of the controller, as shown in the next sections.

2.8.2 Numerical results

In Table the tuning parameters and their values used in the numerical simulations are listed.

Tuning parameters	Value
$\boldsymbol{Q}$	$\begin{bmatrix} 10 & 0 & 0 & 0 \\ 0 & 0 & 0 & 0 \\ 0 & 0 & 8 & 0 \\ 0 & 0 & 0 & 0 \end{bmatrix}$
$\boldsymbol{S}$	$\begin{bmatrix} 24 & 0 & 0 & 0 \\ 0 & 100 & 0 & 0 \\ 0 & 0 & 22 & 0 \\ 0 & 0 & 0 & 7 \end{bmatrix}$
R	1
$\boldsymbol{k} = [k_1, k_2, k_3]$	$[\,80, 4, 4]$
$\boldsymbol{\alpha} = [\alpha_1, \alpha_2, \alpha_3]$	$[0.125, 50, 50]$

Table 3: Parameters used

The FLOP controller is tested by numerical simulations to observe its performances, robustness and effectiveness in bringing the pendulum in its upper position. Limitations are imposed on both the maximum actuation force u_{max} .The actuator transfer function is represented by $1/(1 + \tau s)$ with $\tau = 0.1s$. The monitored variables are the position of the carriage, the angular rotation of the pendulum and their derivatives, and the control force u.
Figure shows four different cases of swing up:
Case 1 uses the FLOP controller for reaching the target position. Once the pendulum holds the target, case 4 introduces an additional impulse disturbance to test the robustness of the control. Cases 1 and 4 show the same trend and are overlapped until about t=15s, when the pendulum disturbance is injected. Both start to oscillate around the equilibrium position and carry out the ascent manoeuvre that ends after only 7 seconds of oscillation. The cart moves only 20 cm from the origin, exploiting

maximum actuator accelerations less than 0.2g. In case 4, the cart reacts quickly to the impulse disturbance in such a way it keeps the upper position of the rod stable.
Case 3 introduces a perturbation in the parameters of the system during the simulations, without updating the controller information. In fact, to validate the control robustness, random positive or negative variations of 10% are imposed on the mass of the carriage, mass and length of the rod, while maintaining constant the tuning parameters of the control logic.
Case 2 introduces a swing up test starting from the initial pendulum conditions $\theta = \pi/2$. This condition is simpler to control because the pendulum, even without an external control action, starts naturally to oscillate and is pulled up in less than one second, keeping the carriage travel very limited near the origin.
Finally, to verify further the robustness of the controller, a large set of simulation with random initial conditions are performed changing the initial speed of both, the cart and the rod, and assuming different angular rod positions Figure . The control has proven to work in all cases bringing both the cart and the rod to the desired target position.
Figure and 12 show, for different initial conditions, a comparison between FLOP and a nonlinear control logic based on energy [16]. This technique uses the fusion of two controls, the first, of Lyapunov type, used when the pendulum is at its lower position and the second, LQR-based, intervenes when a set threshold of angle near the origin is exceeded. The upper limit for u_{max} is equal to 5N, and the characteristic time of the actuator is $\tau = 0.01s$.
The energy-based control is formulated as follows:

$$u_{energy} = \begin{cases} -\boldsymbol{K}_{LQR}\boldsymbol{x} & |\theta| < \varepsilon \\ sat_{u_{max}}(\mu(E - E_r)sign(\dot{\theta}\cos\theta)) & otherwise \end{cases} \quad (98)$$

where $\boldsymbol{K}_{LQR}, E,\ E_r, \mu, \varepsilon$ are the Riccati gain of LQR, the instantaneous potential and kinetic energy of the pendulum, the reference energy of the upward position and the last two terms are tuning parameters.
The switch threshold in the energy method is set to ε = 30°. Both controls behave well, and the energy method can pull up the pendulum in a very short time if it starts from the rest condition. In the case illustrated in Figure in which the pendulum starts from rest condition at π, the energy method, although very reactive in the swing up operation, needs to displace the cart of almost 2 meters from the origin. The FLOP method, instead, shows a very small cart displacement, about 50cm away from the origin. The FLOP control is slow only when starting from the rest condition, but it demonstrates an excellent control ability in the swing up maneuver, involving very small movements of the cart when compared with the energy method.

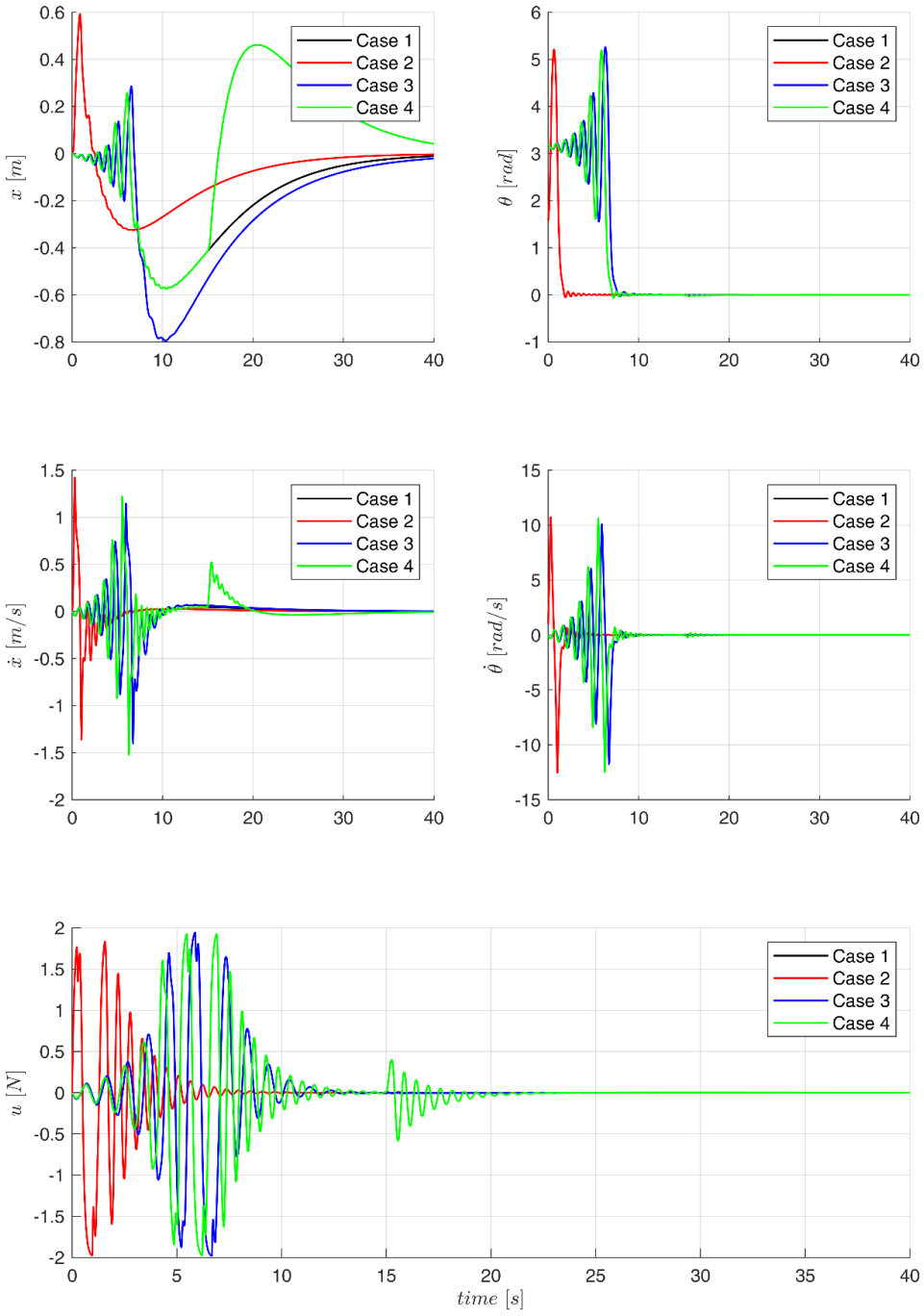

Figure 9: Swing-up maneuver with perturbed parameters

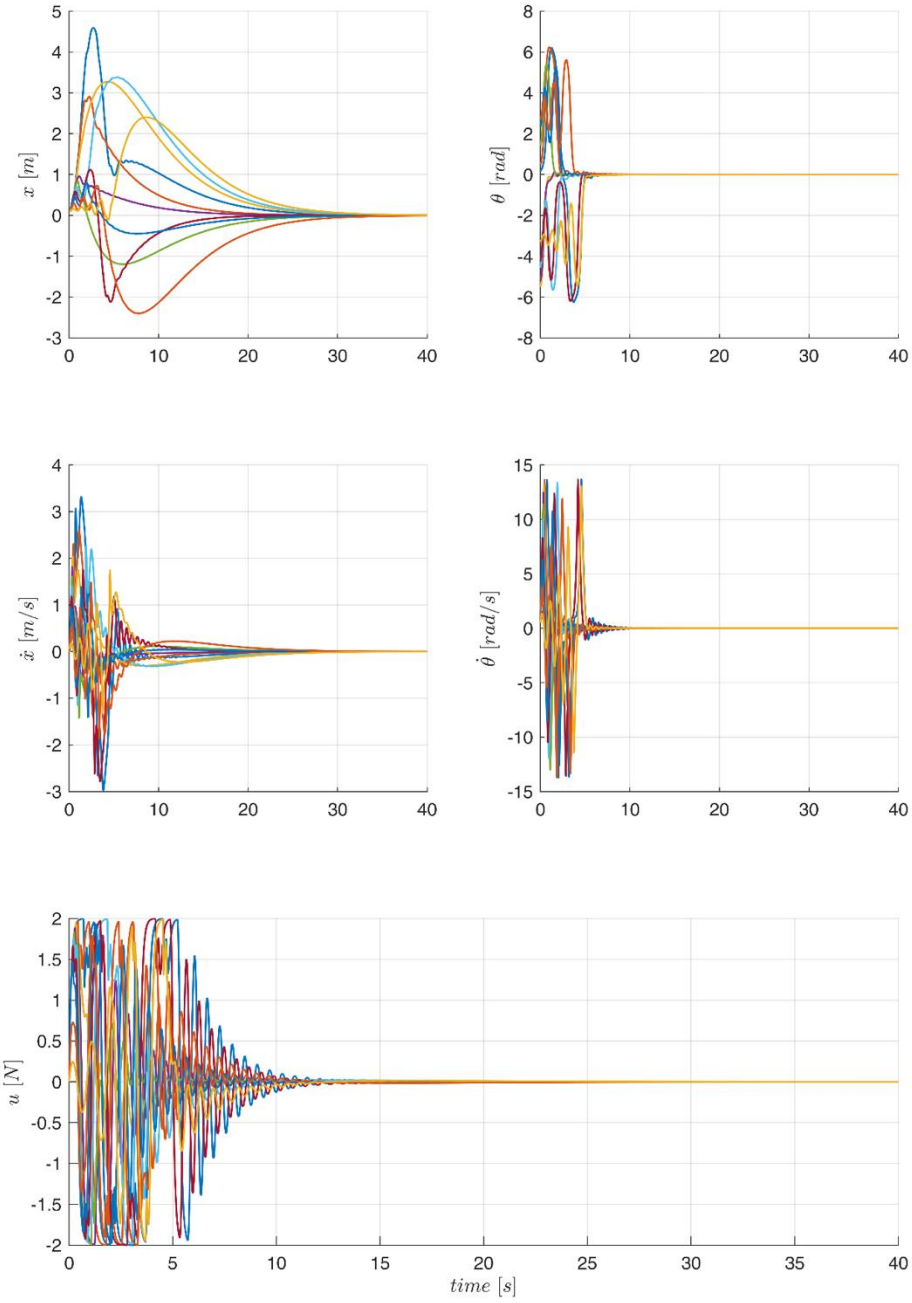

Figure 10: Swing-up maneuver with different initial conditions

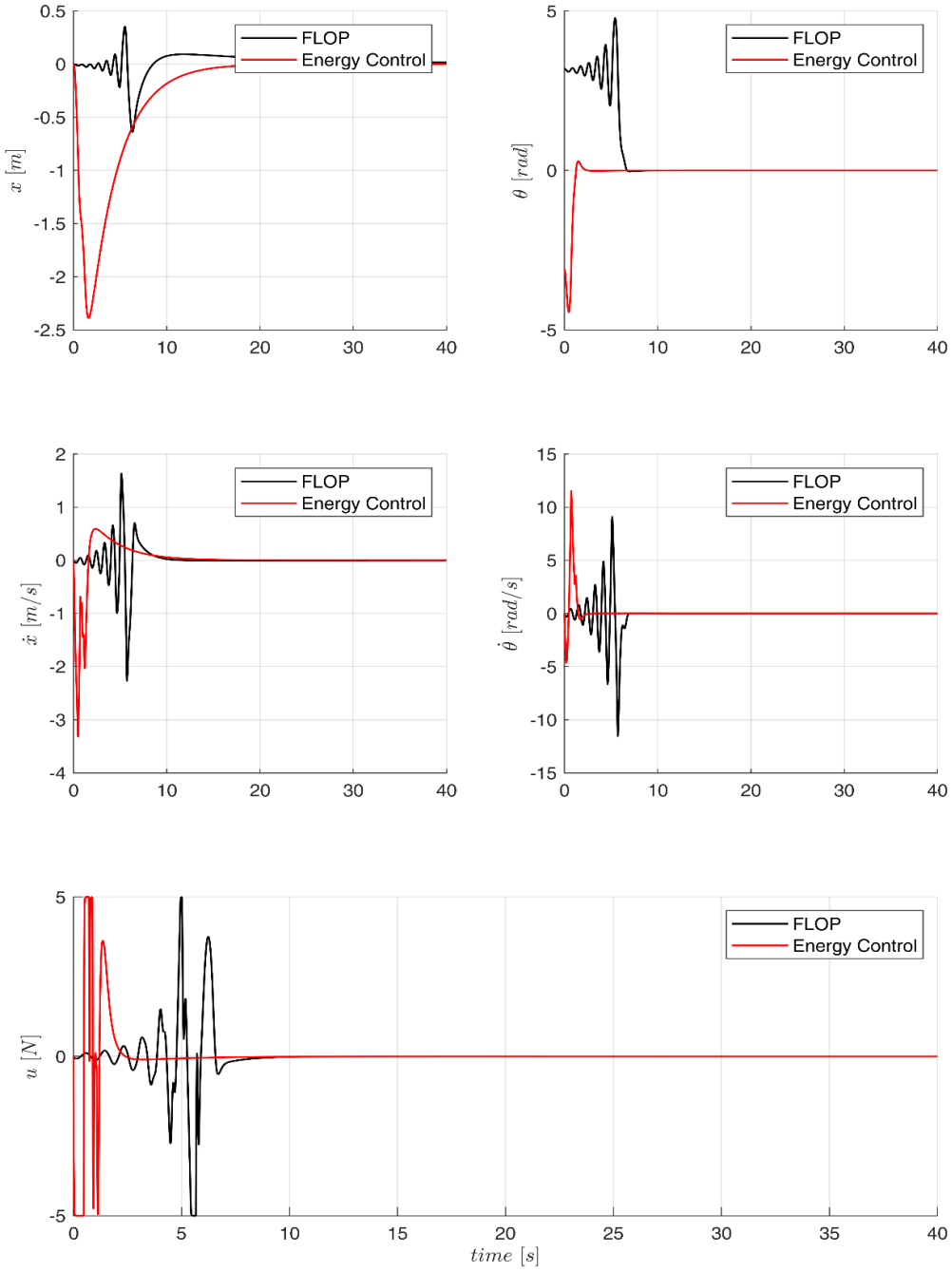

Figure 11: Swing-up maneuver: FLOP vs energy method, initial condition $\theta_0 = \pi$

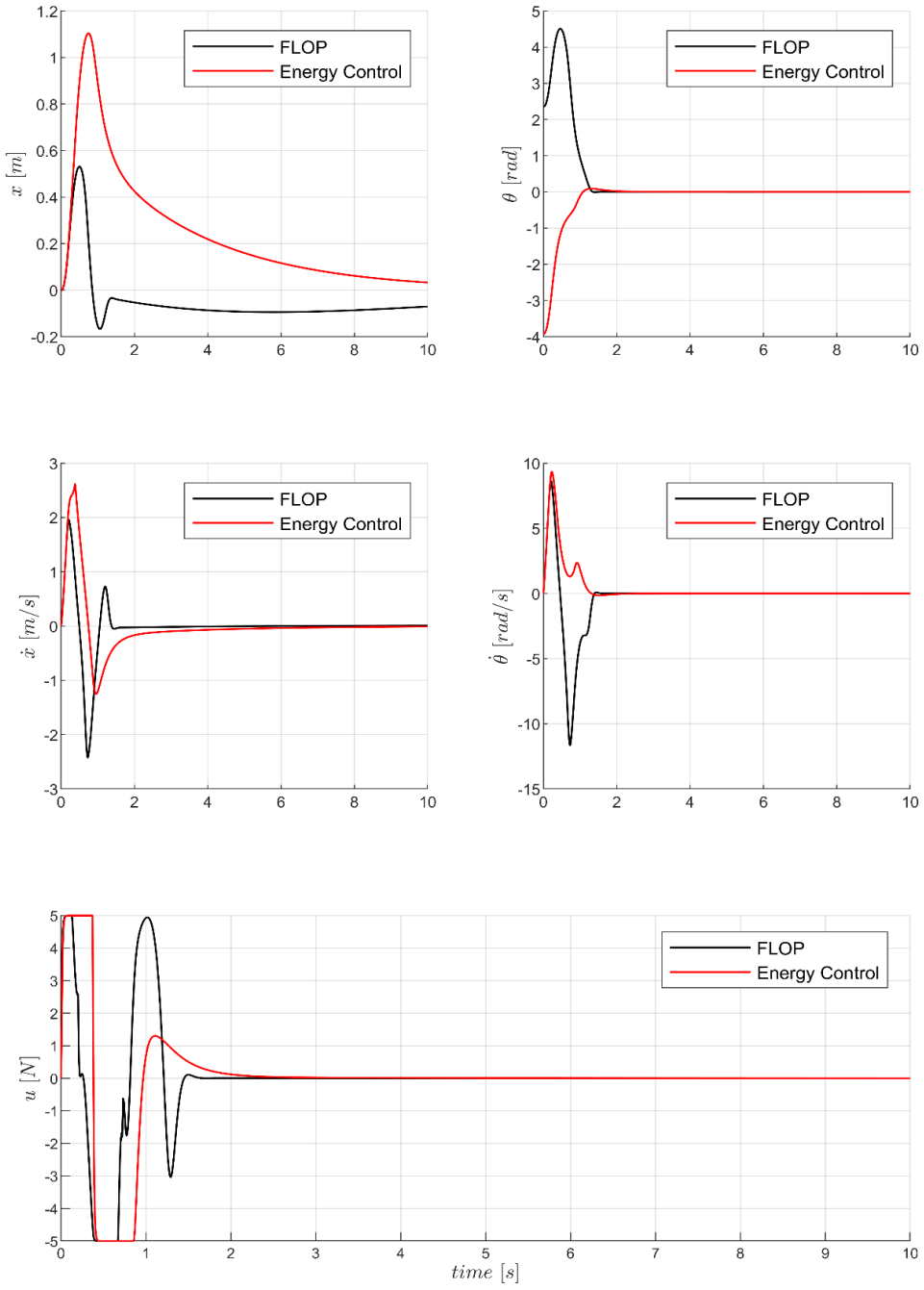

Figure 12: Swing-up maneuver: FLOP vs energy method, initial condition $\theta_0 = \pi 3/4$

The FLOP method is applied to control an inverse pendulum showing robustness and effectiveness for the swing up maneuver. The control, thanks to its formulation, allows to choose how the pendulum is accompanied and maintained in the upper position. In fact, in the objective function it is possible to create customized potential functions allowing different control behaviors, such as managing the initial oscillations of the pendulum in the downward position, differently from the maintenance of the upward position. The comparison with Lyapunov control law method mixed to LQR control shows that the FLOP provides better performance.

Chapter 3

La Sapienza Autonomous car project

3.1 Autonomous Vehicles research project

Nowadays, autonomous vehicle (AV) represents a crucial field in intelligent transportation systems. In recent years, integrated control of in-wheel motor and assisted-steering is a subject of central interest [44-47] in automotive technology, and the introduction of active devices in place of the traditional passive components can improve vehicle dynamics as in the case of the semi active suspension [33,35,38,40].
This work is addressed to the analysis of an autonomous vehicle as a first step of an on-going project at the Mechatronic and Vehicle Dynamic Lab of Sapienza []. The project is developing an experimental setup for a series city car to be equipped with a complete assisted integrated system of mechatronic type, controlling the steering and the wheel torques. a bike-model for its dynamic response is considered, including the car body dynamics, suspensions and tires that can rely on the previous controls and on a control logic that is based on a new strategy, the FLOP control. This kind of control, recently developed by the Sapienza team, relies on optimal control theory of Pontryagin type [9-16], that has been revisited transforming the global optimality problem into a set of local optima along the system trajectory. This method provides a chance for an efficient feedback control of the vehicle in an environment in which moving obstacles and external noise are present.
The FLOP method is here implemented to control the steering radius in a turning maneuver. The goal is to track, at the possible maximum speed, the assigned trajectory maintaining a given steering radius. The numerical results show the good performances of the new control in a rather complex scenario.

3.2 Dynamic Model of the Vehicle

In this section, a standard three-DOF nonlinear bike model, depicted in Figure 13, is considered. The vehicle motion is assumed planar and including the longitudinal forward motion (u), the lateral sway (v), and the yaw (ψ). The equations of motion are expressed in the body reference frame. The rear wheel steering angle is set to zero, while the front one is δ. The center of gravity of the vehicle is CG. The distances of points A (center of front wheel) and B (center of rear wheel) from CG are l_f and l_r, respectively. The wheelbase is $L = l_f + l_r$. The velocity of CG is V, the angle between the velocity vector $of\ CG$ and the longitudinal axis of the vehicle u is β.

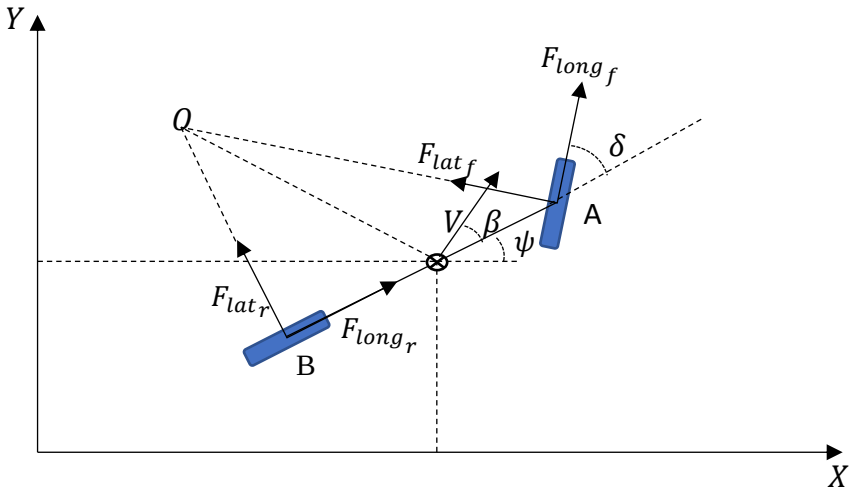

Figure 13: Bike model

The state vector is $\boldsymbol{x} = [X; Y; \psi; u; v; \omega; \omega_r; \omega_r]$, where X, Y are the coordinates of CG in the road reference, while ψ is the yaw rotation angle, u, v, ω, are the speed components measured in the body fixed reference, representing the surge, sway, and yaw motions. The longitudinal and lateral slips of the wheels depend both on the spin speeds ω_r, ω_r , for the rear and front wheel, respectively. The equations of motion of the vehicle can be written in terms of the state defined above. The system has three degrees of control, the steering angle of the front wheel δ, the rear torque C_r and the front torque C_f. The inertia matrix can be written in terms of the body mass m_b summed with wheels masses m_w in m, the yaw moment of inertia I_z, the wheels inertia moments I_w

$$\boldsymbol{M} = diag[1; 1; 1; m; m; I_z; I_w; I_w] \tag{99}$$

This leads to the following expressions for the $\dot{\boldsymbol{x}} = \left[\dot{X}; \dot{Y}; \dot{\psi}; \dot{u}; \dot{v}; \dot{\omega}; \dot{\omega}_r; \dot{\omega}_r\right]^T$. The speeds of the vehicle, in the fixed reference can be written through the 2D rotation matrix which is function of the yaw angle ψ that converts the speeds of the vehicle from the body reference frame to the fixed reference frame.

$$\begin{bmatrix} \dot{X} \\ \dot{Y} \\ \dot{\psi} \\ \dot{u} \\ \dot{v} \\ \dot{\omega} \\ \dot{\omega_r} \\ \dot{\omega_f} \end{bmatrix} = \boldsymbol{M}^{-1} \begin{bmatrix} \cos(\psi)\, u - \sin(\psi) v \\ \sin(\psi)\, u + \cos(\psi) v \\ \omega \\ F_{long_f} \cos(\delta) - F_{lat_f} \sin(\delta) + F_{long_r} + mv\omega - F_{aero} \\ F_{long_f} \sin(\delta) + F_{lat_f} \cos(\delta) + F_{lat_r} - mu\omega \\ F_{long_f} \sin(\delta)\, l_f + F_{lat_f} \cos(\delta)\, l_f - F_{lat_r} l_r \\ C_r - F_{long_r} R_w - F_{rolling_r} R_w \\ C_f - F_{long_f} R_w - F_{rolling_f} R_w \end{bmatrix} \tag{100}$$

The terms F_{long_f} and F_{long_r} represent the Pacejka longitudinal front and rear forces evaluated in function of the normal force acting on the tires and of the longitudinal slip ratio σ_f and σ_r

$$F_{long_f} = f(F_{N_f}, \sigma_f(u_f, \omega_f, \delta)) \tag{101}$$

$$F_{long_r} = f(F_{N_r}, \sigma_r(u_r, \omega_r))$$

$$\sigma_f = -\frac{u_f - \omega_f R_w}{|u_f|}$$

$$\sigma_r = -\frac{u_r - \omega_r R_w}{|u_r|}$$

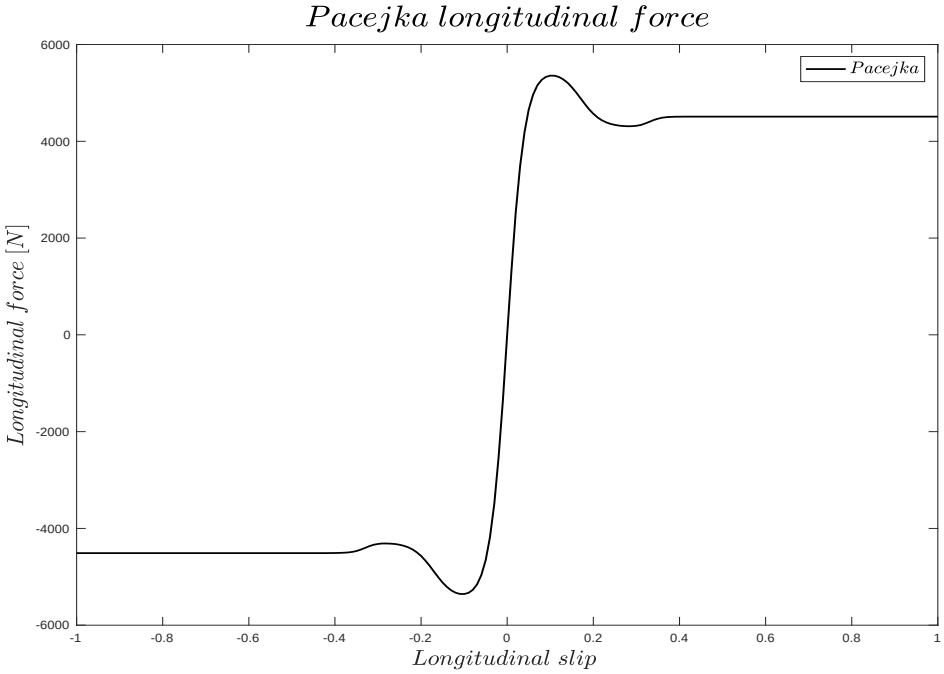

Figure 14: Pacejka longitudinal force model

The aerodynamic drag is expressed through the following model:

$$F_{aero} = \frac{1}{2}\rho_{air} A_{section} C_d u^2 \tag{102}$$

The rolling resistance of the tires are represented by two forces, $F_{rolling_f}$ and $F_{rolling_r}$ defined as:

$$\begin{aligned} F_{rolling_f} &= \left(\mu_0 + \mu_1 u_f^2\right) F_{N_f} \\ F_{rolling_r} &= \left(\mu_0 + \mu_1 u_r^2\right) F_{N_r} \end{aligned} \tag{103}$$

where u_f and u_r are the longitudinal speed of the front and rear wheels, respectively, in the body fixed reference frame:

$$\begin{aligned} u_f &= \cos(\delta)\, u - \sin(\delta)\left(v + l_f \omega\right) \\ u_r &= u \end{aligned} \tag{104}$$

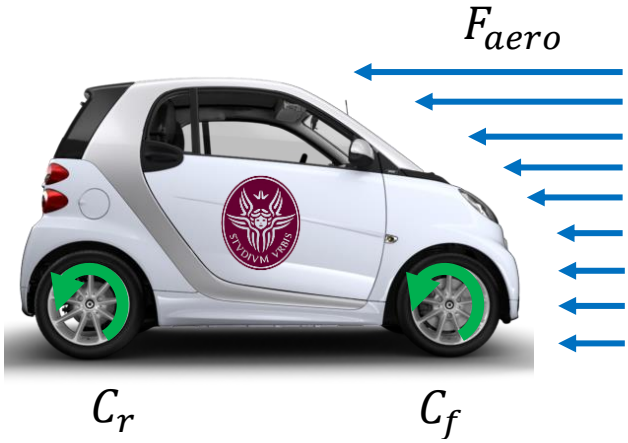

Figure 15: Rolling resistance and aerodynamic drag acting on the vehicle

The lateral sway motion forces are F_{lat_f} and F_{lat_r}. They depend on the lateral slip ratios α_f and α_r

$$
\begin{aligned}
F_{lat_f} &= f\left(F_{N_f}, \alpha_f(\hat{u}, \hat{v}, \omega, \delta)\right) \\
F_{lat_r} &= f\left(F_{N_r}, \alpha_r(\hat{u}, \hat{v}, \omega)\right) \\
\alpha_f &= -\operatorname{atan}\left(\frac{\left(\hat{v} + \omega l_f\right)\cos(\delta) - \hat{u}\sin(\delta)}{\hat{u}\cos(\delta) + \left(\hat{v} + \omega l_f\right)\sin(\delta)}\right) \\
\alpha_r &= -\operatorname{atan}\left(\frac{(\hat{v} - \omega l_r)}{\hat{u}}\right)
\end{aligned}
\tag{105}
$$

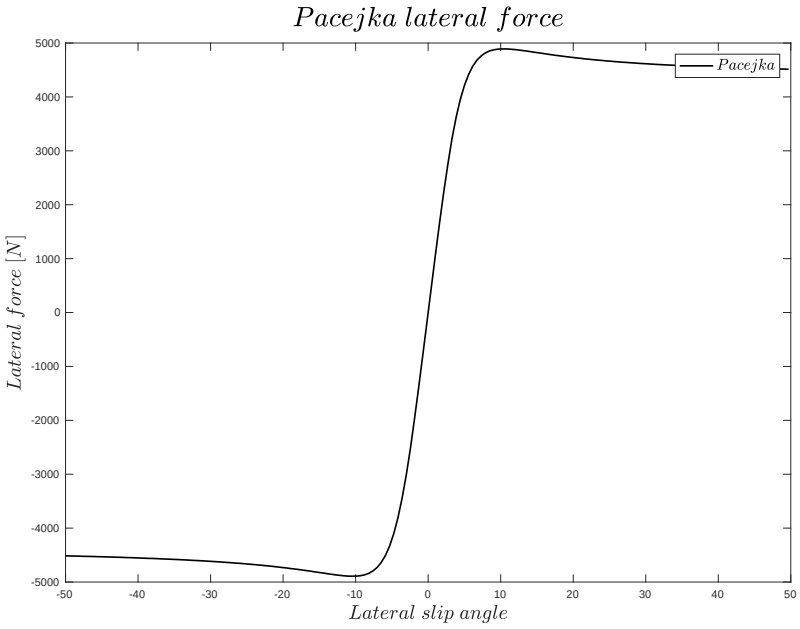

Figure 16: Pacejka lateral force model

The estimation of the tire's grip and rolling resistance, can be performed even in feedback by using advanced intelligent tires provided with sensors. Finally, the vertical forces F_{N_f} and $F_{N_r}$are:

$$F_{N_f} = \frac{m}{L}\left(g l_r - (\dot{u} - v\omega)h_g\right) - \frac{F_{aero}h_g}{L} - \frac{\left(C_r + C_f\right)}{L}$$
$$F_{N_r} = mg - F_{N_f} = mg - \frac{m}{L}\left(g l_r - (\dot{u} - v\omega)h_g\right) + \frac{F_{aero}h_g}{L} + \frac{\left(C_r + C_f\right)}{L} \qquad (106)$$

3.3 Cruise Control, a test case to introduce control limits

The first application of the FLOP control law considered in this project is the cruise control, this kind of actuation provides the car with a system, that acting on control of fuel permits to it to reach and maintain the specified value of the forward speed u, since it doesn't require specific hardware it is diffused on most of the actual production car, but in general commercial solutions aren't based on optimal control law, Optimal control class can lead to a more efficient systems in terms of fuel consumption hence less pollutions. This case represents a suitable candidate to introduce a nonlinear penalty function $g(\boldsymbol{u})$ on the control variable $\boldsymbol{u}$, to introduce actuators limits i.e. the maximum driving torque and the maximum braking torque, that can be provided to the wheels. As shown in the following is not easy to solve analytically for the variable $\boldsymbol{u}$ hence a numerical solution will be employed in the place of the analytical one. The bike model previously defined reduced by considering only the differential equation of the forward motion of the vehicle, and the differential equation that describe the wheel dynamic, given the fact that the cruise control regards only the forward motion of the vehicle, hence the state of the system is represented by $\boldsymbol{x} = [u; \omega_r; \omega_f]$, neglecting the lateral motion of the vehicle hence the lateral forces:

$$\begin{aligned} \dot{u} &= \frac{1}{m}\left(F_{long_f} + F_{long_r} - F_{aero}\right) \\ \dot{\omega_r} &= \frac{1}{I_w}\left(C_r - F_{long_r}R_w - F_{rolling_r}R_w\right) \\ \dot{\omega_f} &= \frac{1}{I_w}\left(C_f - F_{long_f}R_w - F_{rolling_f}R_w\right) \end{aligned} \qquad (107)$$

The control vector $\boldsymbol{u}$ is represented by the two torques C_r, C_f represent the two degrees of control of the system, hence the vehicle is supposed to be four-wheel drive, while the inertia terms, the contact forces, the rolling resistance model and the aerodynamic drag are identical to those provided in the previous section.
Now the performance index J contains in this case, both the quadratic cost function written in terms of the state target state $\boldsymbol{x}_T$ i.e. $\left[u_T; \omega_{r_T}; \omega_{f_T}\right]$, and in terms of the penalty function on the control variables $g(\boldsymbol{u})$

$$J = \int_0^T \frac{1}{2}(\boldsymbol{x} - \boldsymbol{x}_T)^T \boldsymbol{Q}(\boldsymbol{x} - \boldsymbol{x}_T) + \frac{1}{2}(\boldsymbol{u} - \boldsymbol{u}_T)^T \boldsymbol{R}(\boldsymbol{u} - \boldsymbol{u}_T) + g(\boldsymbol{u}) + \boldsymbol{\lambda}^T\left(\dot{\boldsymbol{x}} - (\boldsymbol{\phi}(\boldsymbol{x}) + \boldsymbol{B}\boldsymbol{u})\right) dt \qquad (108)$$

The $g(\boldsymbol{u})$ function is represented by sum of potential gaussian function centered on the limits of actuation for the driving torque and for the braking torque:

$$g(\boldsymbol{u}) = \frac{amp_{braking}}{\sqrt{2\pi}\sigma_{braking}} e^{\left(-\frac{1}{2}\left(\frac{C_r - C_{Blmit}}{\sigma_{braking}}\right)^2\right)} + \frac{amp_{braking}}{\sqrt{2\pi}\sigma_{braking}} e^{\left(-\frac{1}{2}\left(\frac{C_f - C_{Blmit}}{\sigma_{braking}}\right)^2\right)} + \frac{amp_{driving}}{\sqrt{2\pi}\sigma_{driving}} e^{\left(-\frac{1}{2}\left(\frac{C_r - C_{Dlmit}}{\sigma_{driving}}\right)^2\right)} + \frac{amp_{bracking}}{\sqrt{2\pi}\sigma_{bracking}} e^{\left(-\frac{1}{2}\left(\frac{C_f - C_{Dlmit}}{\sigma_{driving}}\right)^2\right)} \tag{109}$$

The limit for braking torque is represented by C_{Blmit}, the one for driving torque is represented by C_{Dlmit}, while the parameters $amp_{bracking}, amp_{driving}, \sigma_{bracking}, \sigma_{driving}$ are to be suitably chosen in order to get the best performance.
The set of equation obtained by applying the variational calculus becomes:

$$\begin{cases} \boldsymbol{Q}^T(\boldsymbol{x} - \boldsymbol{x}_T) - \boldsymbol{\nabla\phi}(\boldsymbol{x})^T\boldsymbol{\lambda} = \dot{\boldsymbol{\lambda}} \\ \boldsymbol{R}^T\boldsymbol{u} - \boldsymbol{B}^T\boldsymbol{\lambda} + \boldsymbol{\nabla} g(\boldsymbol{u})^T = 0 \\ \dot{\boldsymbol{x}} = \boldsymbol{\phi}(\boldsymbol{x}) + \boldsymbol{B}\boldsymbol{u} \\ \dot{\boldsymbol{\lambda}} = \boldsymbol{G}\boldsymbol{\lambda} \end{cases} \tag{110}$$

That in general, cannot provide an explicit expression for the control vector $\boldsymbol{u}$, hence in this case only a numerical solution can provide the desired control.

3.4 Steering control strategies, kinematic vs potential approach

In order to investigate the steering capabilities of the FLOP approach, two different strategies were investigated, the first strategy relies on the actual turning radius performed by the vehicle, by introducing it through a $g(\boldsymbol{x})$ penalty function centered at a reference value for the turning radius. The cost function in the FLOP method is assumed to be:

$$\bar{J} = \int_0^T \frac{1}{2}\boldsymbol{u}^T\boldsymbol{R}\boldsymbol{u} + g(\boldsymbol{x}) + \boldsymbol{\lambda}^T\left(\dot{\boldsymbol{x}} - \boldsymbol{f}(\boldsymbol{x}, \boldsymbol{u})\right) dt \tag{111}$$

where $g(\boldsymbol{x})$ can represent any kind of possible nonlinear and continuous function. This permits the user to define $\bar{J}$ as:

$$g(\boldsymbol{x}) = g_r(\boldsymbol{x}) + g_s(\boldsymbol{x}) + g_c(\boldsymbol{x}) = k_r\left(t_r(\boldsymbol{x}) - t_{reference}\right)^2 + \frac{ampS}{\sigma_s\sqrt{2\pi}} \exp\left(-0.5\left(\frac{V(\boldsymbol{x}) - V_{min}}{\sigma_s}\right)^2\right) \tag{112}$$

$g_r(\boldsymbol{x})$ shown in fig 18 is a quadratic form of the $t_r(\boldsymbol{x})$; $t_{reference}$ these represent the actual turning radius and its reference value. $t_r(\boldsymbol{x})$ is function of the state $\boldsymbol{x}$, and can be easily evaluated in term of the absolute speed V of the vehicle and the yaw rate $\dot{\psi}$ using the following formula:

$$t_r(\boldsymbol{x}) = \frac{V}{\dot{\psi}} \tag{113}$$

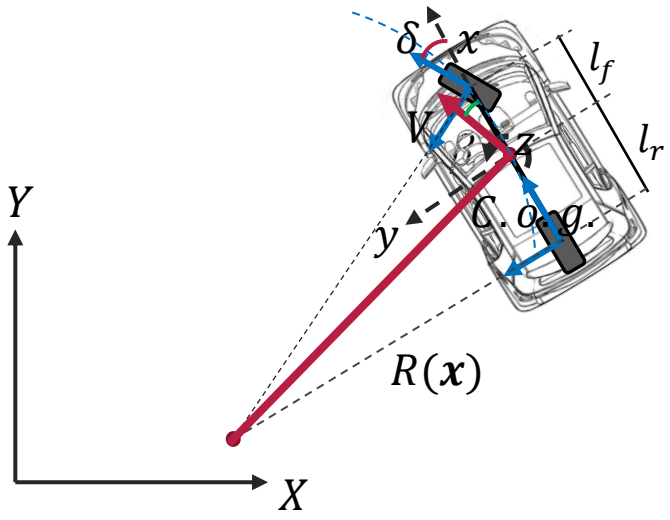

Figure 17: Actual turning radius

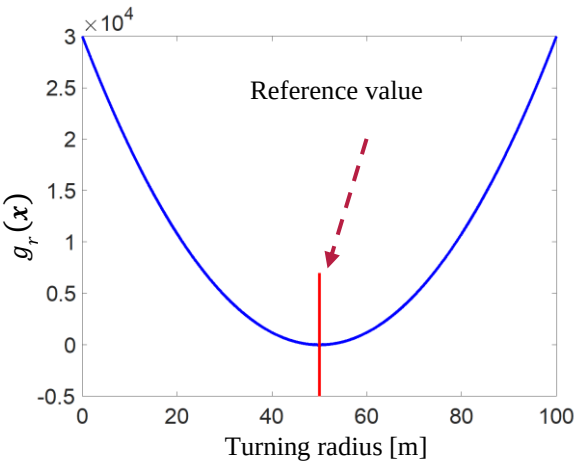

Figure 18: $g_r(\boldsymbol{x})$ function for various turning radius

The function $g_S(\boldsymbol{x})$ shown in fig 19 is a gaussian function of the vehicle absolute speed V and of a minimum speed V_{min}.

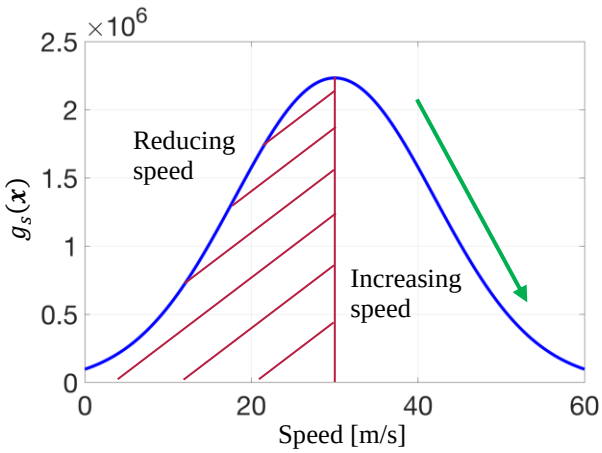

Figure 19: $g_s(\boldsymbol{x})$ function for various speed

The second strategy uses a pre-defined trajectory (an information provided by sensors). More precisely, given a desired trajectory (for example the shape of a circuit, as in figure 20) a potential function can be shaped (for example using Gaussian-like functions) that introduces a high penalty when the vehicle position approaches the boundaries of the track.

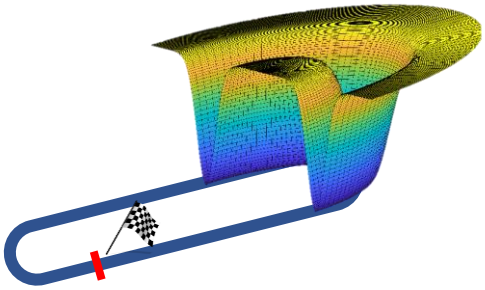

Figure 20: Potential surface track strategy

In this case the penalty function $g(\boldsymbol{x})$ is written in terms of the actual vehicle position on the track and it is centered on the pre-defined trajectory, for example in the case of simple turn, it might be written as:

$$\begin{gathered} X_{turn} = x_{center} + \rho\cos(\theta) \\ Y_{turn} = y_{center} + \rho\sin(\theta) \\ \rho = \sqrt{(x - x_{center})^2 + (y - y_{center})^2} \quad , \quad \theta = \operatorname{atan}\left(\frac{y - y_{center}}{x - x_{center}}\right) \\ g(\boldsymbol{x}) = \frac{ampTrack}{\sigma_{track}\sqrt{2\pi}} \exp\left(-0.5\left(\frac{\sqrt{(X_{turn} - x_{center})^2 + (Y_{turn} - y_{center})^2} - \rho_{reference}}{\sigma_{track}}\right)^2\right) \end{gathered} \tag{114}$$

Where X_{turn}, Y_{turn} represents the actual position of the vehicle on the turn centered in x_{center}, y_{center}. ρ and θ are the actual radial and angular positions of the vehicle in that specific turn while $ampTrack, \sigma_{track}$ parameters that must be chosen.

3.5 Results, high speed cornering

In this section some numerical simulations are shown. The first set shows the cornering capability and the obstacle avoidance performance, this last being the most challenging and critical for an autonomous vehicle.
Fig. 21 illustrates the capability of the vehicle to follow a corner with specific turning radius, fixed by the user to 70 m.

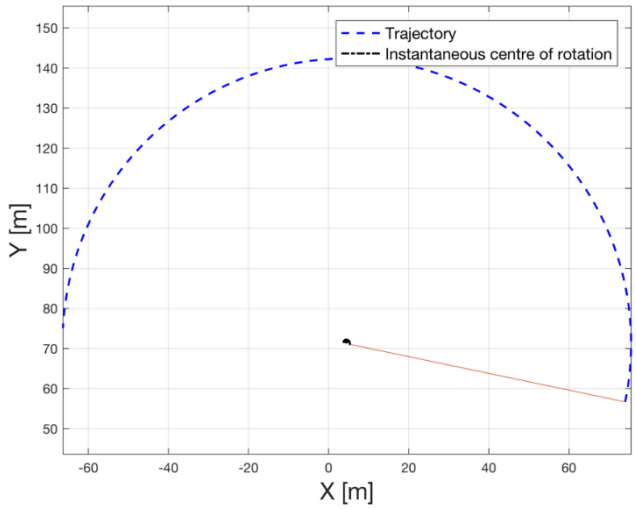

Figure 21: Trajectory analysis

Fig. 22 visualizes small perturbations of the position of the center of instantaneous rotation in comparison with the radius of curvature.

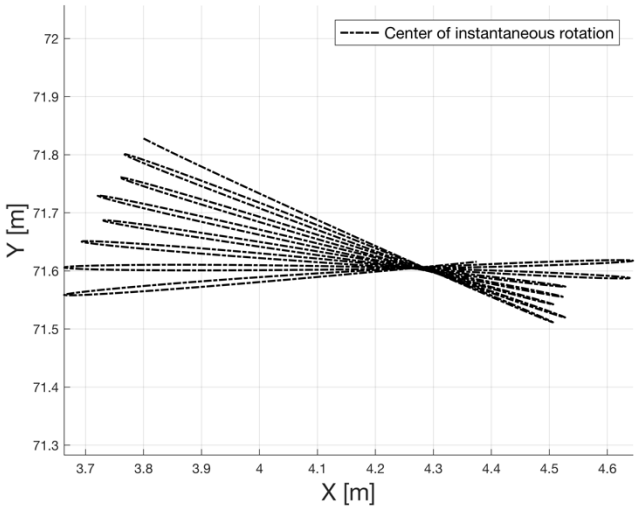

Figure 22: Center of instantaneous rotation

Fig. 23 reports the highest speed reached by the vehicle for various steering angles. Moreover, the time history of the speed for one of the vehicle's maneuver is represented with the black curve to show the stability of the controlled vehicle. The blue curve represents the highest speed reached by the controlled vehicle and it is compared to the maximum speed obtained equating the maximum lateral adherence force reachable by the Pacejka's forces with the centrifugal force, for various turning radius:

$$F_{long_f}\sin(\delta) + F_{lat_f}\cos(\delta) + F_{lat_r} = \frac{mV^2}{R} \tag{115}$$

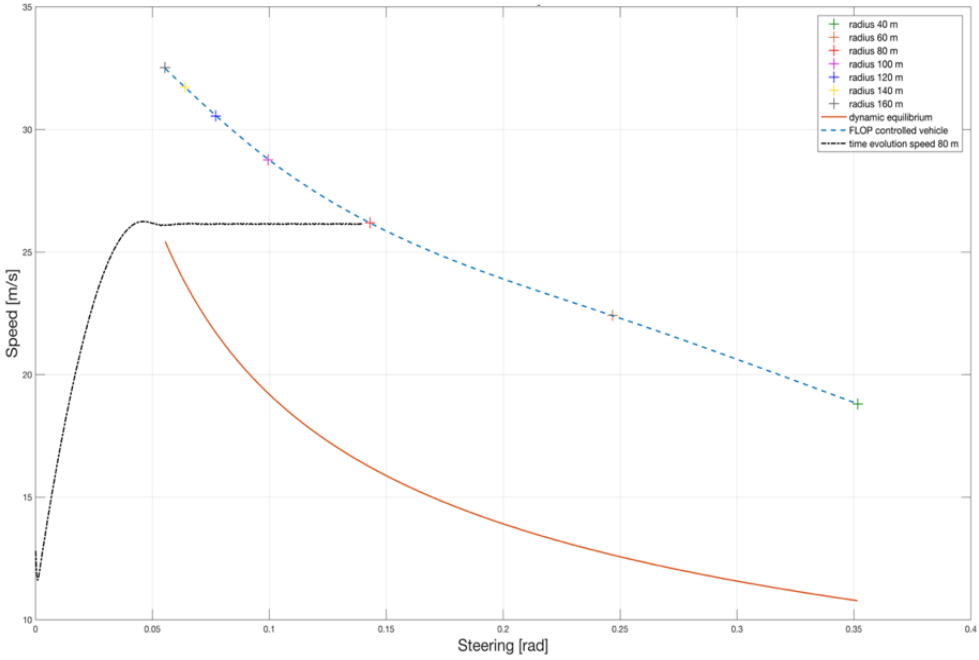

Figure 23: $g_s(\boldsymbol{x})$ function for various speed

The following figures illustrate the reaction in case of an obstacle placed along the trajectory of the vehicle, this is compared to the free-way case (compare figures 24 and 25). This shows the different trajectories, different turning radius, longitudinal and lateral speeds, lateral slip angles of the body and tires and in terms of Pacejka's forces.
The starting point of the variation is represented by the magenta marker placed within the plot. It is interesting to notice that the system, after the corrections and due to the presence of the obstacle, returns to the initial maneuver.

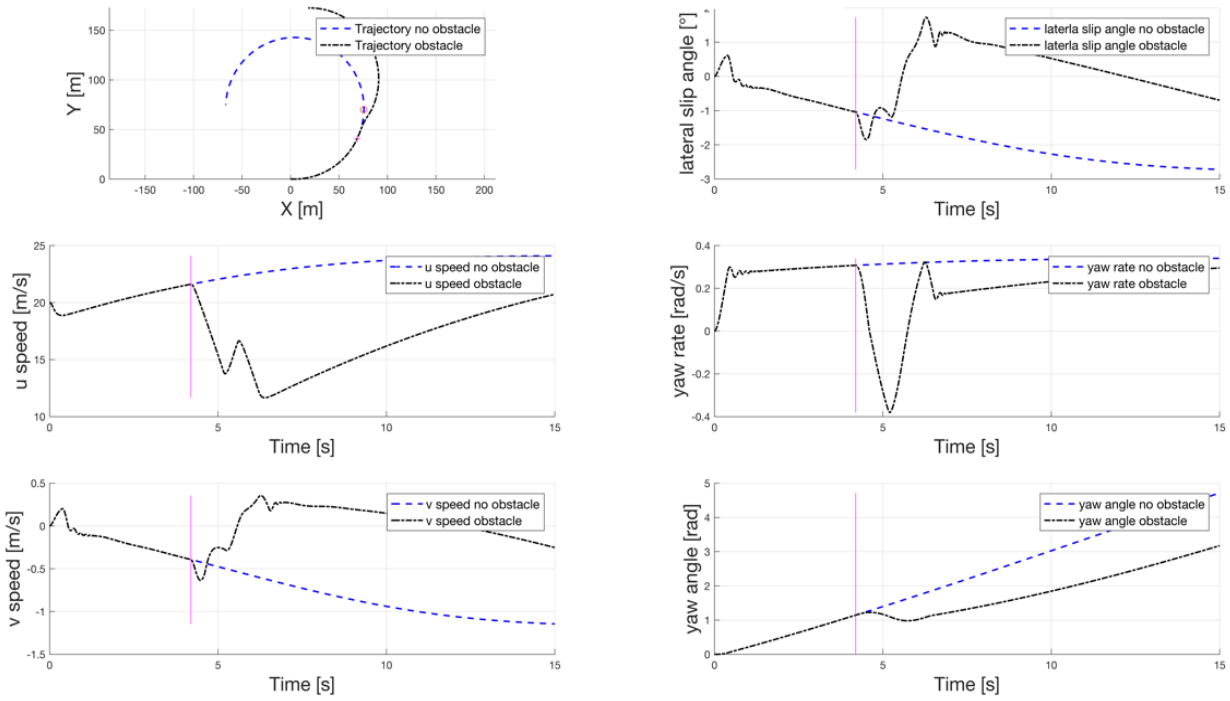

Figure 24: Trajectory comparison

It is interesting to notice in figure 25 the behavior of the control input represented by steering, rear torque and front torque when the vehicle reaches the obstacle, in fact it is noticeable that after a first braking phase the vehicle steers to avoid the collision, then it returns to accelerate and while proceeding to the original turning radius, this particular behavior is due to the functions (112) that request to maximum speed of the vehicle while following a specific trajectory and to avoid the obstacle by varying the orientation of the speed and not only its modulus showing a great performance in terms of vehicle maneuverability.

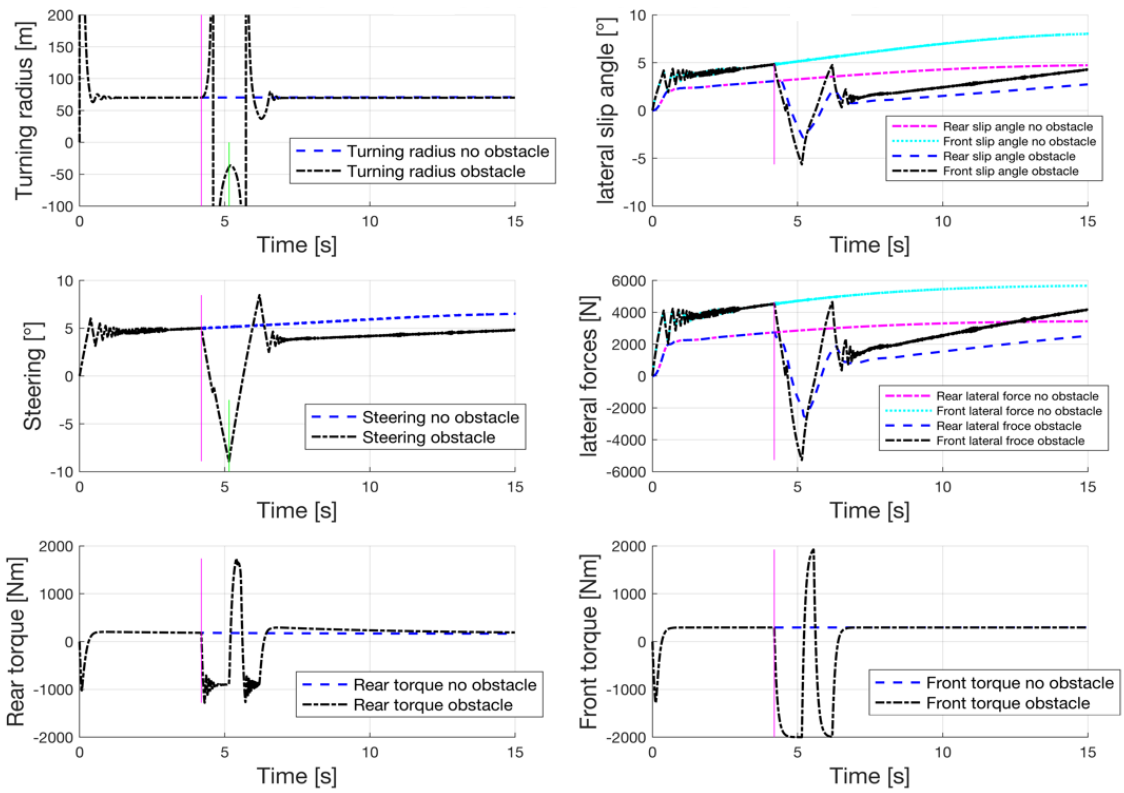

Figure 25: Control and Pacejka's forces comparison

the first strategy is compared with the LQR control logic. The equations of motion in this last case are rewritten using as a state variable the turning radius r:

$$\begin{bmatrix} \dot{X} \\ \dot{Y} \\ \dot{\psi} \\ \dot{u} \\ \dot{\beta} \\ \dot{r} \\ \dot{\omega}_r \\ \dot{\omega}_f \end{bmatrix} = \boldsymbol{M}^{-1} \begin{bmatrix} \cos(\psi)\, u - \sin(\psi)\beta u \\ \sin(\psi)\, u + \cos(\psi)\beta u \\ u/r \\ F_1 \\ -\frac{\beta}{u} F_1 + \frac{1}{u} F_2 \\ \frac{r}{u} F_1 - \frac{r^2}{u} F_3 \\ C_r - F_{long_r} R_w - F_{rolling_r} R_w \\ C_f - F_{long_f} R_w - F_{rolling_f} R_w \end{bmatrix} \tag{116}$$

$$F_1 = F_{long_f} \cos(\delta) - F_{lat_f} \sin(\delta) + F_{long_r} - F_{aero} + \frac{m\beta u^2}{r}$$

$$F_2 = \left(F_{long_f} \sin(\delta) + F_{lat_f} \cos(\delta) + F_{lat_r} - \frac{m u^2}{r} \right)$$

$$F_3 = \left(F_{long_f} \sin(\delta)\, l_f + F_{lat_f} \cos(\delta)\, l_f - F_{lat_r} l_r \right)$$

This makes possible, for the LQR, to reduce the cost function state dependence to a simple quadratic form in terms of the turning radius. However, this formulation is used for both the LQR and the FLOP

method to perform the comparison. The objective function is completed, for both cases, with a velocity dependent quadratic term, trying to force the vehicle to proceed at high speed.
Fig. 26 shows the example of simulation results for two different tracked values of the radius: 40m and 140m.

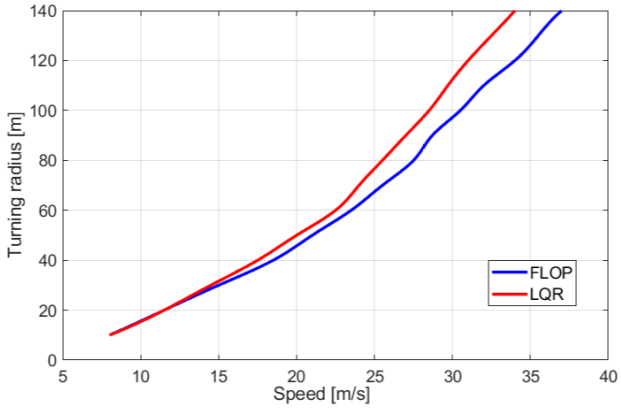

Figure 26: Flop Vs LQR comparison

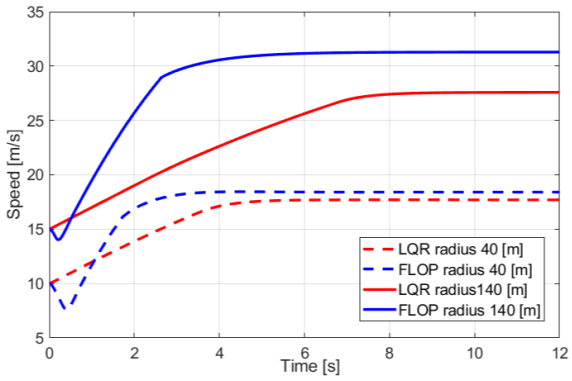

Figure 27: FLOP Vs LQR comparison

In Fig. 27, the evolution of the vehicle speed for each turning radius is shown. The FLOP approach shows better results, characterized by a higher asymptotic speed with a shorter transient. For the larger radius, the advantage of the FLOP method is even more evident.

3.6 Obstacle Avoidance

In this section, the collision avoidance performances of the FLOP control are investigated. A first example considers the collision avoidance when the car is travelling along a given circular trajectory, where an obstacle appears, as shown in Fig. 28-29.

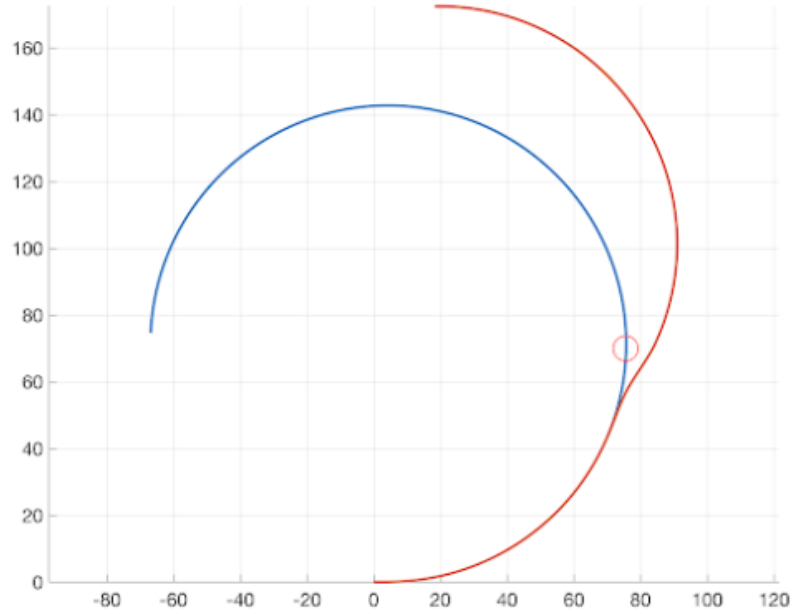

Figure 28: Obstacle avoidance

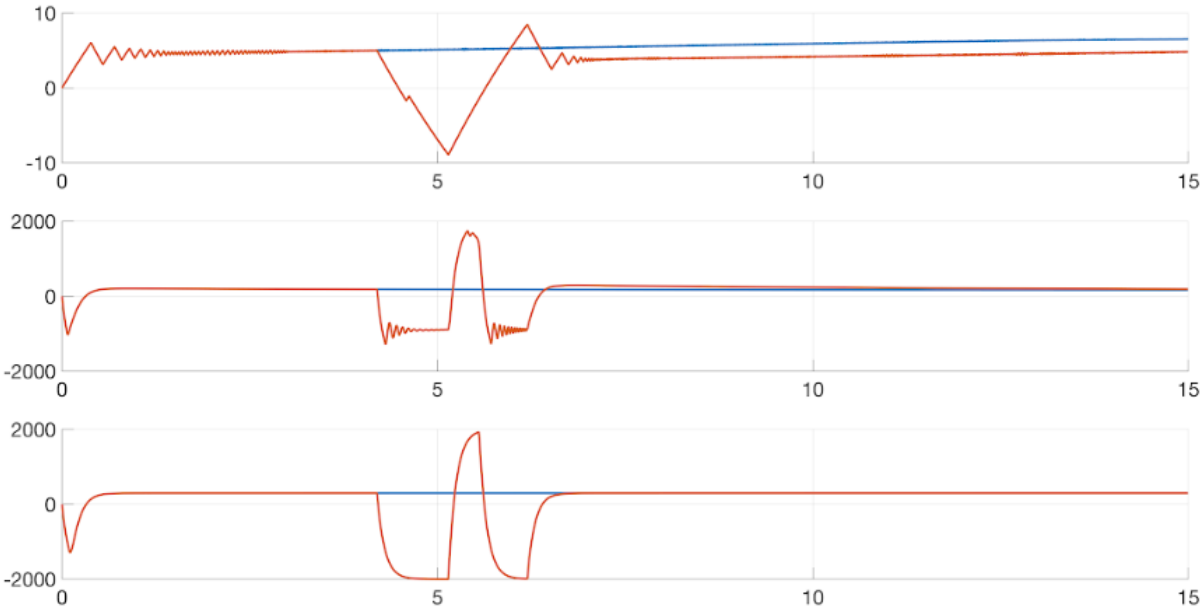

Figure 29: FLOP steering and torques

In Fig. 28-29 the FLOP controlled vehicle is first tested on following a curved trajectory without obstacle, then an obstacle is placed on the trajectory. The FLOP guided vehicle succeeds in performing the braking phase, the steering phase and in following back to the previous condition, i.e. following a designed turning radius.

The robustness of FLOP control on collision avoidance is also tested in other three different scenarios:

- Frontal collision avoidance.
- Rear-end collision avoidance.
- Cross collision avoidance.

These three scenarios are used on one hand to prove the robustness of FLOP approach in different environments simulation. On the other hand, one of the main fundamental aspect of the autonomous vehicle project is to assure a high level of safety for people inside the AVs. Therefore, these three

scenarios are chosen to prove FLOP guided vehicle is a safe system. In these simulations, sensors emulation is added in the dynamical vehicle model. Sensors are divided in two main categories:

- State estimation
- Obstacle detection

For the state estimation, list of emulated sensors includes GPS, Inertial Measurement Unit (IMU) and wheel encoder. Regarding the obstacle detection, emulated sensors includes radar and ultra-sound, for long-range and short-range detection, respectively. Sensors emulation is performed in real-time simulation in MATLAB and Simulink environment, and it provides reliable results for the real experimental phase of the autonomous vehicle project.

In the first scenario, two cars are in the same roadway, as shown in Fig. 31. The vehicle controlled by FLOP (blue) is on the correct lane. The uncontrolled vehicle (in red) is in the same carriage of the blue one, so is in the wrong carriage. FLOP, here, must perform multiple tasks:

- Obstacle detection
- Obstacle avoidance
- Carriage maintenance

Obstacle detection is performed in the simulation through the emulation of long-range and short-range obstacle detection sensors, i.e. radar and ultrasound, respectively. Once the uncontrolled vehicle is detected, obstacle avoidance is performed by using a highly nonlinear local penalty function, centered in the position of the uncontrolled vehicle. Each side of the carriage is mathematically expressed as a high penalty function, so that the controlled vehicle succeeds in remaining in the correct carriage. Results are shown in Fig. 30-34.

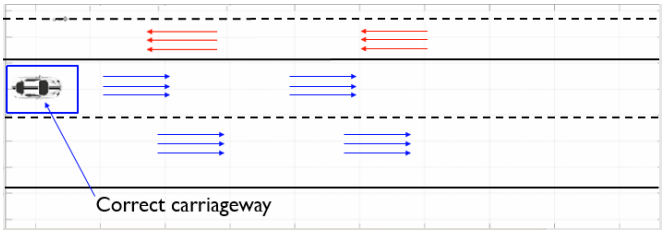

Figure 30: No obstacle detection

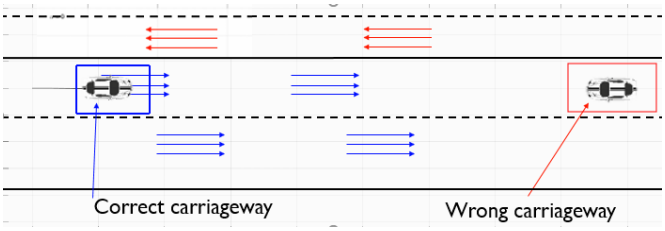

Figure 31: Obstacle detection

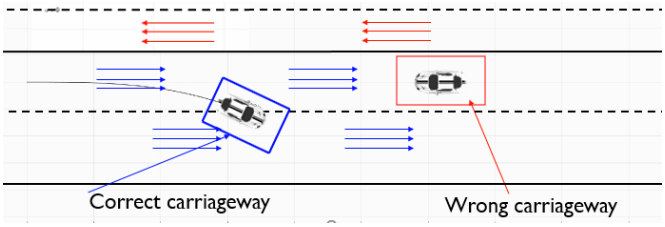

Figure 32: Obstacle avoidance

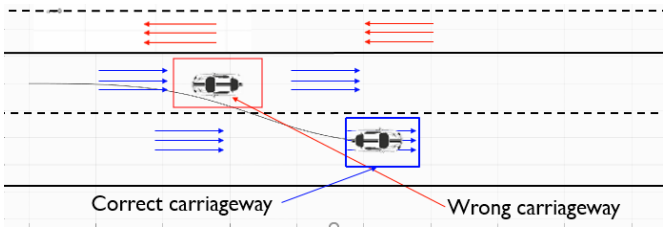

Figure 33: Carriage maintenance

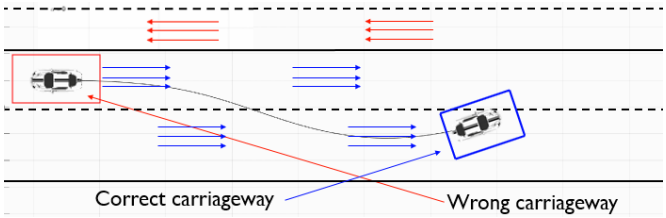

Figure 34: Returning in the previous carriage

As shown, the FLOP controlled vehicle succeeds in

- detecting the uncontrolled car (Fig. 31),
- avoiding the uncontrolled car (Fig. 32),
- maintaining the correct carriage (Fig. 33),
- returning in the original carriage (Fig. 34).

In this example, some of the potentialities of autonomous vehicle controlled by FLOP are exhibited. Penalty function $g(\boldsymbol{x})$ contains both obstacle avoidance $g_{OA}(\boldsymbol{x}, \boldsymbol{x_{obs}})$ and carriage maintenance $g_{\boldsymbol{CM}}(\boldsymbol{x}, \boldsymbol{x_C})$ function, as shown in (12)

$$
\begin{aligned}
g(\boldsymbol{x}) &= g_{\boldsymbol{OA}}(\boldsymbol{x}, \boldsymbol{x_{Obs}}) + g_{\boldsymbol{CM}}(\boldsymbol{x}, \boldsymbol{x_C}) \\
g_{\boldsymbol{OA}}(\boldsymbol{x}, \boldsymbol{x_{Obs}}) &= \frac{K_{obs}}{\sqrt{2\pi}\sigma_{Obs}} \exp\left(-\frac{1}{2}\left(\frac{\boldsymbol{x} - \boldsymbol{x_{Obs}}}{\sigma_{Obs}}\right)^2\right) \\
g_{\boldsymbol{CM}}(\boldsymbol{x}, \boldsymbol{x_C}) &= -\frac{K_{CM}}{\sqrt{2\pi}\sigma_{CM}} \exp\left(-\frac{1}{2}\left(\frac{\boldsymbol{x} - \boldsymbol{x_C}}{\sigma_{CM}}\right)^2\right)
\end{aligned}
\tag{117}
$$

with

- $\boldsymbol{x}$ state of the controlled vehicle
- $\boldsymbol{x_{Obs}}$ state of the uncontrolled vehicle
- $\boldsymbol{x_C}$ position of the carriages.
- K_{obs}, σ_{obs} gaussian parameter for obstacle avoidance
- K_{CM}, σ_{CM} parameter for carriage maintenance.

As second scenario, the FLOP controlled vehicle (in blue) is tested on the avoidance of a rear-end collision caused by an uncontrolled car (in red). Both cars are in the same carriage. In the initial condition, only the controlled vehicle is visible, as shown in Fig. 35.

Figure 35: No obstacle detection

Tasks are the same of the previous case. Next figures show the result of the simulation:

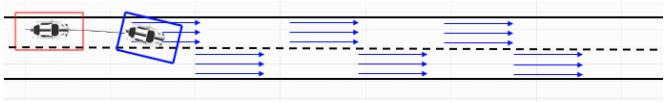

Figure 36: Obstacle detection

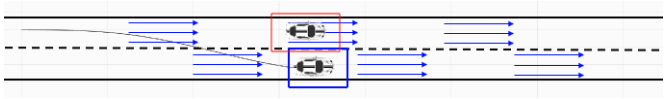

Figure 37: Obstacle avoidance

Figure 38: Carriage re-entry

As shown in Fig. 36-38, the controlled vehicle is capable to avoid also a rear-end collision, by simultaneously remaining in the assigned carriage. Penalty function used is the same of the previous example. As last scenario, FLOP approach is tested on cross collision avoidance. In this test case, situation is the one depicted in Fig. 39: the controlled by FLOP vehicle (in blue) is on the left of the figure, with green light.

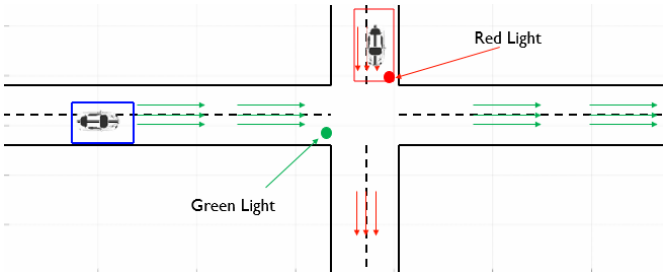

Figure 39: Cross collision scenario

The uncontrolled vehicle comes from the top of the figure, with red light. Driver of the uncontrolled vehicle do not brake the car and cross the intersection. Tasks for the controlled vehicle are the same of previous cases:

- Obstacle detection
- Obstacle avoidance
- Carriage maintenance

Following figures shown the simulation performed in MATLAB and Simulink environment:

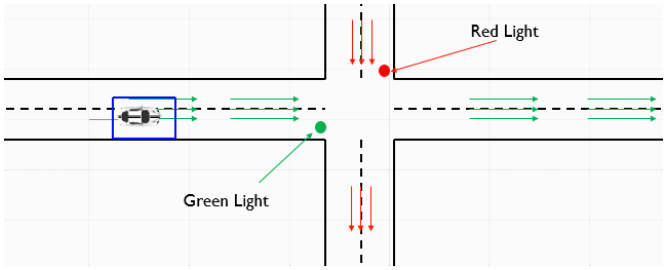

Figure 40: No obstacle detected

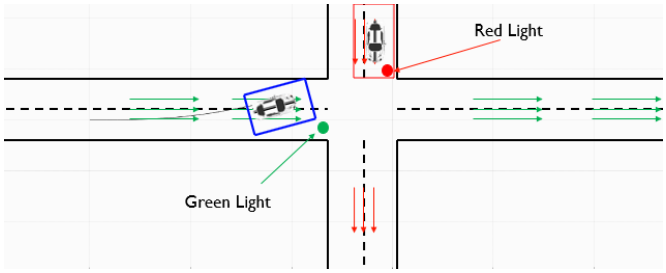

Figure 41: Obstacle detected

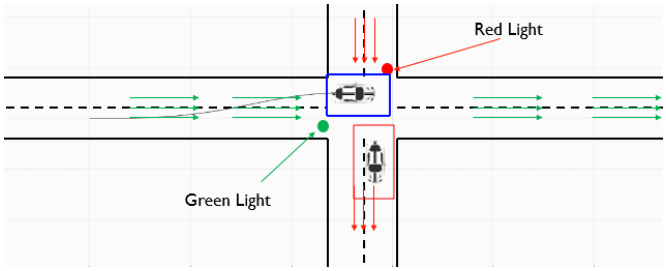

Figure 42: Obstacle avoidance

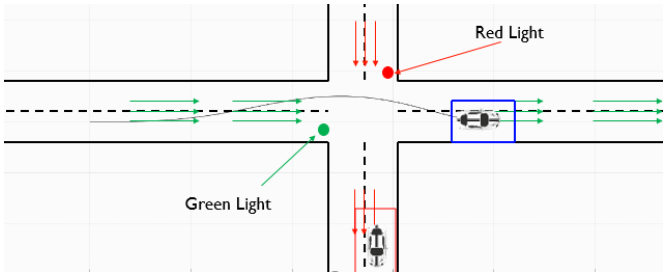

Figure 43: Carriage re-entry.

A third scenario is represented in Fig. 40-43. Even in this more complex case, the FLOP controlled vehicle succeeds in avoiding the collision with the uncontrolled one. These three scenarios prove the ability of the FLOP-guided vehicle to react to avoid the collision.

3.7 Trajectory optimization

The first step of the technique is the identification of the set of optimal maneuvers for the vehicle, that will guide it properly within its motion. In order to define these maneuvers specific penalty functions $g(\boldsymbol{x})$ are introduced, these can represent any kind of possible nonlinear and continuous function.
In order to perform the fastest lap time for the considered vehicle a set made of 5 main maneuvers is selected, steering maneuver, corner entry, straight alignment, max acceleration, max braking. The main ability for an autonomous car, is the steering maneuver, this will give to the vehicle the required stability to go around corners safely.
This function, named $g_r(\boldsymbol{x})$ is a quadratic form of the $t(\boldsymbol{x})$; $t_{reference}$ these represent the actual turning radius and its reference value. $t(\boldsymbol{x})$ is function of the vehicle's state $\boldsymbol{x}$, and can be easily evaluated in term of the absolute speed V of the vehicle and the yaw rate ω as follows:

$$t(\boldsymbol{x}) = \frac{V}{\omega} \tag{118}$$

The function makes the car perform the desired turning radius and in order to reach the optimal performance in terms of time, i.e. minimum time, the vehicle has to perform the corner, at the maximum speed allowed for the considered vehicle, and is determined through several simulations for different corners. The limit of the vehicle's state envelope is represented in Fig. 44, where maximum speed through the corner versus different turning radius, values are depicted:

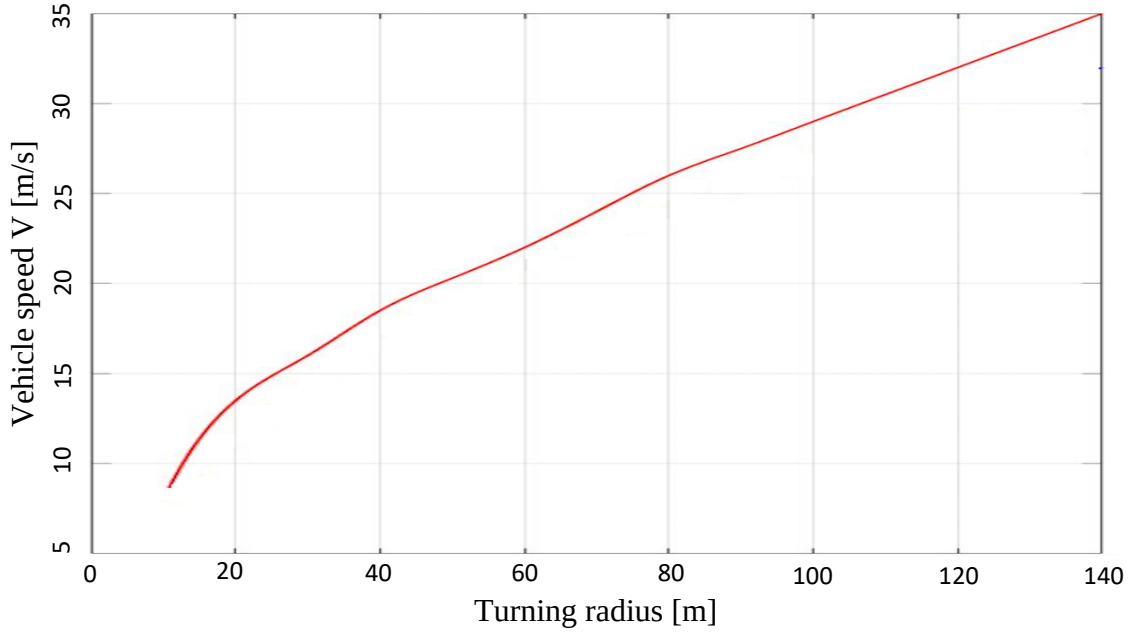

Figure 44: Vehicle maximum cornering speed

The steering maneuver implies the corner entry maneuver, in fact in order to obtain a stable trajectory around the corner, the vehicle has to reach the correct speed and attitude, even when it approaches the corner with uneven conditions for these. Hence a function that optimizes the vehicle's state during the corner entry phase is needed, this function $g_{cornerEntry}(\boldsymbol{x})$ is written in terms of the vehicle state $\boldsymbol{x}$, and guide the vehicle to reach the optimal state $\boldsymbol{x}_{optimalEntry}$ in terms of speed and attitude. These optimal states are determined, for the specific vehicle here considered, during the optimization process repeated for a wide set of corners. The effectiveness of the function is shown in Fig. 45, starting from different speeds, the vehicle reaches the optimal cornering speed and turning radius, for the considered turn.

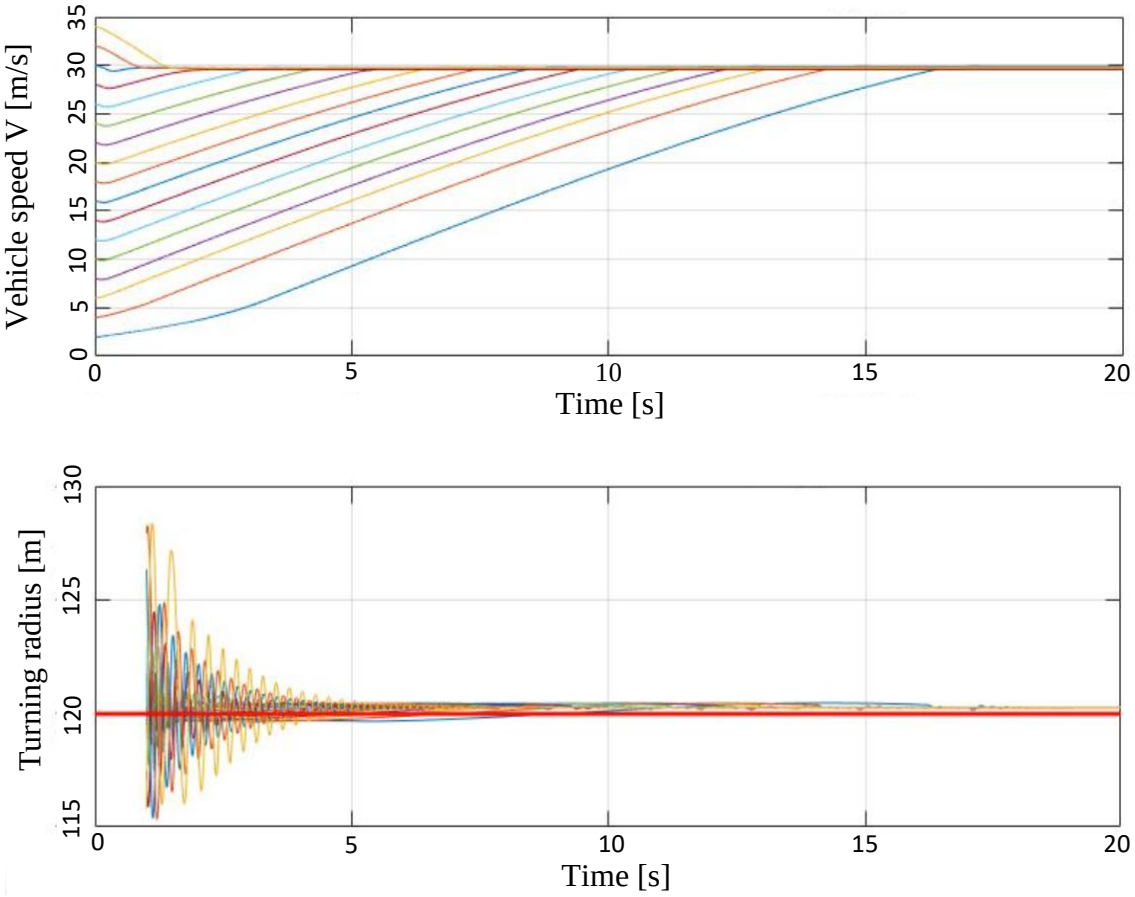

Figure 45: Vehicle maximum cornering speed from different initial conditions

Once the vehicle ends the cornering maneuver, a function that will make it come back to the straight line is needed, hence a straight alignment maneuver is defined. This function $g_{allignment}(\boldsymbol{x})$ reduces to zero vehicle's residual lateral and yaw speeds i.e. v and ω. This function helps the vehicle to maintain a straight motion with a sideslip angle β equal to zero and a speed that is parallel to the boundaries of the track.

The other two functions max acceleration and max braking, act on vehicle's speed modulus. The max acceleration function $g_{acceleration}(\boldsymbol{x})$ acts on wheel's torques to provide the maximum traction, hence maximum forward acceleration to the vehicle taking into the account the actual state. During the braking phases is still necessary to maximize the tires grip, hence an optimal maneuver for braking $g_{braking}(\boldsymbol{x})$ is introduced. These two functions maximize the modulus of the forward acceleration, this is written considering zero value for the steering control δ. The acceleration formula (119) can be written, substituting the expressions of the normal forces acting on rear and front wheels. This provides a formula that depends on actual rear and front longitudinal grip coefficients $\mu_r(\boldsymbol{x}), \mu_f(\boldsymbol{x})$, obtained by Pacejka's model, on the aerodynamic resistance and on the torques C_r, C_f:

$$\dot{u} = \frac{\mu_f(\boldsymbol{x})}{p(\boldsymbol{x})} g l_r + \frac{\mu_r(\boldsymbol{x})}{p(\boldsymbol{x})} g l_f + \frac{F_{aero}(\boldsymbol{x})}{p(x)} \frac{h_g}{m} \left(\mu_r(\boldsymbol{x}) - \mu_f(\boldsymbol{x})\right) + \frac{C_r + C_f}{p(x)m} \left(\mu_r(\boldsymbol{x}) - \mu_f(\boldsymbol{x})\right) \quad (118)$$

$$with \quad p(x) = L + \mu_f(x) h_g - \mu_r(x) h_g$$

This permits to obtain the maximum acceleration of the vehicle, considering the Pacejka's model introduced. To improve the system's performance, these coefficients can be measured through experimental setup as shown in [38-40].
Once the set of optimal maneuvers is ready the technique can be implied to identify the optimal trajectory. This procedure starts considering the specific part of the track, i.e. corner or complex arrangement of corners, this defines the road's boundaries that has to be respected by the vehicle while moving within that specific part.
The optimization phase, performed through parameter optimization tools, defines the proper arrangement of the optimal maneuvers to make the vehicle go around the considered track part as fast as possible, providing the minimum time. The optimization identifies the best time instants, to imply each of the optimal maneuvers i.e. it defines the start and end instants for every control and the specific sequence of each one.
An example of this procedure is depicted in Fig. 46, where the technique is implied for a 180° turn, with a radius of 100 meters, the corner is filleted by two straights long 200 meters, that guide the car inside and out of the corner.
The algorithm has identified the optimal maneuvers sequence, that are divided in Fig. 4 into the main phases of the vehicle motion around the corner i.e. braking phase, cornering phase, and accelerating phase.
The optimization uses multiple combinations of the optimal maneuvers. The process considers acceptable only those combinations that make the vehicle perform trajectories fully contained into the trackwidth.
The aim is a vehicle moving as fast as possible. Then, the high speed and a wrong combination of maneuvers might lead the vehicle out of track, i.e. assuming the positions represented by red crosses in Fig. 46. Each point of these trajectories is checked during the process and eventually the combination of maneuvers is discarded. Instead, among the acceptable trajectories, the algorithm chooses the one that provides the best performance in terms of time. Since the technique implied takes into the account the vehicle dynamics, the trajectory finally identified is surely performable by the considered vehicle.

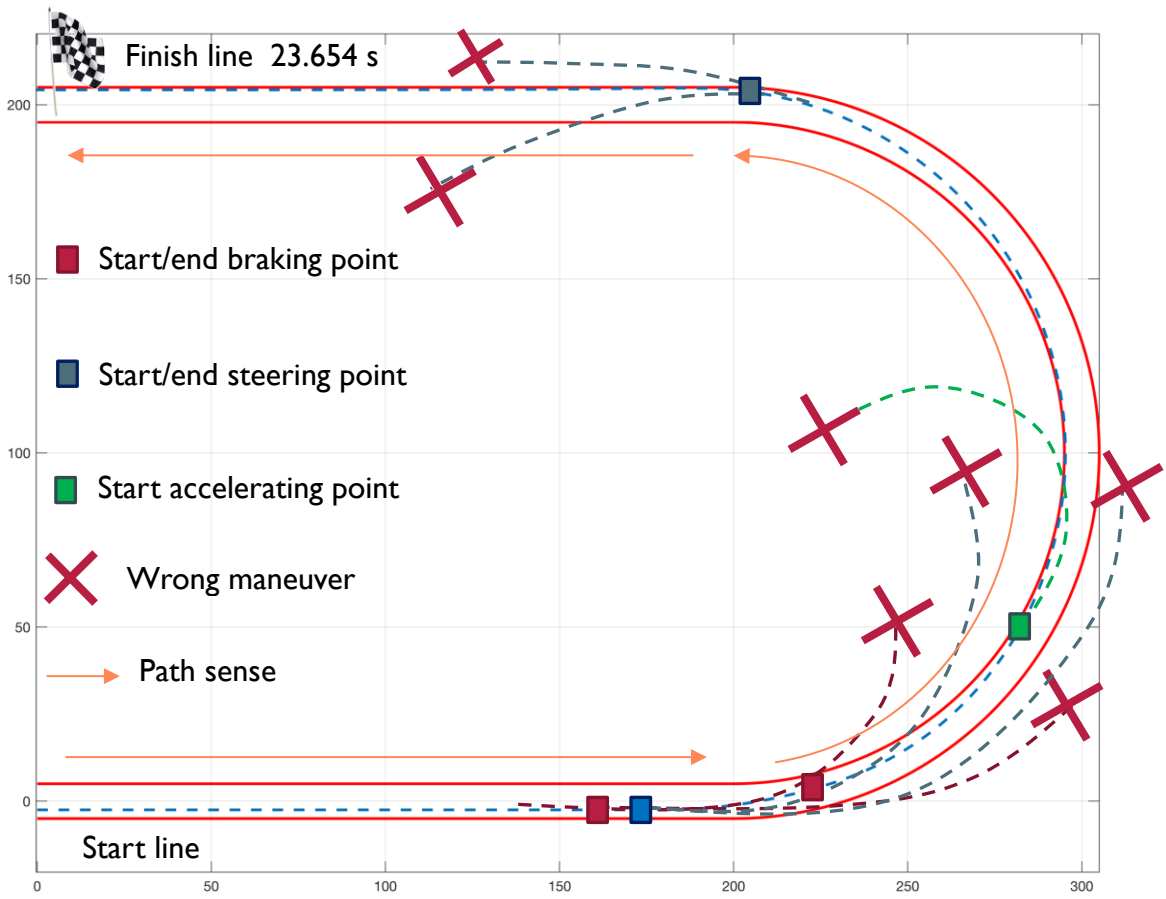

Figure 46: Optimal trajectory technique

In Fig. 46 and even in Fig. 47 is evident how the phases overlap one another in order to reach the best time performance, in particular braking phase overlaps corner entry phase till the very first beginning of the cornering phase, as much as, once the vehicle reaches the correct attitude to perform the required turning radius, the solution provided by the technique makes the acceleration phase overlap the turning maneuver, in order to provide the fastest time for the entire simulation.

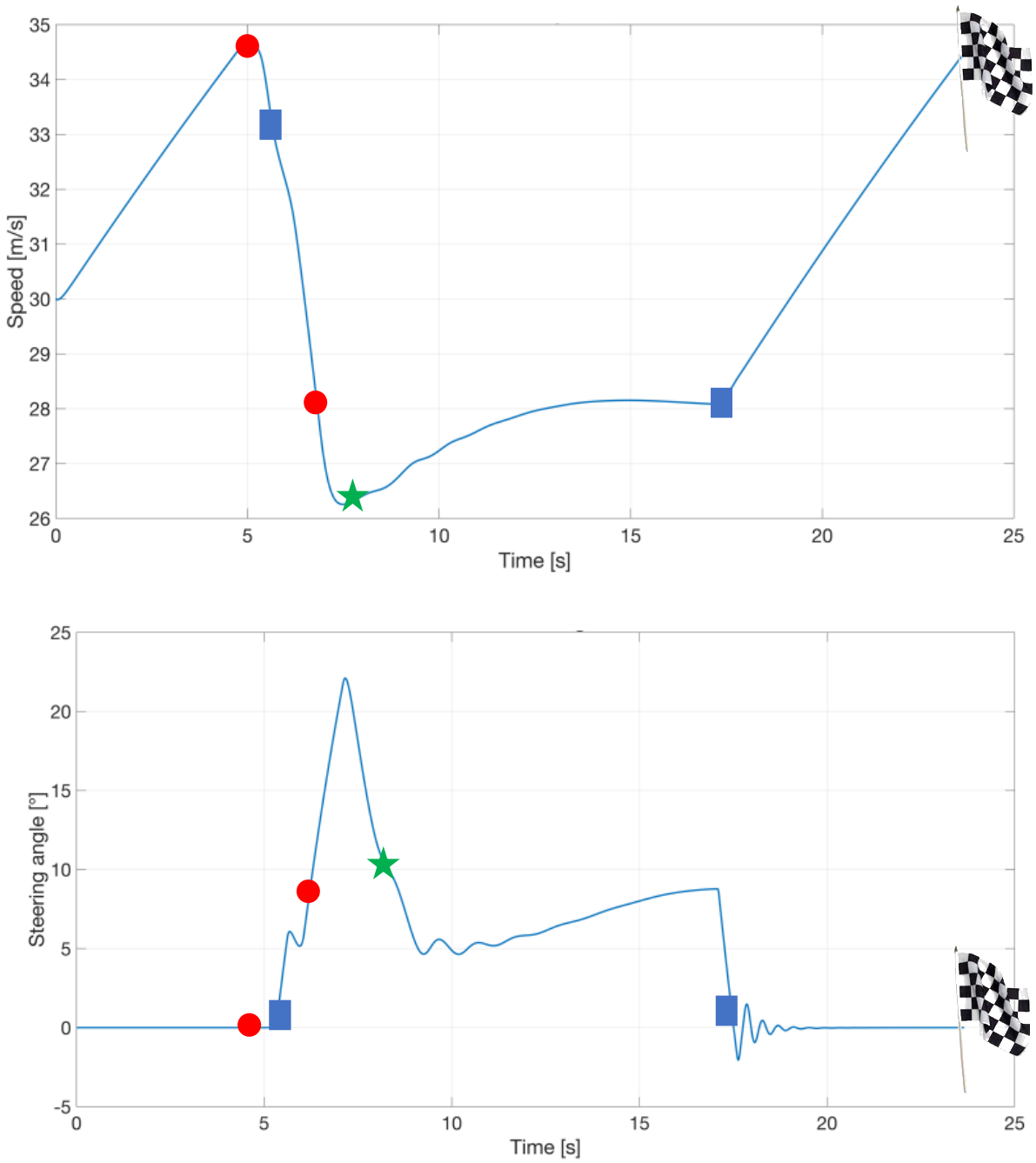

Figure 47: Vehicle speed and steering control

Fig. 47 represents the time evolution of both vehicle's speed and steering angle, during the entire simulation.
The red circles represent the starting and ending instants of the braking phase, while the vehicle speed is decreasing the turning maneuver starts, as indicated by the blue rectangle, it is interesting to notice the slight slope's reduction of the vehicle speed in the same instant, this represents the correlation between the two slip coefficients of the tires (9), in fact when the steering value raises, the tire's grip available for braking is reduced, since part of it absorbed by the lateral forces that appear when a steering maneuver is performed.
The same behavior is observed when the braking phase ends, in fact when the brakes stop their action, the required longitudinal grip decreases, hence more lateral grip is available. Since the control

technique used to generate the optimal path is aware of the vehicle's dynamic that contains a Pacejka's model, the steering angle can now be raised to the required value for performing the correct turning radius.
Once the vehicle reaches the correct state to perform the corner, the control starts the acceleration phase represented by the green star, this demands longitudinal grip, but given the feedback formulation of the FLOP technique, it takes into the account the reduced grip available due the cornering phase that is still present. This pushes the vehicle to the max accelerations reachable with the considered grip model. Given the speed increase, the steering angle required to continue to perform the desired turning radius is greater, in fact a slightly increase of the steering angle is noticeable till its end point, marked by the second blue rectangle, where the maneuver ends, leaving all the grip at disposal for the vehicle acceleration, that is strongly evident in the last part of the speed profile in Fig. 47.
The technique used is now applied in simulations in a racetrack. This part of the investigation wants to demonstrate the possibility of driving around a circuit, performing for multiple laps, safely and reliably. For this purpose, the Monza circuit is considered Fig. 48

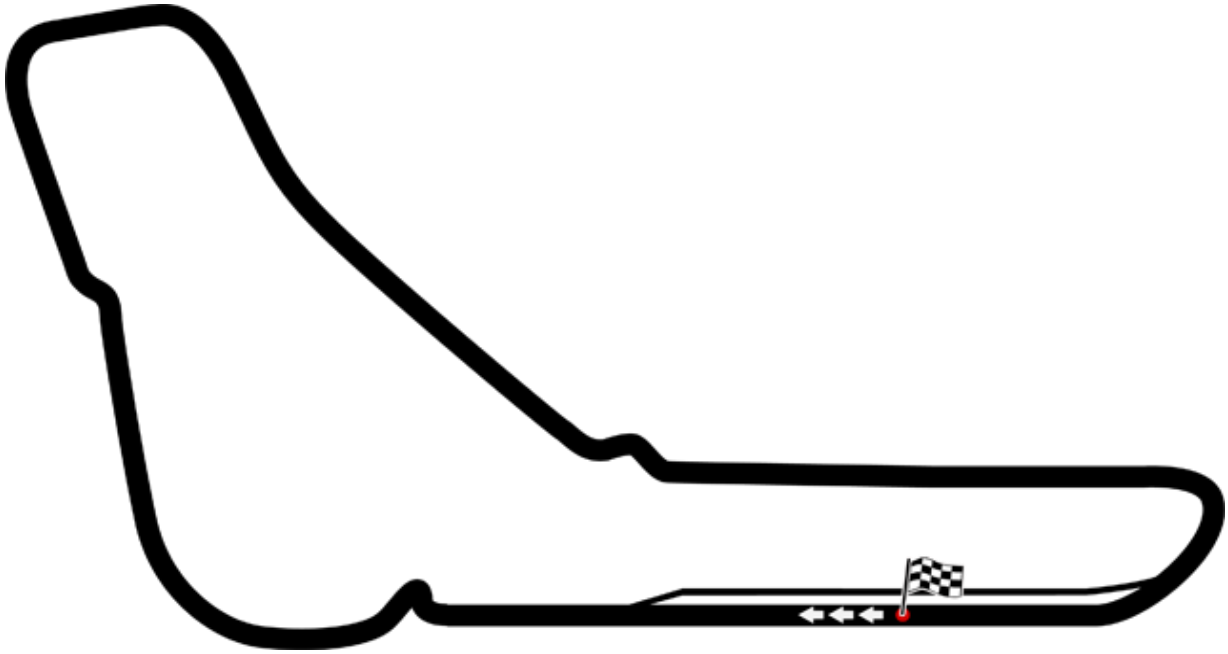

Figure 48: Monza racetrack

The optimization process, performed for each corner of the track, produced optimal trajectory that has to be performed by the considered vehicle, in order to reach the best performance around the track, Fig. 49 shows example trajectories.

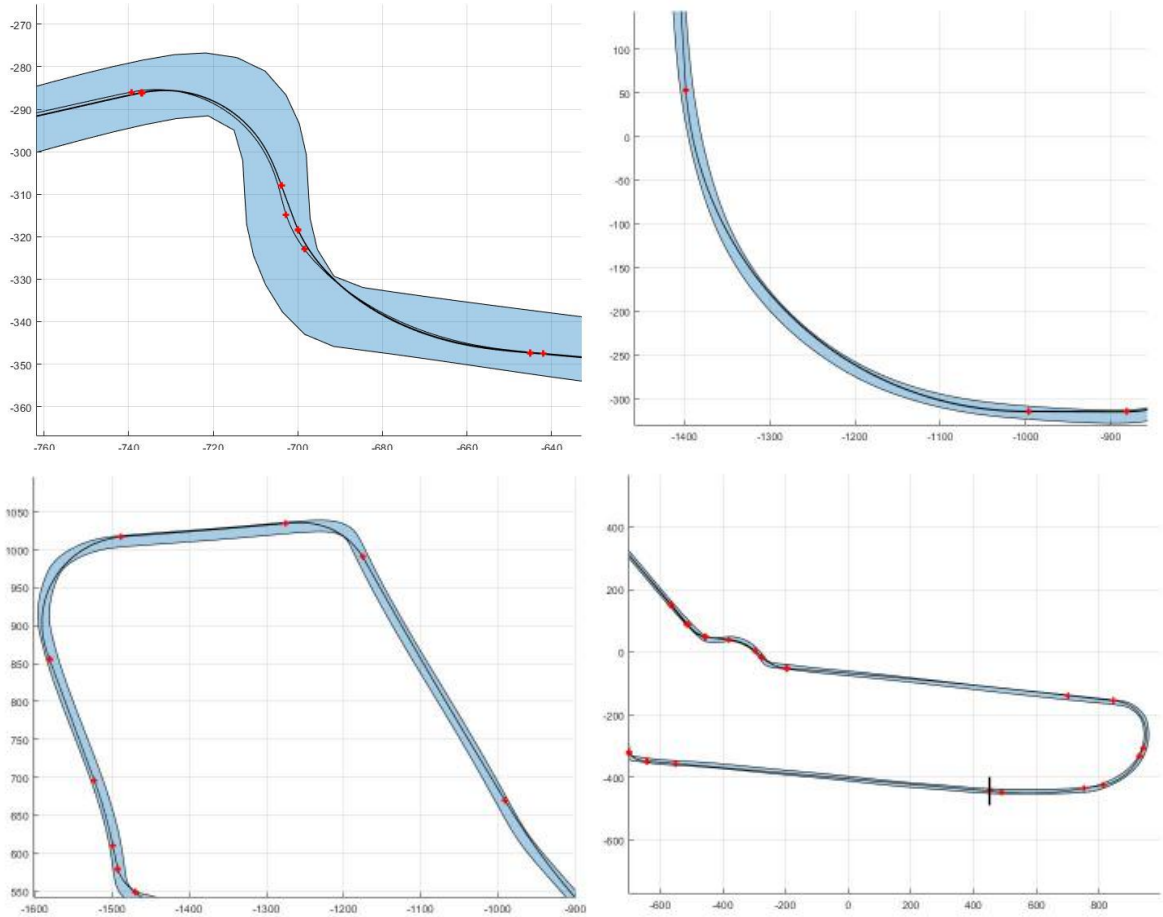

Figure 49: Monza trajectories

In order to make the vehicle perform multiple laps around the track, checkpoints are introduced at corners entry and exit points, in fact the defined control, when implied to perform various laps, provides a feedforward solution, since the optimal trajectory found is defined in terms of sequence of optimal maneuvers that has to be implied, this weakness does not guarantee a reliable sequence of laps. To overcome this, checkpoints are introduced at entry and exit of each corner, so that the vehicle is pushed to pass in specific track points. These checkpoints are represented by another $g_{checkpoints}(\boldsymbol{x})$ function that takes into the account the actual vehicle's speed direction and tries to orientate it towards the next checkpoint.
Since this in general cannot guarantee the complete reliability of the controlled system, especially in presence of disturbances, different checkpoints for each corner are defined, these differs from the others because they are obtained through other optimization process, that provided alternative trajectories, that are sub-optimal but augment the robustness of the entire system. hence even if the vehicle is not moving on the optimal trajectory due to a small disturbance, the system is able to continue the maneuver through the considered corner, safely.
Since variations in the performed trajectories can still be present, a potential function $g_{boundaries}(\boldsymbol{x})$ that avoid crashes of the vehicle with the limits of the track. This guarantees the vehicle moving safely around the track for multiple laps, without going off the track.
30 laps were performed around the chosen track, the lap times are illustrated in Tab. 4. The lap times are all similar, this underline the robustness and repeatability of the results obtained with the described

technique. The red highlighted lap time represents the worst performance, while the green one represents the best lap time obtained by the controlled system, among the 30 laps.

Lap	Time	Lap	Time
1	3.09.086	16	3.01.611
2	3.01.685	17	3.01.621
3	3.01.615	18	3.01.620
4	3.01.641	19	3.01.660
5	3.01.606	20	3.01.604
6	3.01.647	21	3.01.568
7	3.01.632	22	3.01.665
8	3.01.692	23	3.01.658
9	3.01.597	24	3.01.588
10	3.01.576	25	3.01.633
11	3.01.657	26	3.01.624
12	3.01.627	27	3.01.575
13	3.01.634	28	3.01.637
14	3.01.580	29	3.01.599
15	3.01.599	30	3.01.682

Table 4: Monza Lap times

The laps performed, given a track length of 5789 m provide a mean speed around the track of about 115 km/h, that represents a good performance considering the small production series car used as dynamic system. The significant difference in time, for the first lap is due to an initial condition, for the vehicle forward speed, reduced with respect to the reference value set by the optimization process. This new method to identify the optimal trajectory relies on the feedback control method based on the classical variational approach, named Feedback Local Optimality Principle (FLOP). FLOP technique was applied on the control of an Autonomous Vehicle that represents an ongoing project of the Mechatronic and Vehicle Dynamic Lab of Sapienza, based on production series city car, modelled through a bike-model. FLOP control represents a new approach for optimal feedback control of a vehicle, moreover it provides a new solution for trajectory optimization. This represent a reliable and robust solution since the resulting trajectory is designed taking into the account the vehicle dynamics, instead of the kinematic constraints generally introduced. It must be noticed that the performance achieved depend on the tuning process, that represents a crucial step to improve the optimality of the solution. Instead, the control flexibility, provide the chance to apply it to challenging dynamic systems, avoiding the linearization required by LQR and SDRE techniques. Further development will be devoted to the investigation of the sensitivity of the controlled system to uncertainties on system parameters, such as mass and its distribution, tire coefficients. Moreover, the applied technique will be compared with MPC based approaches to verify in deep details, the performance and the robustness compared, to those provided by these techniques.

Chapter 4

Secure Platform, Autonomous marine rescue vehicle, research project

4.1 "Secure Platform" Joint Research project Introduction

Autonomous vehicles represent the new frontier in rescue applications, the capabilities in terms of effectiveness, reliability and efficiency without the direct involvement of human make them the best choice in complex and critical situations [30,59]. These performances are strictly related to the algorithms that provide their autonomous behavior, even the most advanced platforms are less effective and secure if not driven by the best control algorithms [1-29]. This section is addressed to the analysis of an autonomous marine vehicle of a joint Industrial Research Project promoted by Fincantieri (Leading company in building cruise ships) and developed by La Sapienza, CNR (National Research Council) INM, CNR ISSIA and CNR IREA. This drone is meant for rescue purpose, here the application of the FLOP algorithm for the autonomous navigation [53] is discussed and some results are presented, the data collected during the experimental activity cannot be presented in this work, because of the restrictions due to the agreement with Fincantieri of non-disclosure.
The marine surface craft here presented Fig. 50 is a double hull catamaran vessel, its overall length is 4 meters with a width of 2.7 meters, these dimensions enhance the hiding capabilities of the vehicle even under region scanned by satellites, this augment the probability of success of any mission. The catamaran design provides more stability to the vehicle for better maneuvering, that is even enhanced by the propulsion system choice, in fact this vessel uses two jet drive pump with steering nozzle and thrust reversers, the double propulsors configuration guarantee a higher yaw rate during navigation hence enhanced dynamic performance, this coupled with the used of the advanced FLOP control algorithm gives to the vehicle the necessary agility to operate in complex environment or during avoidance maneuvers as will be shown in the following sections.

Figure 50: Secure platform prototype

The vehicle standard mission is structured as follows:

- Vehicle in stand-by monitoring all the on-board systems, to guarantee the full efficiency in any moment.
- Receives the alarm
- Vehicle, launch, ditch into the water, systems check.
- Receives GPS coordinates of the man within a range of 5 miles from its actual position
- Autonomous navigation in any environment and in any complex situation thanks to its advanced control algorithm.
- Perform the rescue action.
- Return to the main ship, or navigation to any other recovery point.

The following table summarize the principal characteristics of the vehicle:

	Vehicle
type	catamaran
mass	800 [kg]
L_{wl}	4 [m]
$width$	2.7 [m]
payload	150 [kg]
V_{max}	10 [m/s]
propulsion	electric

Table 5: Vehicle characteristics

4.2 Surface marine craft vehicle dynamics

The equations of motion of the vehicle are represented by a six-DOF differential equation system, written in the body fixed reference system in terms of the surge speed u, the sway speed v, the heave speed w and in terms of three rotational speed represented by the roll motion p, the pitch motion q and the yaw motion v, these lead to the following set of equation:

$$
\begin{aligned}
&m\left[\dot{u} - vr + wq - x_g(q^2 + r^2) + y_g(pq - \dot{r}) + z_g(pr + \dot{q})\right] = F_x \\
&m\left[\dot{v} - wp + ur - y_g(p^2 + r^2) + z_g(qr - \dot{p}) + x_g(qp + \dot{r})\right] = F_y \\
&m\left[\dot{w} - uq + vp - z_g(p^2 + q^2) + x_g(rp - \dot{q}) + y_g(rq + \dot{p})\right] = F_z \\
&I_x\dot{p} + \left(I_z - I_y\right)qr - (\dot{r} + pq)I_{xz} + (r^2 - q^2)I_{yz} + (pr - \dot{q})I_{xy} \\
&\qquad + m\left[y_g(\dot{w} - uq + vp) - z_g(\dot{v} - wp + ur)\right] = M_x \\
&I_y\dot{q} + (I_x - I_z)rp - (\dot{p} + qr)I_{xy} + (p^2 - r^2)I_{zx} + (qp - \dot{r})I_{yz} \\
&\qquad + m\left[z_g(\dot{u} - vr + wq) - x_g(\dot{w} - uq + vp)\right] = M_y \\
&I_z\dot{r} + \left(I_y - I_x\right)pq - (\dot{q} + rp)I_{yz} + (q^2 - p^2)I_{xy} + (rq - \dot{p})I_{zx} \\
&\qquad + m\left[x_g(\dot{v} - wp + ur) - y_g(\dot{u} - vr + wq)\right] = M_z
\end{aligned}
\tag{118}
$$

That is written in the general form that consider the origin of the reference settled in the general point of the vehicle $[x_g; y_g; z_g]$, the terms $[F_x; F_y; F_z; M_x; M_y; M_z]$ represents the external forces, such as resistance and propulsion forces that act on the vehicle during its navigation, while the inertia of the vehicle is described by $[m; I_x; I_y; I_z; I_{xy}; I_{xz}; I_{yz}]$.
The formulation of the control will be addressed by a specific dynamic model usually defined as three-DOF control model, this reduction of degrees of freedom relies on two main aspects, the motion of surface craft vehicle is represented by a planar motion, hence the DOF that has to be controlled are represented by its surge sway and yaw motion, moreover the characteristic times of these motions are slow than it is right to admit that the frequency content of the external forces acting on the vehicle does not affect these DOF.
The dynamic system of the vehicle used to evaluate the feedback control law is then rewritten in terms of the absolute coordinate fig. 51 of the system that are measured in the world fixed reference, the surge, sway and yaw speeds and in terms of the engines speed $\boldsymbol{x} = [X; Y; Azimuth; u; v; r; \omega_1; \omega_2]^T$:

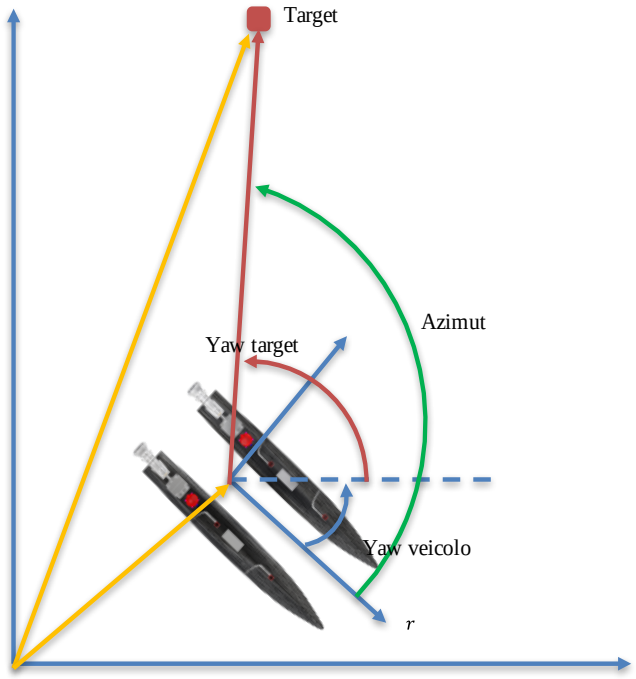

Figure 51: reference system

These lead to the following set of non-linear differential equation, that can be written in its compact formulation represented by:

$$\boldsymbol{M}\dot{\boldsymbol{x}} = \boldsymbol{\phi_{tot}}(\boldsymbol{x}) + \boldsymbol{h_{tot}}(\boldsymbol{x}, \boldsymbol{u}) \tag{119}$$

Where $\boldsymbol{M}$ is the inertia matrix $\boldsymbol{M} = diag[1; 1; 1; m; m; I_z; I_{engine}; I_{engine}]$; the control parameters $\boldsymbol{u} = [i_1; i_2; \theta_1; \theta_2; r1; r2]$ considered are the two currents $i_1; i_2$ that drive the engines, here considered electric, the two steerable nozzle angle $\theta_1; \theta_2$ and finally the thrust reverser $r1; r2$. The terms $\boldsymbol{\phi_{tot}}(\boldsymbol{x})$ and $\boldsymbol{h_{tot}}(\boldsymbol{x}, \boldsymbol{u})$ are non-linear function of the state $\boldsymbol{x}$ and control $\boldsymbol{u}$, such that:

$$\boldsymbol{\phi_{tot}} = [\boldsymbol{R}(yaw)[u, v, \omega]^T \quad ; \quad \boldsymbol{\phi}(\boldsymbol{x})] \tag{120}$$

Where $\boldsymbol{\phi}(\boldsymbol{x})$

$$\boldsymbol{\phi}(\boldsymbol{x}) = \begin{cases} -0.5\rho A_{car} C_{car}(u+\omega b)^2 \tanh\big(20(u+\omega b)\big) - 0.5\rho A_{car} C_{car}(u-\omega b)^2 \tanh\big(20(u-\omega b)\big) - R_1 - R_2 \\ -\rho A_{lat} C_{lat} v^2 tanh(20v) \\ -\rho A_{lat} C_{lat} v^2 tanh(20v) by - -0.5\rho A_{car} C_{car}(u+\omega b)^2 \tanh\big(20(u+\omega b)\big)\, b + 0.5\rho A_{car} C_{car}(u-\omega b)^2 \tanh\big(20(u-\omega b)\big) b - C_1 - C_2 \\ -\rho V_{noz1} A_{noz}\left(\omega_1 r_{medio} - \dfrac{V_{noz1} A_{noz}}{A_{imp}} \tan(b2)\right) r_{medio} \\ -\rho V_{noz2} A_{noz}\left(\omega_1 r_{medio} - \dfrac{V_{noz1} A_{noz}}{A_{imp}} \tan(b2)\right) r_{medio} \end{cases} \tag{121}$$

With R_1, R_2 the residuary resistance forces due to the hulls of the vehicle and C_1, C_2 the torques due to the resistance of the hulls evaluated around the yaw axis Z. The $\boldsymbol{h_{tot}}(\boldsymbol{x}, \boldsymbol{u})$ contains the controls variable with non-linear dependence from them:

$$\boldsymbol{h_{tot}}(\boldsymbol{x}, \boldsymbol{u}) = [[0,0,0]^T; \boldsymbol{h}(\boldsymbol{x}, \boldsymbol{u})] \tag{122}$$

Where $\boldsymbol{h}(\boldsymbol{x}, \boldsymbol{u})$

$$\boldsymbol{h}(\boldsymbol{x}, \boldsymbol{u}) = \begin{cases} r_1 \rho V_{noz1} A_{noz}(V_{noz1} - (u+\omega b)) \cos(\theta 1) + r_2 \rho V_{noz2} A_{noz}(V_{noz2} - (u-\omega b)) \cos(\theta 2) \\ r_1 \rho V_{noz1} A_{noz}(V_{noz1} - (u+\omega b)) \sin(\theta 1) + r_2 \rho V_{noz2} A_{noz}(V_{noz2} - (u-\omega b)) \sin(\theta 2) \\ -r_2 \rho V_{noz2} A_{noz}\big(V_{noz2} - (u-\omega b)\big)(\cos(\theta 2) b + \sin(\theta 2)\, l/2) + r_1 \rho V_{noz1} A_{noz}(V_{noz1} - (u+\omega b))(\cos(\theta 1) b - \sin(\theta 1)\, l/2) \\ Volt * i1 * \dfrac{\eta_{mot}}{\omega_1} \\ Volt * i2 * \dfrac{\eta_{mot}}{\omega_2} \end{cases} \tag{123}$$

4.3 FLOP for vehicle GN&C (guidance, navigation & control)

In this section will be shown the development of the FLOP feedback control law for this autonomous stealth surface craft, a specific cost function J must be formulated in order to obtain, from the variational calculus, the relations that provide the control law.

$$\bar{J} = \int_0^T \frac{1}{2}(\boldsymbol{x}^T \boldsymbol{Q} \boldsymbol{x} + \boldsymbol{u}^T \boldsymbol{R} \boldsymbol{u}) + g(\boldsymbol{x}) + \boldsymbol{\lambda}^T\big(\dot{\boldsymbol{x}} - \boldsymbol{f}(\boldsymbol{x}, \boldsymbol{u})\big)\, dt \tag{124}$$

The first term represents the quadratic term $\boldsymbol{x}^T \boldsymbol{Q} \boldsymbol{x}$ in the state $\boldsymbol{x}$ the quadratic form in the control $\boldsymbol{u}$, the $\boldsymbol{R}$ matrix is positive definite and contains the coefficients that relates the three degrees of control, the constraint term represented by the dynamic equations of the model is introduced through the Lagrange multipliers $\boldsymbol{\lambda}$, it is interesting to notice the non-conventional, non-linear function $g(\boldsymbol{x})$ introduced here, in fact normal optimal based feedback control law can deal only with quadratic nonlinearities, in this case thanks to the FLOP formulation, it is possible to introduce any kind of non-linear C^1 function, this let the user to modify the potential function represented by the cost function, allowing it to modify even locally the shape of the function, in order to produce better performances in terms of reliability, robustness and effectiveness of the controlled vehicle. In this case the $g(\boldsymbol{x})$ function permitted to take into the account additional requirements:

$$g(\boldsymbol{x}) = g_o(\boldsymbol{x}) = Ke^{\left(-0.5\left(\frac{vehicle_{azimut} - obs_{azimut}}{sigma}\right)^2\right)} \tag{125}$$

Where the $g_o(\boldsymbol{x})$ represents a non-linear function of the state $\boldsymbol{x}$ used to avoid obstacles or forbidden zone fig. 52, expressed in terms of the vehicle azimuth and of the angular position of the obstacles.

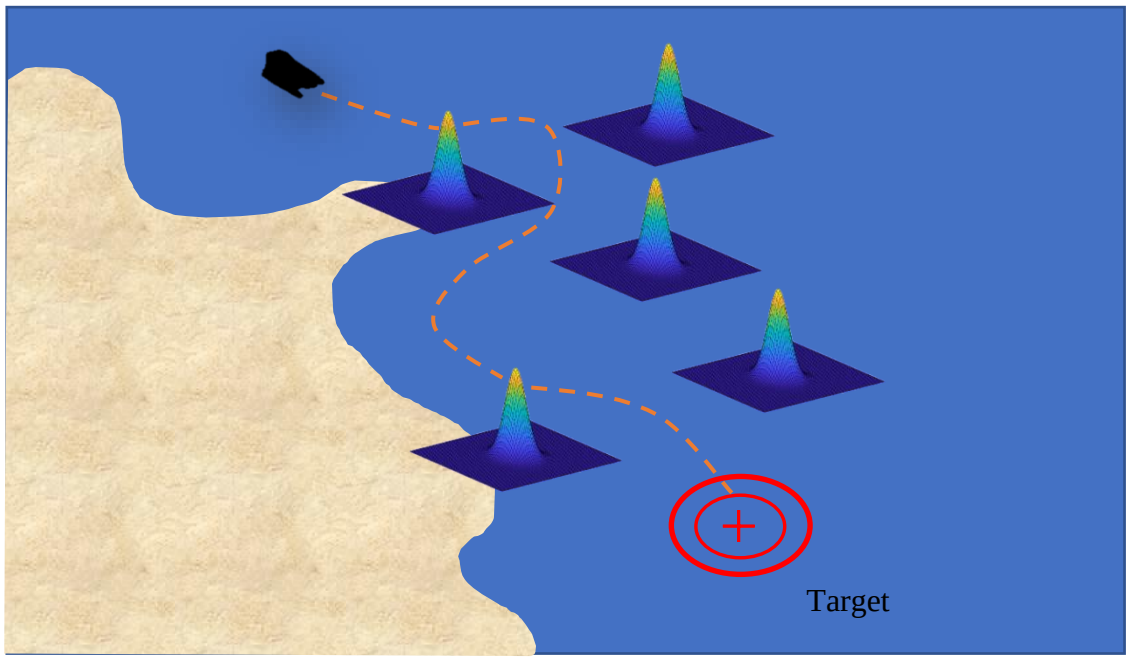

Figure 52: Obstacle avoidance

$$\begin{cases} \nabla_x g(\boldsymbol{x}) - \dot{\boldsymbol{\lambda}} - \left(\nabla_x \boldsymbol{\phi}(\boldsymbol{x})\right)^T \boldsymbol{\lambda} - \boldsymbol{A}^T \boldsymbol{\lambda} = \boldsymbol{0} \\ \boldsymbol{R}^T \boldsymbol{u} - \boldsymbol{B}^T \boldsymbol{\lambda} = \boldsymbol{0} \\ \boldsymbol{M}\dot{\boldsymbol{x}} = \boldsymbol{\phi}_{\boldsymbol{tot}}(\boldsymbol{x}) + \boldsymbol{h}_{\boldsymbol{tot}}(\boldsymbol{x}, \boldsymbol{u}) \end{cases} \tag{126}$$

The FLOP approach leads to the following non-linear formulation of the control law, since its complexity compared to those usually provided by the classical feedback control law, the algorithm will be more conscious of all the systems non-linear behaviors, local variation of the potential field, leading to a more advanced autonomous marine vehicle.

$$\boldsymbol{u}_{\boldsymbol{FLOP}} = \boldsymbol{\chi}(\boldsymbol{x}) \tag{127}$$

4.4 results

The following section presents the results of the FLOP control, applied to the vehicle, showing how it can avoid obstacles or forbidden zone and reach the target position provided by an external source. This test case represents one of the most important and challenging, in fact the capability of moving autonomously with confidence in a complex scenario enhance the probability of success in any mission.
Figure 53 illustrates the evolution of the trajectory, performed by the vehicle, in this case the vehicle must reach the target represented by the orange dot, while avoiding the ship present on the path. The vehicle starts the navigation reaching a cruise navigation speed, as shown by the fig. 54, this is very close to the highest speed achievable by the vehicle, because it was designed to provide the best efficiency within that range of speed.

When the vehicle approaches one the obstacles its forward speed decreases in favor of the lateral speed as shown in fig. 55, in fact when this increases a variation in the longitudinal speed is observed, once the first obstacle is avoided the lateral speed is reverted, the vehicle passes through the two ships, and then performs the avoidance of the second obstacles.

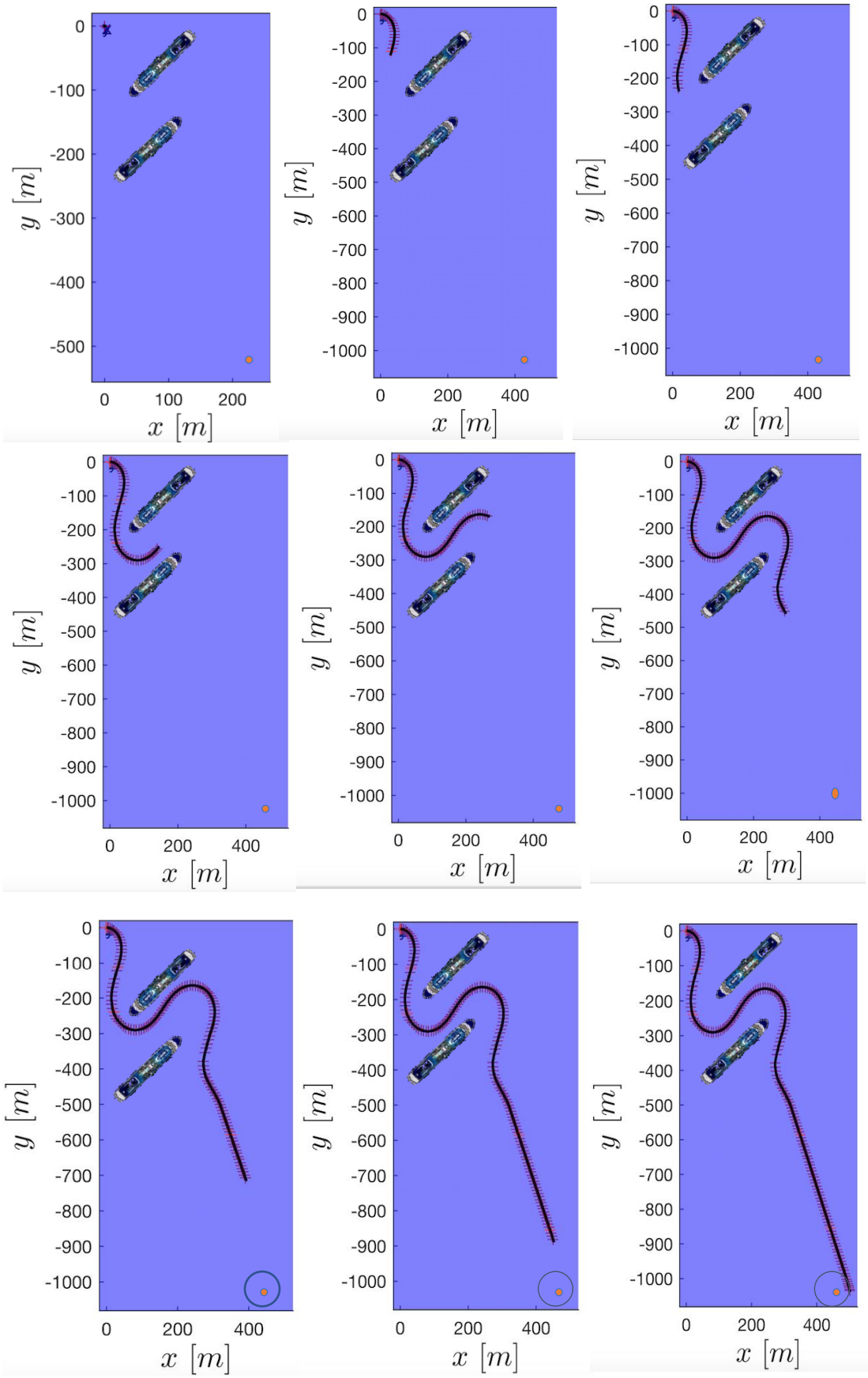

Figure 53: Trajectory evolution, obstacle avoidance capabilities, target reaching

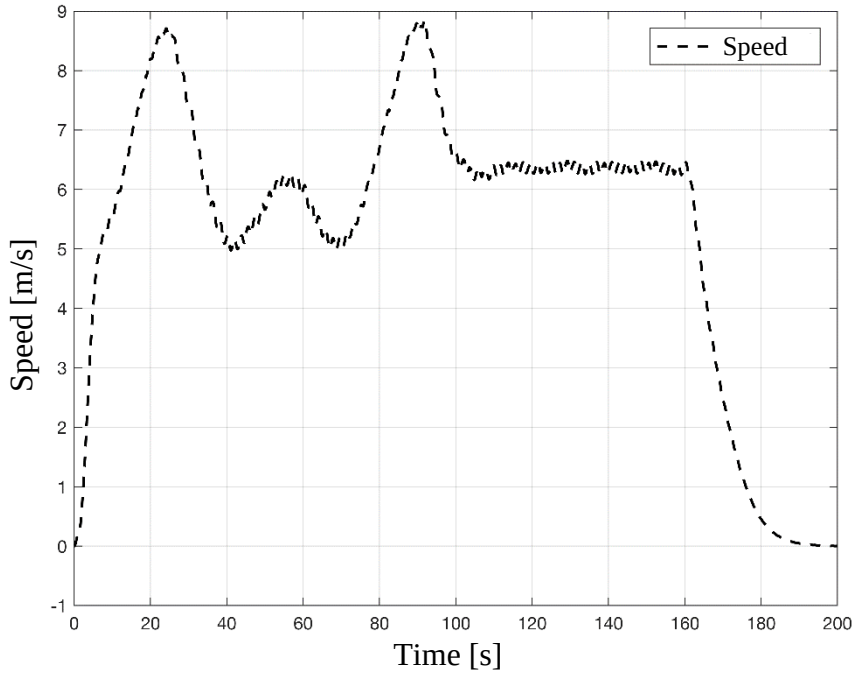

Figure 54: Navigation speed

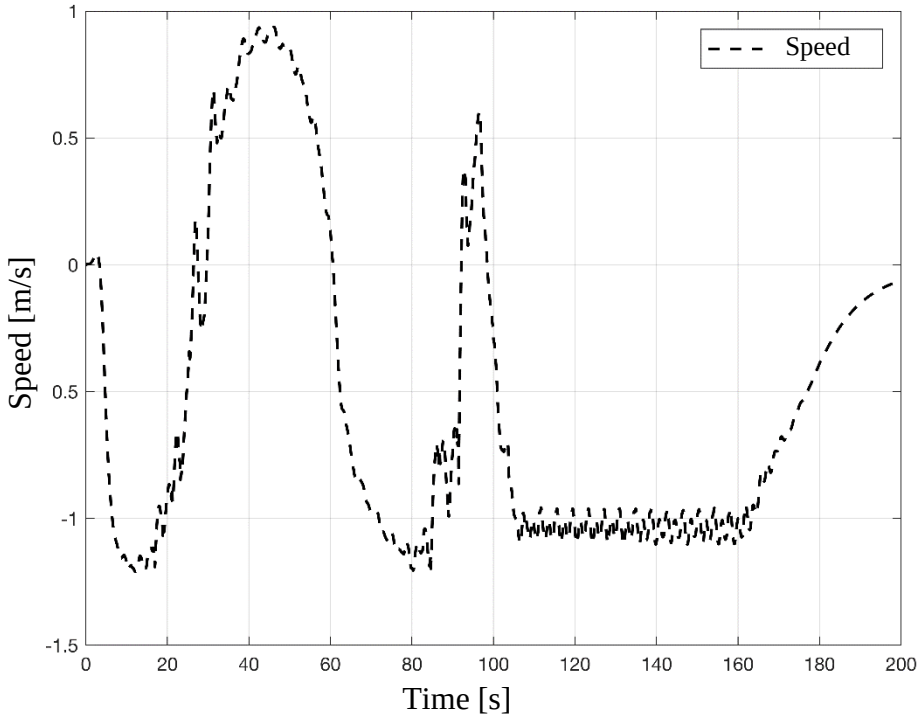

Figure 55: Lateral speed through the obstacles

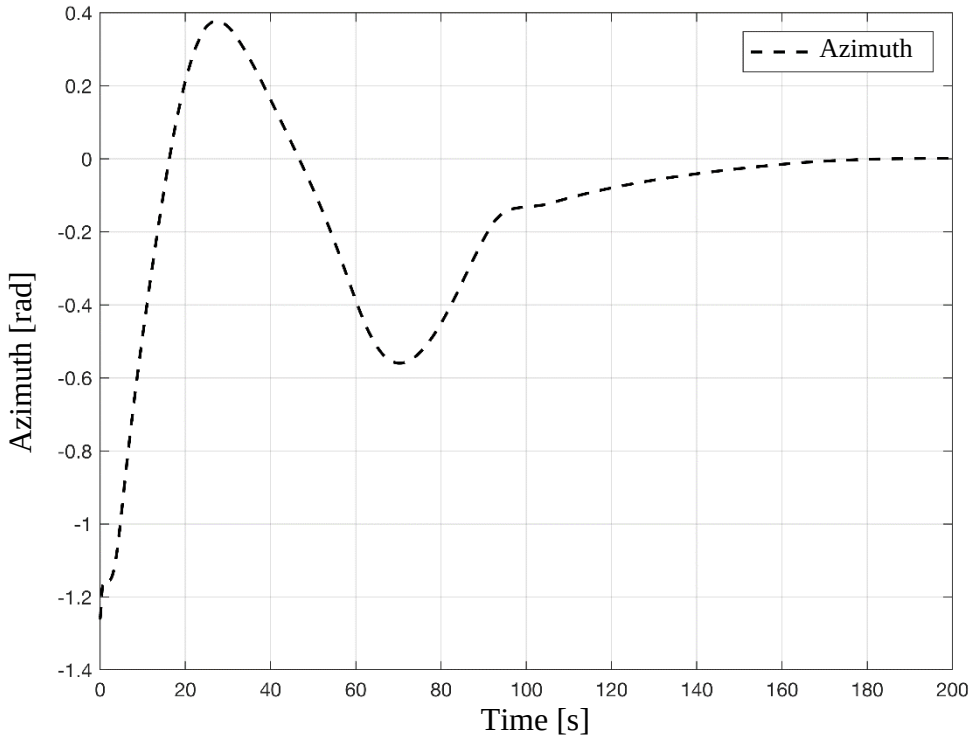

Figure 56: Azimuth evolution

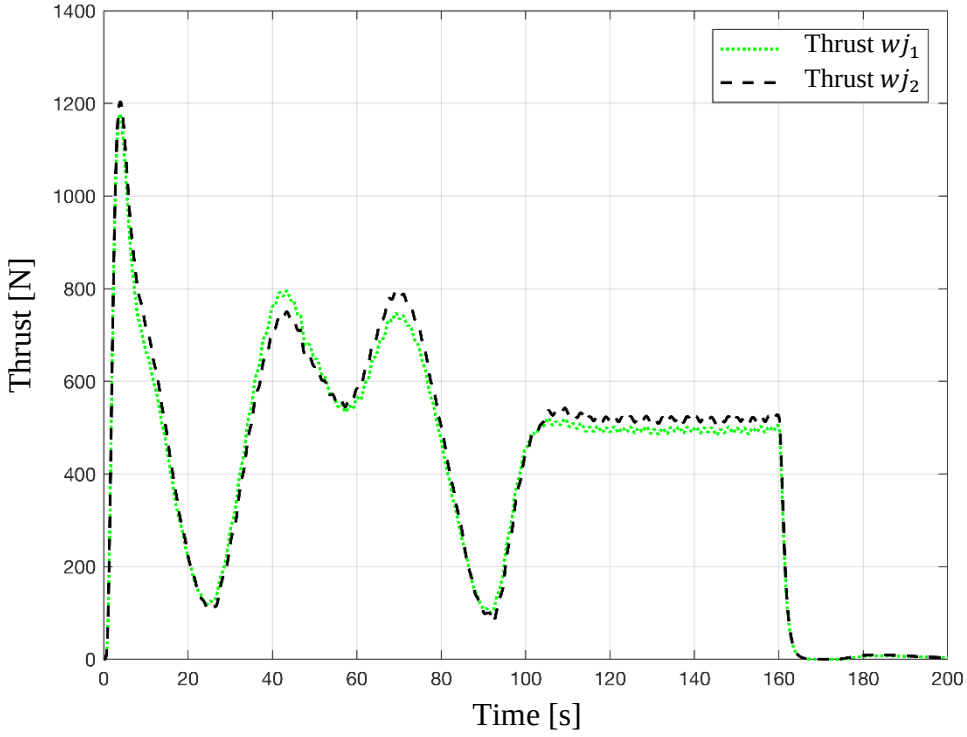

Figure 57: Jet pumps thrusts

The vehicle is guided towards the target using the azimuth formulation (125); the azimuth evolution is shown in fig. 56, two oscillation is observable and are due to the avoidance maneuvering performed to skip the two obstacles, once this maneuver is complete the vehicle points to the target to reach it.
Figures 57 illustrate the commands sent to the actuators, by the FLOP, to vary the thrust of the two waterjets.
The results obtained through this simulation were investigated and confirmed by the experimental campaign performed in the lake of Nemi near Rome (Italy), the following figure 58 illustrates the activity.

Figure 58: Experimental activity

The project at this time is completed, the experimental findings in terms of autonomous navigation, ditching capability, and ability of performing the rescue maneuver were deeply investigated and satisfied all the requirements set by Fincantieri.

Chapter 5

Rocket vertical landing VTVL

5.1 The rocket vertical landing problem

Vertical landing is becoming popular in the last fifteen years, a technology known under the acronym VTVL, Vertical Takeoff and Vertical Landing [54-56]. The interest in such landing technology is dictated by possible cost reductions [57], that impose spaceship's recycling. The rockets are not generally designed to perform landing operations, rather their design is aimed at takeoff operations, guaranteeing a very high forward acceleration to gain the velocity needed to escape the gravitational force. Landing, as for the Apollo 11 mission to the Moon, is an operation deputed to a lander module of the rocket body, the LEM, Lunar Excursion Module. As a new frontier of space discovery, space vehicles are today required to be able to land with reliability on different surfaces. Among the multiple complexities implied by the vertical landing, the control strategy plays a determinant role to obtain reliability and robustness. While take-off operations are better predictable and can be specifically designed by using suitable launch infrastructures, the landing phase is affected by higher uncertainties due to weather disturbances and ground surface imperfections [58]. The launch umbilical tower, evacuation vanes, shockwaves dissipation, vibrations insulation and accurately designed attitude during the first phases of the launch help much in facilitating the take-off operations. The return trajectory is instead weakly stable due to the presence of random disturbances. Hence, to improve the landing success probability, a feedback optimal trajectory is to be identified [58]. The "Moon landing problem" is one of the prototype problems included in many control books and it is an excellent example of a two-boundary optimization problems, that is difficult to approach by a feedback control strategy. Moreover, the vertical landing is a nonlinear problem with instabilities, analogous to the challenging control of the inverse pendulum.
The SpaceX successfully performed this task, and this study takes into the account a vehicle based on their activity Fig. 59:

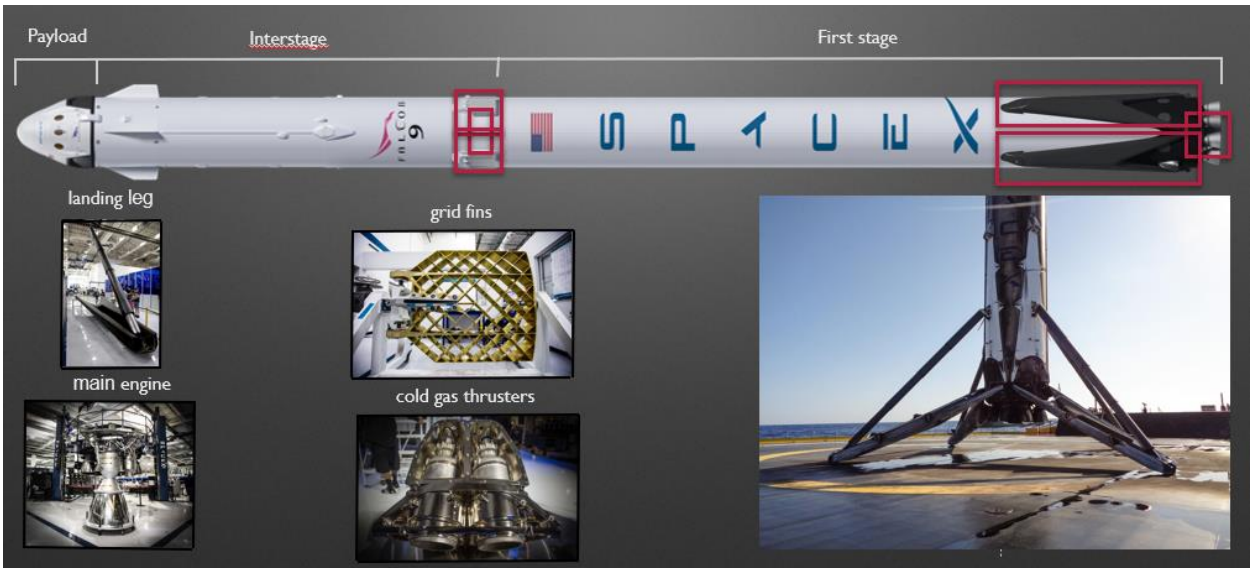

Figure 59: Experimental activity

The FLOP approach represents an interesting alternative to more classical solutions, as the LQR. The aim of this section is to present a robust and reliable control to land the vehicle safely. The quality of the control law is investigated considering the landing approach maneuver, starting from an assigned altitude, and varying the initial conditions, namely attitude and speed. The control actions involve the magnitude and the direction of the thrust, and orientable grid fins mounted on the top of the vehicle controlling the aerodynamic forces. The model of the system includes also actuators saturation effects.

5.2 Dynamic model

In this section the rocket dynamic model depicted in Fig. 59 is presented. The dynamic of the system is described by a 6 DOF rigid body motion with an additional equation describing the fuel mass consumption. The origin O of the mobile frame is placed in the geometric center of the vehicle body, since the CoG longitudinal position changes during the flight, due to the mass variation of the system. As usual for aerial vehicles, the x axis is aligned along the longitudinal axis, the y axis is set on the wing's plane, the z axis is orthogonal to the previous two Fig. 60

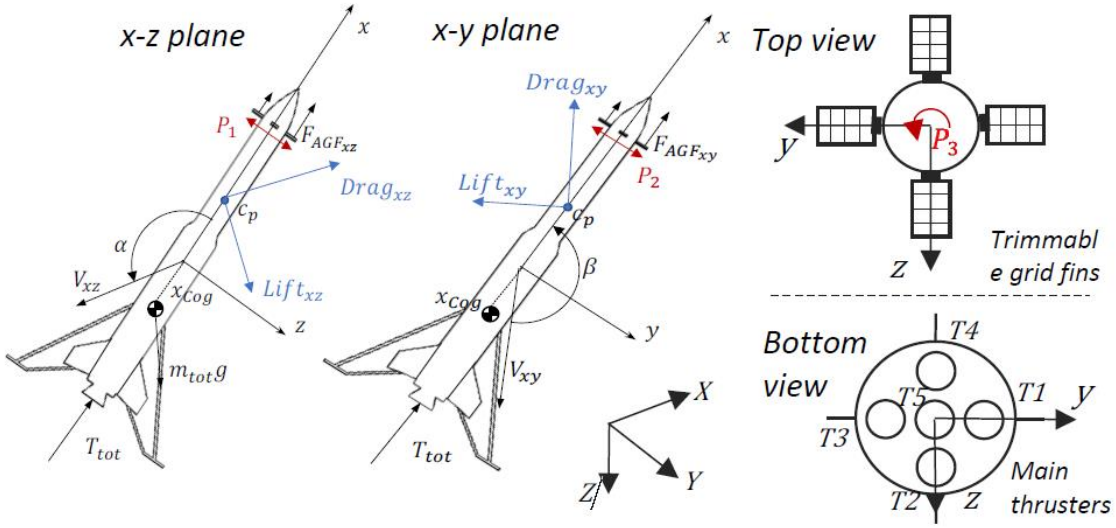

Figure 60: Rocket main systems, body reference and NED reference

The equations of motion are written within this frame in terms of the vehicle longitudinal, transverse and vertical speed components $\boldsymbol{\nu} = [u, v, w]$, along x, y and z, respectively, and in terms of the angular speed components $\boldsymbol{\omega} = [p, q, r]$, along the axes, associated to the roll, pitch and yaw motions, respectively. The absolute position $\boldsymbol{\eta} = [X, Y, Z]$ of the CoG is described within an earth fixed, NED (North-East-Down) reference frame. To avoid gimbal lock when the rocket approaches the vertical displacement, the attitude of the vehicle is described in the NED frame using quaternions $\boldsymbol{q} = [q_0, q_1, q_2, q_3]$. Hence the vehicle dynamic equation can be written as:

$$\boldsymbol{M}(t)\dot{\boldsymbol{x}} + \boldsymbol{C}(\boldsymbol{x})\boldsymbol{x} = \boldsymbol{\tau} \tag{128}$$

to which the fuel mass consumption equation is added:

$$\dot{m}_{fuel}(t) = -\gamma T_{tot} \tag{129}$$

where the total thrust is $T_{tot} = T_1 + T_2 + T_3 + T_4 + T_5$, sum of the individual forces provided by the main engines (γ is a suitable engine constant). $\boldsymbol{x} = [\boldsymbol{\eta}, \boldsymbol{q}, \boldsymbol{\nu}, \boldsymbol{\omega}, m_{fuel}(t)]$ and $\boldsymbol{M}(t), \boldsymbol{C}(\boldsymbol{x})$ are the inertia matrix and the generalized Coriolis matrix, respectively.
The external forces $\boldsymbol{\tau}$ collect the gravity action $\boldsymbol{\tau}_G$, the aerodynamic forces $\boldsymbol{\tau}_A$ acting on the vehicle body, the main thrusters forces $\boldsymbol{\tau}_{T_i}$, the cold gas thrusters actions $\boldsymbol{\tau}_{P_j}$ and the forces generated by the trimmable grid fins $\boldsymbol{\tau}_{AGF_k}$:

$$\boldsymbol{\tau} = \boldsymbol{\tau}_G + \boldsymbol{\tau}_A + \sum_{i=1}^{5} \boldsymbol{\tau}_{T_i} + \sum_{j=1}^{3} \boldsymbol{\tau}_{P_j} + \sum_{k=1}^{4} \boldsymbol{\tau}_{AGF_k} \tag{130}$$

Where the generic $\boldsymbol{\tau}_{\boxtimes} = [\boldsymbol{0}_{7,1}; \boldsymbol{F}_{\boxtimes}; \boldsymbol{M}_{\boxtimes}; 0]$. The gravity action is $\boldsymbol{F}_g = \boldsymbol{J}^T(q_0, q_1, q_2, q_3)[0,0, m_{fuel}g]^T$, with $\boldsymbol{J}$ is the transformation matrix from the vehicle to the NED Earth reference. Since the dynamic equations are written in the body frame, the CoG position varies during the flight, and the gravity action generates torque $\boldsymbol{M}_g = [x_{CoG}, 0,0] \times \boldsymbol{F}_g$. Analogously, for aerodynamic action $\boldsymbol{F}_{Aero}, \boldsymbol{M}_{Aero}$. These last depend on the angle of attack $\alpha = \text{atan}\,(w/u)$, and $\beta = \text{atan}\,(v/u)$, the sideslip angle. Drag and Lift coefficients C_D, C_L for the forces acting in the two planes xy and xz are introduced, together with the effective cross section areas A, the position of the centre of pressure c_p, and are expressed through nonlinear function of the attack and sideslip angles as $C_{D_{xz}}(\alpha), C_{L_{xz}}(\alpha), C_{D_{xy}}(\beta), C_{L_{xy}}(\beta), A_{xz}(\alpha), A_{xy}(\beta), c_{p_{xz}}(\alpha), c_{p_{xy}}(\beta)$, while dependences from $\dot{\alpha}$ and $\dot{\beta}$ are neglected.
These permit to evaluate the aerodynamic forces due to the airflow around the rocket body, with $i = y, z$.

$$\begin{aligned} D_{xi} &= \frac{1}{2}\rho_{air}(Z) A_{xi} C_{D_{xi}} V_{xi}^2 \\ L_{xi} &= \frac{1}{2}\rho_{air}(Z) A_{xi} C_{L_{xi}} V_{xi}^2 \end{aligned} \tag{131}$$

The air density $\rho_{air}(Z)$ is a nonlinear function of the height Z. Torque associated to the set of forces are:

$$\boldsymbol{M}_{Aero} = [c_{p_{xy}}, 0,0] \times \boldsymbol{F}_{Aero_{xy}} + [c_{p_{xz}}, 0,0] \times \boldsymbol{F}_{Aero_{xz}} \tag{132}$$

Analogous expressions follow for $\boldsymbol{\tau}_{T_i}$ and $\boldsymbol{\tau}_{P_j}$, these last due to cold gasses thrusters P_1, P_2, P_3, designated to control the vehicle attitude in the LEO (Low-Earth-Orbit).
When the vehicle approaches the atmosphere during the descent phase, the cold gasses thrusters have not enough power to control the vehicle attitude. Hence, the actions $\boldsymbol{\tau}_{AGF_k}$ become predominant that through suitable variations of their angles of attack δ_k modify the aerodynamic forces to stabilize the vehicle's flight.
The forces and torques $\boldsymbol{F}_{AGF}, \boldsymbol{M}_{AGF}$ are born because of the trimmable fins and they are:

$$\begin{aligned} D_{fin_k} &= -\frac{1}{2}\rho_{air}(Z) A_{fin_k} C_{D_k}(\delta_k + \phi) V_k^2 q(\phi) \\ \boldsymbol{F}_{AGF} &= \sum_{k=1}^{4} \boldsymbol{F}_{AGF_k}(D_{fin_k}) \end{aligned} \tag{133}$$

$$\boldsymbol{M}_{AGF} = \sum_{k=1}^{4} \boldsymbol{b}_k \times \boldsymbol{F}_{AGF_k}\left(D_{fin_k}\right)$$

where for the $k-th$ fin, A_{fin_k} is the wing section area, $C_{D_k}(\delta_k + \phi)$ is its drag coefficient, depending on δ_k and on the angle ϕ equal to α or β depending on the considered fin. V_k represents the component of the CoG velocity along the x axis, the parameter $q(\phi)$ is the shadowing coefficient that varies between 0 and 1 depending on its configuration, and finally $\boldsymbol{b}_k$ is the position vector of the $k-th$ fin.

5.3 Application of the FLOP control

The control is performed introducing a quadratic penalty function of the state $\boldsymbol{x}$ and target $\boldsymbol{x}_T$:

$$g(\boldsymbol{x}) = \frac{1}{2}(\boldsymbol{x} - \boldsymbol{x}_T)^T \boldsymbol{Q}(\boldsymbol{x} - \boldsymbol{x}_T) \tag{134}$$

The matrix $\boldsymbol{Q}$ is suitably chosen with standard criteria. The vehicle flight is composed by three main phases as shown in fig. 61: the first is the attitude correction in LEO. The vehicle actuates the FLIP maneuver to reach the desired pitch. The state target is referred to a specific attitude and null angle rates $\boldsymbol{x}_{T_{FLIP}} = [\boldsymbol{0}_{3\times1}, \boldsymbol{q}_T, \boldsymbol{0}_{3\times1}, \boldsymbol{0}_{3\times1}, 0]$, hence $\boldsymbol{Q}_{FLIP} = diag\left(\left[\boldsymbol{0}_{3\times1}, K_{\boldsymbol{q}}\boldsymbol{1}_{4\times1}, \boldsymbol{0}_{3\times1}, K_{\boldsymbol{\omega}}\boldsymbol{1}_{3\times1}, 0\right]\right)$.
In the second phase, the vehicle reaches the re-entry speed and pitch angle. The target is $\boldsymbol{x}_{T_{reentry}} = [\boldsymbol{0}_{3\times1}, \boldsymbol{q}_T, \boldsymbol{v}_T, \boldsymbol{0}_{3\times1}, 0]$, and $\boldsymbol{Q}_{reentry} = diag\left(\left[\boldsymbol{0}_{3\times1}, K_{\boldsymbol{q}}\boldsymbol{1}_{4\times1}, K_{\boldsymbol{v}}\boldsymbol{1}_{3\times1}, K_{\boldsymbol{\omega}}\boldsymbol{1}_{3\times1}, 0\right]\right)$.
The third phase is the atmospheric flight terminating with the vertical landing operation. The target is $\boldsymbol{x}_{T_{landing}} = [\boldsymbol{0}_{3\times1}, \boldsymbol{q}_T, \boldsymbol{v}_T, \boldsymbol{0}_{3\times1}, 0]$, and $\boldsymbol{Q}_{landing} = diag\left(\left[\boldsymbol{0}_{3\times1}, K_{\boldsymbol{q}}\boldsymbol{1}_{4\times1}, K_{\boldsymbol{v}}\boldsymbol{1}_{3\times1}, K_{\boldsymbol{\omega}}\boldsymbol{1}_{3\times1}, 0\right]\right)$.

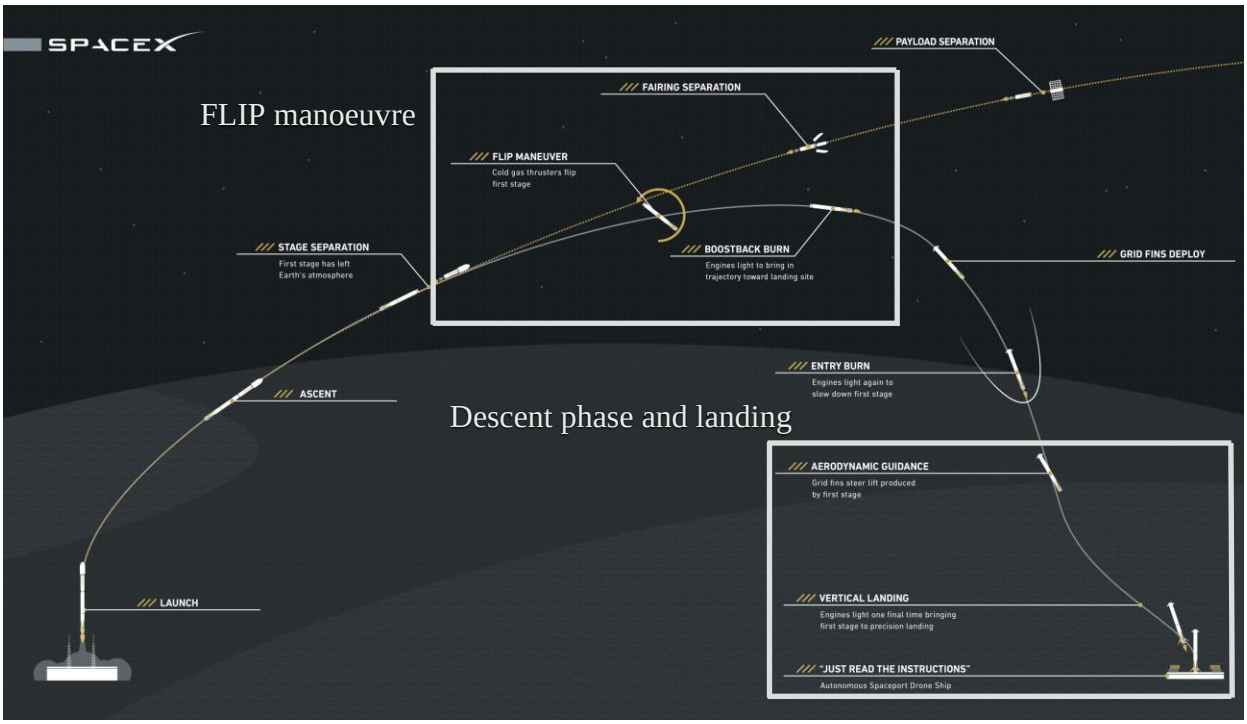

Figure 61: Rocket flight phases

5.4 Results

The simulations consider a rocket with the following characteristics:

Characteristics	Value	Characteristics	Value
Rocket mass	20000 [kg]	Nr. Lateral thrusters	8
Fuel mass	150000 [kg]	Max lateral thrust	400 [N]
Nr. Main thrusters	5	Nr. Grid fins	4
Max thrust T	1521.4 [kN]	Max grid trim angle	±60 [°]

Table 6. Rocket's parameter

In the FLIP maneuver, the vehicle flies at 100 [km] above the Earth surface at a speed of 10000 [km/h], with initial pitch 45 [°]. Three major phases can be identified in this maneuver as shown in fig 62 and 63, which show the maneuver phases and the evolution of the pitch angle its rate and the control provided by the cold gas thrusters commanded by the FLOP.
In the first phase, the lateral thrusters provide the required force to starts the rotation of the vehicle, second, when the vehicle is rotating and it is approaching the desired orientation of 180 [°], the cold gas thrusters starts to brake the rotation of the vehicle, slowing it down, third, the vehicle reaches the desired horizontal position, with zero residual speed. The aim of this maneuver is to rotate the vehicle to make it approaches the atmosphere with the engines pointing forward, because these will slow down the vehicle during the powered descent phase and will control the vehicle vertical attitude during the final landing.

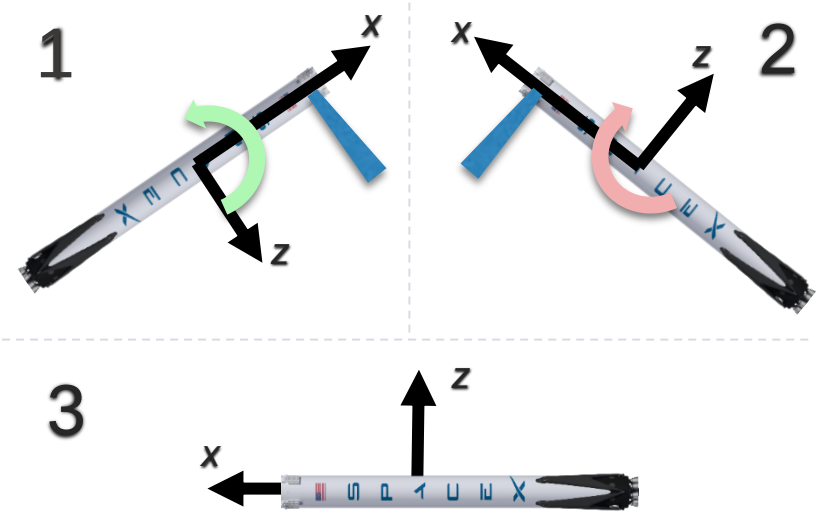

Figure 62: FLIP maneuver phases

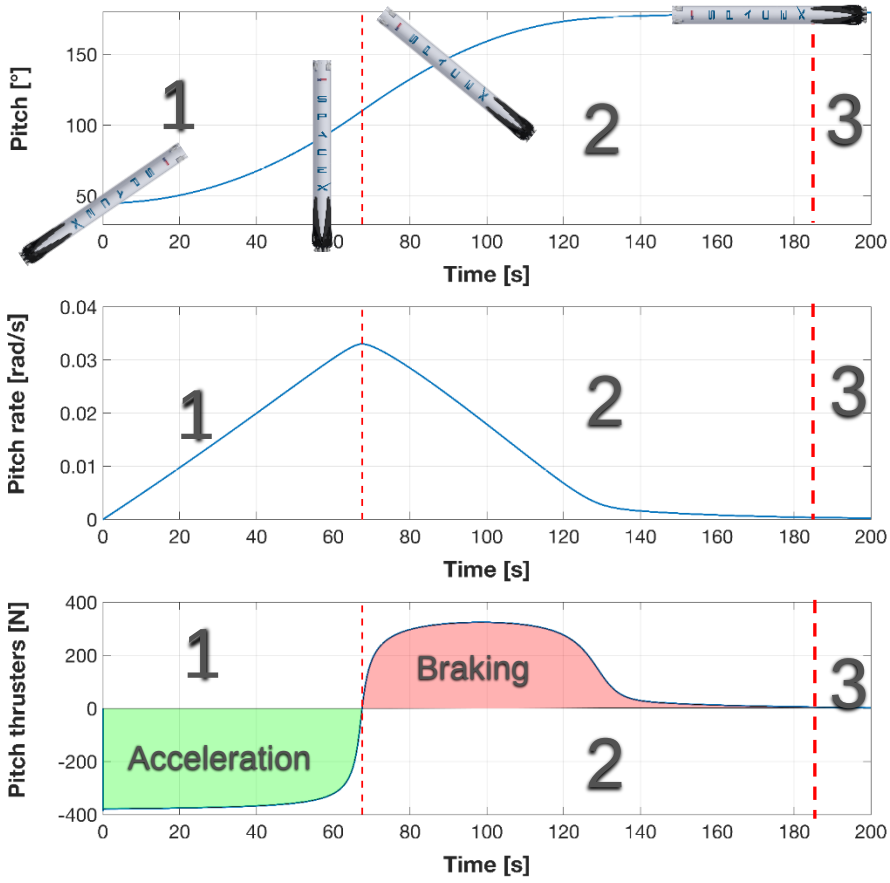

Figure 63: FLIP maneuver angle rate and control

In the second phase, the rocket is still in LEO, flying 100 [km] above earth surface, travelling at 10000 [km/h], with initial pitch 180 [°]. The value required for the pitch to safely approach the atmosphere is 80 [°], the maneuver is shown in fig 64. Moreover, the vehicle approaches the atmosphere reducing the effect of gravity using the main engines.

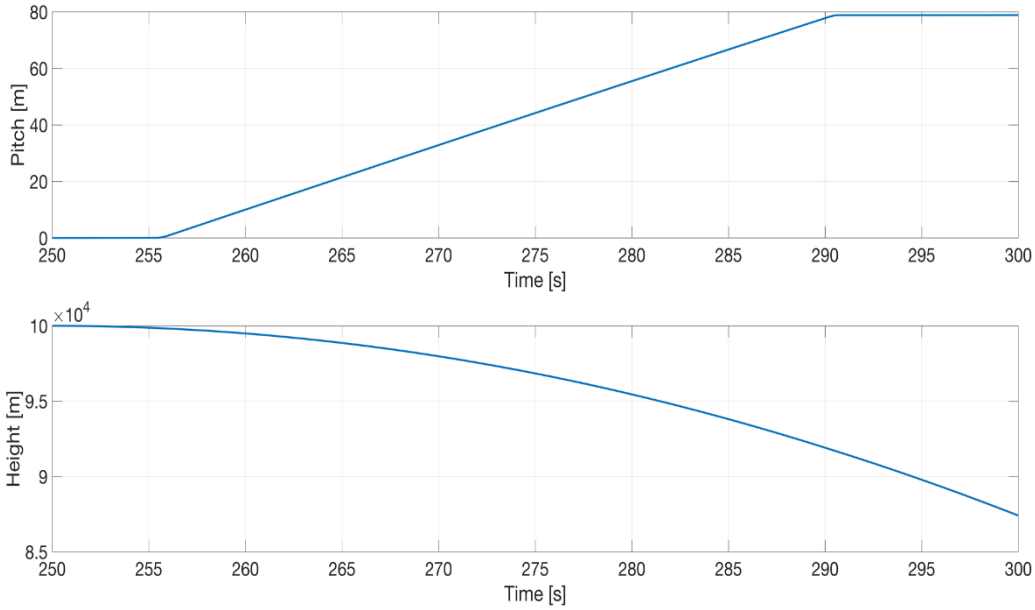

Figure 64: reentry maneuver

Eventually, the landing phase is shown in fig. 65 and 66. Here the vehicle is travelling through the atmosphere starting from a height of 30 [km] at 4320 [km/h], thanks to the grid fins and the main thrusters, it safely performs the vertical landing. Fig. 66 shows the last part of the landing, the speed evolution, the pitch stabilization and the nonlinear behavior of the main central engine of the vehicle.

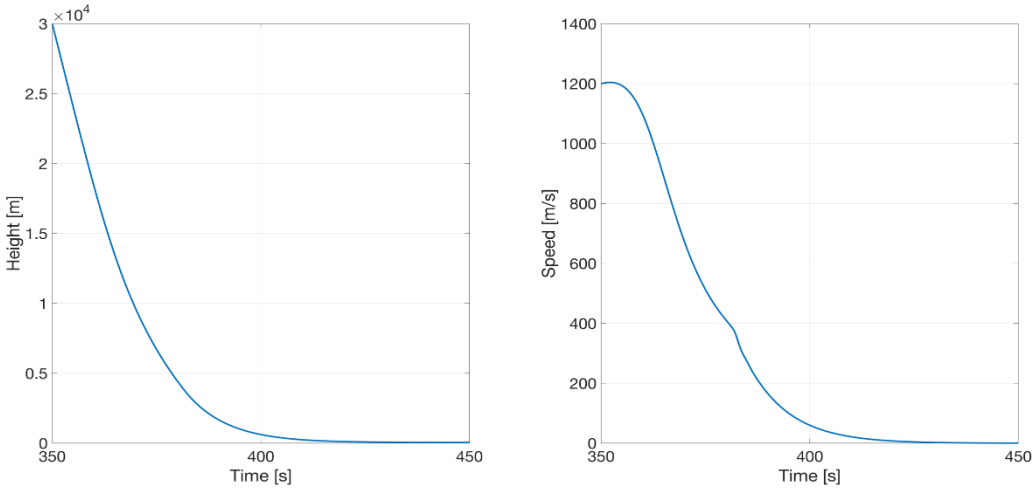

Figure 65: Vertical landing maneuver

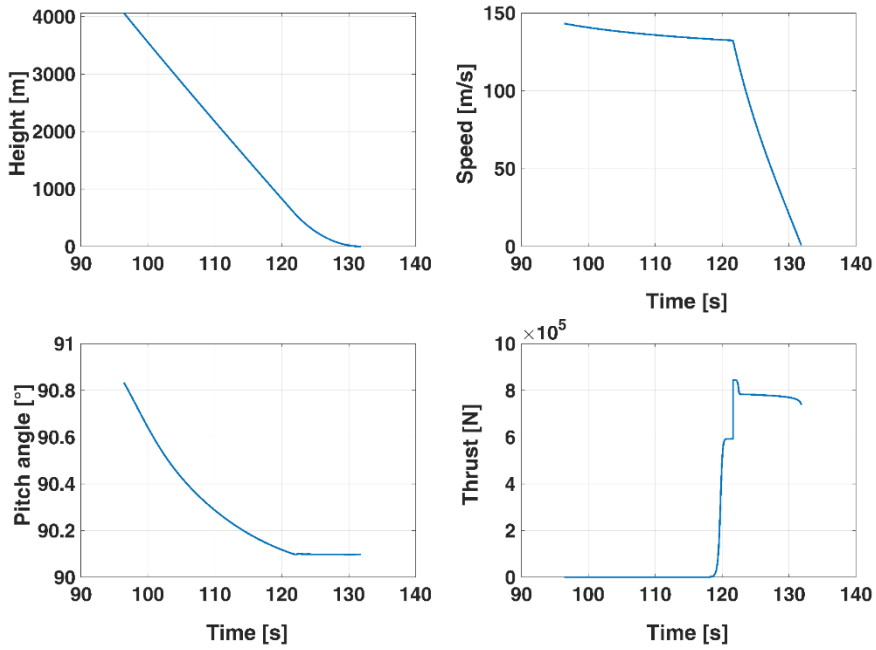

Figure 66: Vertical landing final approach, speed, pitch angle, and thrust

Finally, a landings comparison in presence of wind with different intensities is shown in fig. 67, the aim of this investigation was to understand which the limits of the controlled system are, when wind affect the vehicle dynamics.
The figure shows that wind's speed in the range of $50 - 70$ [km/h] can be handled by the controlled system, even though some misalignment of the final landing spot is observed, while when the wind reaches higher speed the vehicle is fails to land and has to use the engine to gain height, control the pitch and try to land in another point distant from the desired landing spot.

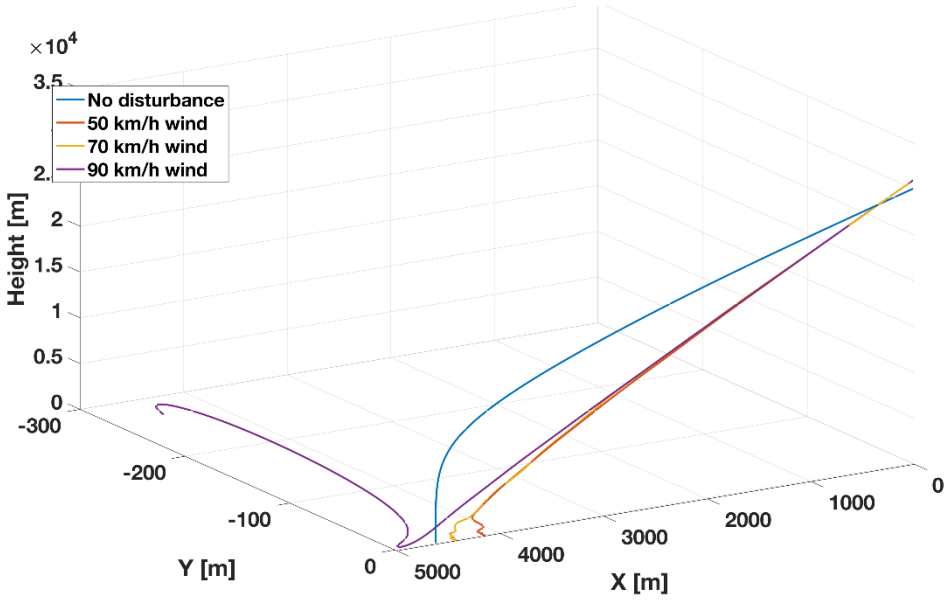

Figure 67: Vertical landing final approach, speed, pitch angle, and thrust

The FLOP control shows good performances in all the phases that characterize the vehicle flight and landing, in a compound complex control operation. These results are possible thanks to the FLOP formulation, that allows to consider the nonlinearities, typical of the rocket model.
The controlled system is also tested in presence of wind disturbances, in this case the results seems to be promising even though they might be improved with different tuning or penalty function specifically designed to counter react the wind effect.

Chapter 6

Micro magnetic robots actuated by an MRI

6.1 Micro magnetic robot actuated by an MRI introduction

Recently new techniques for non-invasive treatment of stomach cancers as well as cardiovascular system diseases are of high interest, in particular MRI-powered untethered robots, represent an interesting technology to this aim. The technology is based on a Magnetic resonance imaging (MRI) device used to actuate magnetic robots remotely inside the human body, thanks to their feature of generating magnetic field gradients, that are generally used to obtain high-resolution tissue images for diagnostic purposes. However, some limitations for robot actuation occur, due to the imaging requirements, that affect the number of active degrees of freedom available for magnetic actuation. Generally, MRI-powered untethered robots are only translational actuated by being pulled in three dimensions using the magnetic gradient fields [76-80].
A proper vehicle design with the innovative control law FLOP permits to overcome these limitations, leading to a controlled system that permits to reach desired position and orientation for these robots. The results that are presented throughout this chapter refer to an untethered magnetic robot, moving in a liquid volume in presence of a magnetic environments like those in MRI devices, experimental setup shows that the vehicle is capable of move and rotate in the volume of the considered fluid reaching the desired position and attitude. The tests are carried out inside a commercially available MRI gradient coil, in silicon oil fluid. These MRI controlled untethered micro robots represent a promising technology for medical applications in which precise control of vehicle position and attitude are required [82].
The recent advances in imaging provide the chance to perform revolutionary procedures, in fact this feature permits the online decision-making that in the past required a direct line of sight to the surgical site. This coupled with the advances in surgical robotics permitted an increase in terms of accuracy of surgical operations and reduces the post-surgical effects and hence reduce the healing time [76,77]. MRI systems used in combination with advanced robotics represent a promising field of research with interesting perspectives to evolve the actual surgical procedures and reduce the trauma suffered by the patients [76-78]. MRI machines provide high-contrast images of tissues without ionizing radiation [79-81], moreover it is recently demonstrated that these devices can remotely actuate micro magnetic robot through electromagnetic coil that produce magnetic gradients, these system are already present within the machine for imaging purposes [76,83-89], these magnetic micro robots permit the surgeon to operate in the surgery site, reducing sensibly the invasivity of the procedure, while having an accurate sight of the interested site thanks to the imaging capabilities of the MRI devices.
In MRI systems three main magnetic fields act, these are the main uniform high magnetic field, $\mathbf{B}0$, the magnetic field gradients, $\nabla\mathbf{B}$, and the radio frequency (RF) magnetic field, $\mathbf{B}1$. $\mathbf{B}0$ is unidirectional, always present, and is very high (1.5 T and above). Given its high strength, $\mathbf{B}0$ causes all ferromagnetic materials inside the device to become magnetized to saturation and align with it, and hence maneuvers that demand high torques generated by large variation of the direction of the magnetic field are unfeasible within the device [90-97].
Some small forces can be generated using the magnetic field gradients ($\nabla\mathbf{B}$) as expressed in Appendix A, these permitted to the researchers to demonstrate that 3 DOF motion is feasible, and hence position control of untethered micro robots is possible [83,84,98,99].

Orientation control may open new possibilities for applications where this becomes strongly important, e.g. control of a pill sided camera, small needles for biopsy or injections, by the way orientation control of the untethered devices is difficult to be realized because magnetic torques cannot be directly applied to magnetic bodies inside the MRI scanner. However properly designed robot can achieve the ability to get desired position and orientation, even though some limitations are still present due to coupled dynamics. These robot exhibit 5 out of 6 DOF, namely positioning (3 DOF), pitch and yaw angles (2 DOF), while roll is not achievable by the actual design, but this doesn't represent a restriction to robot tasks, since the robot are usually cylindrically and therefore symmetric around the roll axis.
The Department for Intelligent Physics of the Max Planck Institute for Intelligent systems has recently designed a new design for this class of robot, and a remote magnetic actuation for them as well, these permit to the robot to achieve position and desired orientation in a magnetically constrained environment like the one inside an MRI [100]. This design generates the pulling forces using magnetic field gradients, these are applied to a magnet that is free to rotate and is placed away from the center of gravity of the vehicle, and hence the forces applied to it generate torques that act on the vehicle body, these are also used to generate translation of the robot. Even though the presented vehicle is able to perform the desired task in terms of position and orientation, one at time, it also exhibits a coupled dynamic for translations and rotations, moreover the peculiar design, i.e. displacement of the center of buoyancy with respect to the center of gravity as well as some misalignment of this due to fabrication imperfections, cause a natural pitched attitude for it.
In order to obtain the final desired position as well as the desired orientation together, the new control FLOP presented in this work has been applied to this application. The goal of the control is to maximize the overall maneuverability of the magnetic robot in a 3D liquid volume.
The results provided by the controlled system shows good performances, even though some limitations due to the vehicle design are still present.

6.2 Robot design concept

The aim of the design of the remotely actuated robots, proposed by the department of Physical Intelligence of the Max Planck Institute for intelligent systems, is to improve vehicle maneuverability when moving in 3D into a viscous fluid and in the presence of a nearly uniform **B0** field. Where nearly uniform field means that the spatiotemporal changes of the field are small compared to the mean value of the field. The vehicles are remotely actuated by the MRI gradient coil insert, which generates the 3D field perturbations. A 1 mm-diameter spherical NdFeB permanent magnet is placed in a cavity on the robot body that is offset from the center of mass (COM) of the robot as in Fig. 68.

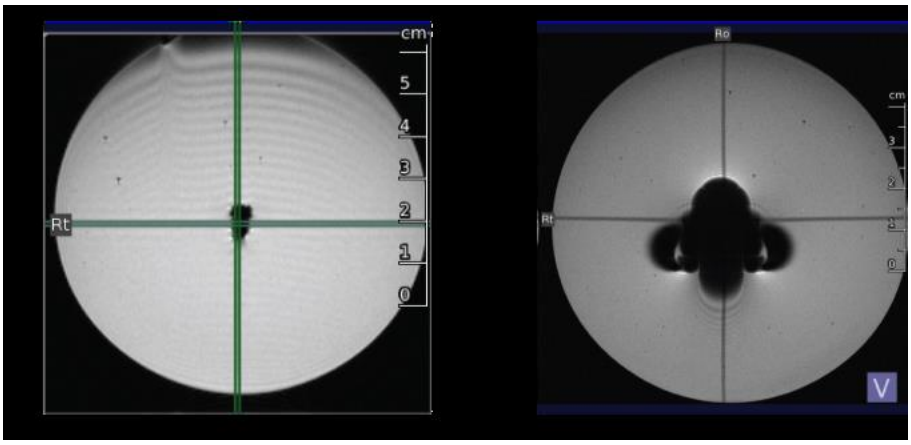

Figure 68: Magnetic resonance (MR) images of an SFNU type robot: (a) MR image of the robot without the magnetic sphere, and (b) MR image of the robot with the magnetic sphere, which distorts the image.

Since the magnet is not rigidly connected to vehicle, but it's just placed into the cavity, it can rotate freely with respect to the robot body, but it can transmit the forces, generated by the magnetic gradients, to the robot's body.
This design permit to the magnet to align itself to the main magnetic field **B0**, without affecting the robot attitude. The position of the magnet into the vehicle body, is out of the overall center of mass COM of the vehicle, therefore the pulling forces, generated by the magnetic gradients, applied to the small magnet, generate also torques that act on the vehicle orientation, the scope of this design is to improve the maneuverability of the vehicle during the 3D motion into a vicious fluid, but some limits appear evident, the translational and rotational dynamics of the vehicle are coupled, therefore any force generate linear motion as well as rotation. Since most of the medical applications require a motion in confined spaces, a high maneuverability is necessary. To maximize the maneuverability of the robot, the coupling between translation and rotation should be minimized. Clearly the distance between the magnet and the center of gravity $\boldsymbol{b_m}$ improve the torques and hence the rotational effect of the pulling forces, so maximize this distance augment vehicle maneuverability, anyway the undesirable coupling effect is impossible to be avoided.
Robot design must take into the account the fluid density, in fact, to reduce the magnetic forces effort required to lift up the vehicle and to move it through the fluid, the robot has to have a density close to the one of the fluid in which it moves.
The buoyancy force and its torque, $\boldsymbol{F_{buoyancy}}$, $\boldsymbol{M_{buoyancy}}$, and the gravitational force, $\boldsymbol{F_{gravity}}$, cause drifts in the position and orientation of the robot, also in steady state, these actions to be counter reacted by the magnetic pulling force in order that the robot can move in any direction. Therefore, the following inequalities must be satisfied:

$$\begin{aligned} |\boldsymbol{F_{balance}}| &< \left|\boldsymbol{F_{magnet_{max}}}\right| \\ \left|\boldsymbol{M_{buoyancy}}\right| &< \left|\boldsymbol{b_m} \times \boldsymbol{F_{magnet_{max}}}\right| \end{aligned} \tag{135}$$

Where $\boldsymbol{F_{balance}}$ is the force required to balance the buoyancy and gravity forces acting on the vehicle, $\boldsymbol{F_{magnet_{max}}}$ is the maximum magnetic pulling force and $\boldsymbol{b_m} \times \boldsymbol{F_{magnet_{max}}}$ is the maximum induced magnetic torque on the robot's body. $\boldsymbol{F_{balance}}$ and $\boldsymbol{M_{buoyancy}}$ can be tuned during the design of the robot varying the robot volume $V_{vehicle}$, its mass M, and the distance between the center of volume CoV and the center of mass of the vehicle CoM.

The magnetic field gradients that an MRI can generate are relatively weak, therefore the inequalities in (135) should be considered carefully for the design of the robot.
To obtain a neutral buoyant vehicle two major characteristics has to be respected:

- The CoM and CoV should be located at the same position
- The overall density of the robot should be equal to the liquid's density

Since some manufacturing error always occur and since the magnet need some space to able to rotate freely in the cavity, these conditions are difficult to be matched in a real prototype. Even though the prototype got close to the ideal prototype, some magnetic forces are always required to maintain the vehicle in the derided position. This result into a vehicle that requires an advanced control logic that might take into the account the dynamic model of the system, and hence the dynamic constraints of the robot, and all of the consequent nonlinearities, of the system.
Fig. 69 shows four different configurations of the robot in steady state within a fluid environment. The robot is assumed to stay stationary inside a liquid, $\boldsymbol{F_{balance}}$ is applied to counter react to the buoyancy and gravity actions and to maintain the robot at the desired altitude, moreover two torques act on the robot: $\boldsymbol{b_m} \times \boldsymbol{F_{balacne}}$ and $\boldsymbol{b_{buoyancy}} \times \boldsymbol{F_{buoyancy}}$.

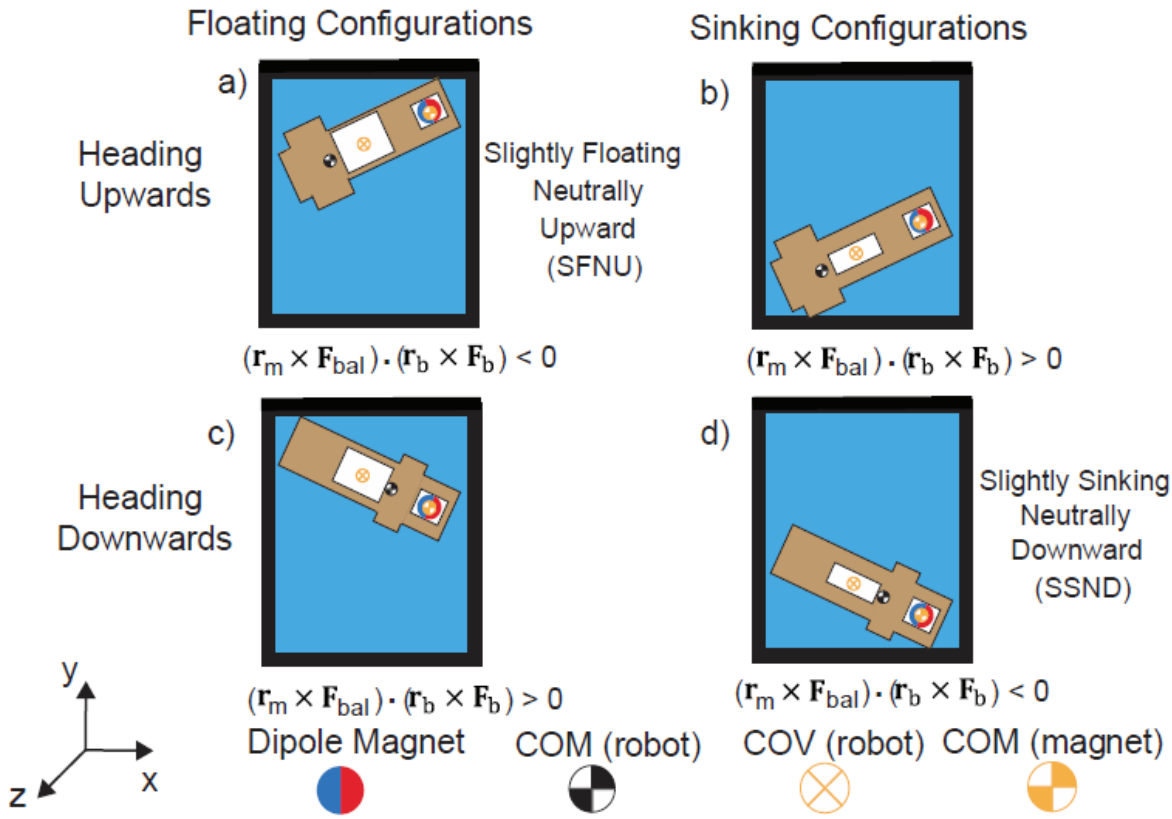

Figure 69: Depending on the density of the robot and the position of COM and COV, four different configurations can be possible inside stagnant fluids at a resting state when there is no magnetic actuation input.

To improve the vehicle maneuverability and hence to obtain the desired robot configuration, the terms that appear in these equations, have to be minimized.

All the designs are axisymmetric and hence CoM and CoV are placed on the longitudinal axis of the vehicle, even though some misalignments occur due to the manufacturing process. Anyway in the ideal case the torques $\boldsymbol{b_m} \times \boldsymbol{F_{balacne}}$ and $\boldsymbol{b_{buoyancy}} \times \boldsymbol{F_{buoyancy}}$ are parallel and perpendicular to the vertical plane that contains the longitudinal axis of the vehicle, this means that a proper choice for them might result into a minimization of the effect due to them.

$$\boldsymbol{b_m} \times \boldsymbol{F_{balacne}} + \boldsymbol{b_{buoyancy}} \times \boldsymbol{F_{buoyancy}} = \mathbf{0} \tag{136}$$

Among the four possibilities shown in Fig. 4, the configurations (b) and (c) result in $\boldsymbol{b_m} \times \boldsymbol{F_{balacne}}$ and $\boldsymbol{b_{buoyancy}} \times \boldsymbol{F_{buoyancy}}$ are in the same direction, and therefore, the induced torques are augmented, causing an increased rotational drift. Instead, configurations (a) and (d) produce parallel but inverse torques, and hence the magnetic action helps also to reduce the action due to buoyancy force. These designs reduce the rotational drift. The configuration (a) is a slightly floating neutrally upward (SFNU) robot type, and the configuration (d) is a slightly sinking neutrally downward (SSND) robot type.

6.3 Dynamic model

The FLOP algorithm is a model-based sub optimal control, and hence a model of the controlled system is required to generate all the functions needed by the algorithm. The model used here, considers two main reference frames, the world fixed reference frame fig. 70 in which the vehicle's position X, Y, Z and orientation $q0, q1, q2, q3, q4$ are described. The vehicle attitude is expressed using the quaternion formulation to avoid singularities that might occur for some poses of the robot. The vehicle configuration is retrieved through image processing of the signals coming from two cameras placed in the setup, one of them points toward a mirror placed on top of the pool in which the robot moves giving information about its planar motion, the other one records the side of the pool giving info about the motion of the vehicle in the vertical plane as shown in fig 70.

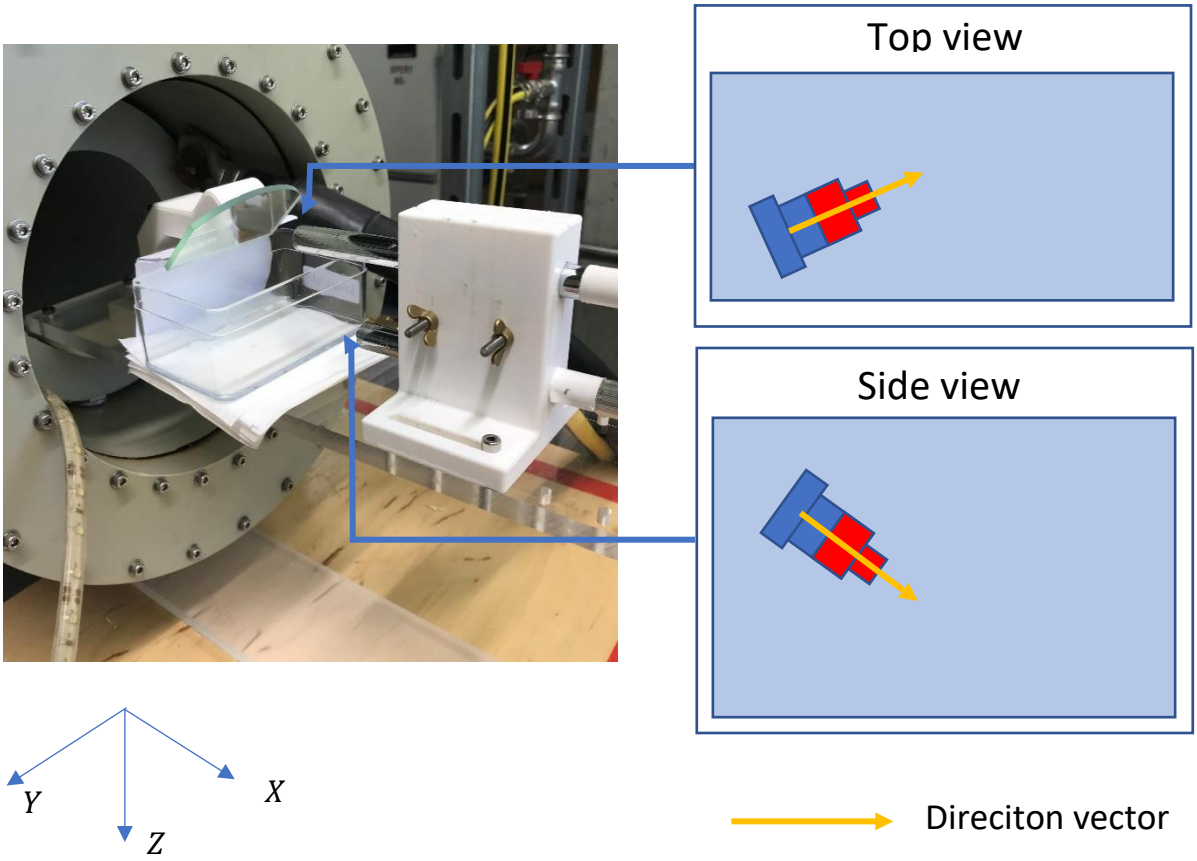

Figure 70: Experimental setup, top and side camera record the motion of the vehicle placed inside the pool, the whole system when active, is placed inside the MRI machine that appear in the left part of the figure. The Two cameras retrieve the position of the vehicle and its direction vector that permits to calculate the actual orientation of the vehicle.

The signals provide position and orientation of the vehicle, this last is obtained through the direction vector, this is mean to belong to the vehicle longitudinal axis, pointing from the back of the robot to its head, this convention is the reason why the robot is painted in red and blue color, in fact the image processing algorithm assign the direction vector pointing from the blue part of the vehicle to the red one fig. Through the components of this vector in the world fixed reference frame is possible to retrieve the actual orientation of the vehicle, by evaluating the actual Euler angles and converting them back to quaternions. Two major limitations come from this technique:

- Singularities, when the vehicle points toward one of the cameras, i.e. the longitudinal axis of it is parallel to the imaginary axis perpendicular to the image provided by the camera, in these conditions the orientation data are strongly affected by fluctuations, this might cause high control fluctuations since the jacobians of the FLOP algorithm are affected by this noisy signal.
- The roll angle is undetermined, the cameras cannot provide any information about the roll angle of the direction vector, anyway this does not have severe drawbacks on the controlled vehicle performance since the vehicle is axisymmetric, although some small misalignment and defects can occur due to the manufacturing process. One technique to overcome this lack of information might be to add some special painting with markers to the vehicle surface. Since this experimental activity is devoted to design a vehicle that might be guided only using the MRI imaging feedback this can’t recognize the painted markers, therefore in

real cases, inside a human body there won't be the possibility to determine the vehicle roll, and hence it is not considered according to this limitation of the real scenario.

The observable Euler angles i.e. pitch θ and yaw ψ, can be evaluated using the spherical coordinates formulation and knowing the components of the direction vector measured by the camera through the following:

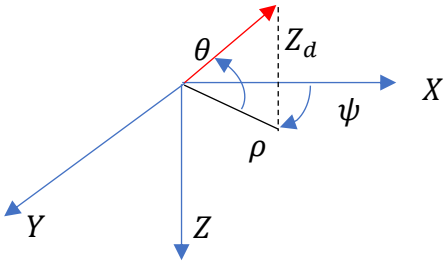

$$\theta = \text{atan}\left(-\frac{Z_d}{\rho}\right)$$
$$\psi = \sin\left(\frac{Y}{\rho}\right) \tag{137}$$

The pitch angle θ can span through $-\frac{\pi}{2} \leq \theta \leq \frac{\pi}{2}$ while the yaw angle can range through $0 \leq \psi \leq \pi$. Once these angles are evaluated it is possible to convert them to the quaternion that is fed to the controller.

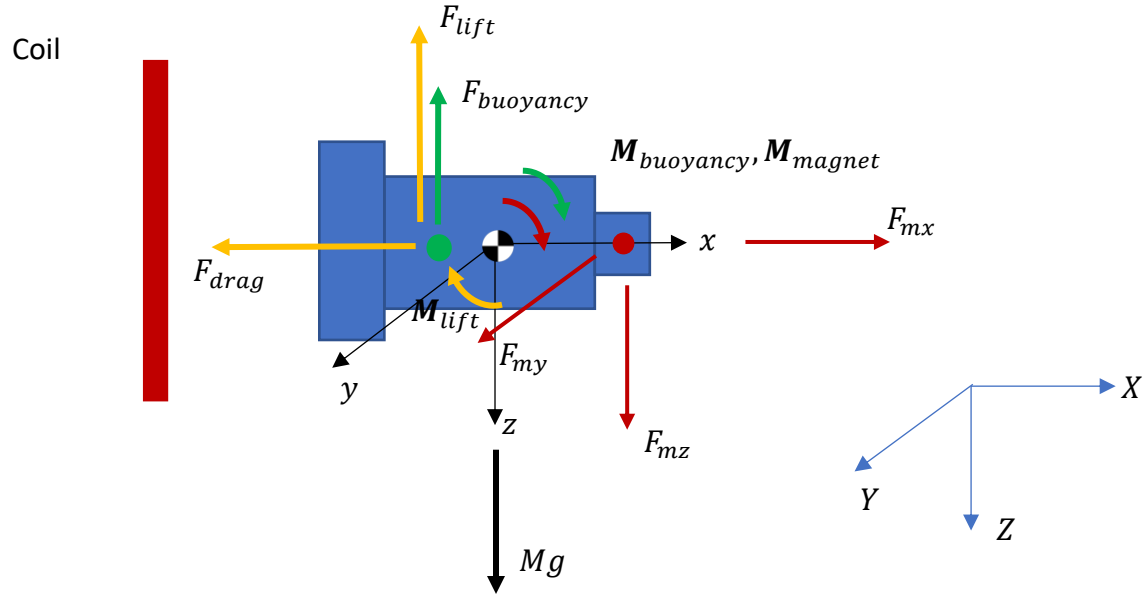

Figure 71: forces acting on the vehicle, the magnetic forces are generated by three fixed coils, and hence they are defined in the world reference frame X, Y, Z. For the sake of clarity, the torques generated by the magnetic, buoyancy and lift forces $\boldsymbol{M}_{magnet}, \boldsymbol{M}_{buoyancy}, \boldsymbol{M}_{lift}$, are meant as vectors. In the picture the torques due to rolling, pitching, and yawing motions are not reported.

The other reference frame is the body fixed frame, this has the x axis parallel to the longitudinal axis of the vehicle, the y axis pointing on the right side of the vehicle and the z axis selected to obtain a right-handed reference frame, according to the aerospace convention.
The state of the system is defined as $\boldsymbol{x} = [X, Y, Z, q0, q1, q2, q3, q4, u, v, w, p, q, r]$ where $[X; Y; Z]$ represent the position of the CoG in the fixed reference frame. Since the goal is to control the 3D motions and rotations of the vehicle, to avoid any singularity due Euler angles, the quaternion $[q0, q1, q2, q3, q4]$ is used, it provides the attitude of the vehicle in the fixed frame. The speeds components $[u, v, w]$ describe the surge, sway and heave motions respectively. Then $[p, q, r]$ represent the three angular speeds of the vehicle around its own axes. The forces and torques acting on an untethered magnetic robot in a 3D liquid environment are the magnetic, fluidic, gravity, and buoyancy forces and torques. The magnetic forces $\boldsymbol{F}_m$, represent the actuation of the system, these are generated by the coils rigidly connected to the world reference frame coordinate system i.e. X, Y, Z. These vary the magnetic field gradient along the directions of the fixed reference, this means that to control the vehicle they have to be translated into the body reference frame of the vehicle.

$$\boldsymbol{F}_{m_{body}} = \boldsymbol{g}(q0, q1, q2, q3, q4)\boldsymbol{F_m} \tag{138}$$

This term will produce a dynamic system in the form $\dot{\boldsymbol{x}} = \boldsymbol{\phi}(\boldsymbol{x}) + \boldsymbol{h}(\boldsymbol{x})\boldsymbol{u}$ that require to be manipulated to belong to the class of the affine system $\dot{\boldsymbol{x}} = \boldsymbol{\phi}(\boldsymbol{x}) + \boldsymbol{B}\boldsymbol{u}$ that is suitable for the FLOP control. Otherwise since the $\boldsymbol{g}(q0, q1, q2, q3, q4)$ transformation can also be used to map the actuations $\boldsymbol{F}_{m_{body}}$ defined directly into the body reference, into the required $\boldsymbol{F_m}$ through:

$$\boldsymbol{F_m} = \boldsymbol{g}(q0, q1, q2, q3, q4)^T \boldsymbol{F}_{m_{body}} \tag{139}$$

This permit to obtain a controlled system that belongs to the class of the affine systems treatable by the FLOP, without any approximation, or manipulation, while permitting to map the necessary forces described into the fixed frame, anyway, it is better to make the control aware of this peculiarity of the experimental setup, and introduce a linearization at each step of this part of the dynamic system as will be discussed in next paragraph. These forces generate the torques that permit to the vehicle to change its attitude in term of pitch and yaw, while the actual design doesn't permit to control the roll motion, but this is not mandatory for the considered application.

$$\boldsymbol{M}_{m_{body}} = \boldsymbol{b_m} \times \boldsymbol{F}_{m_{body}} = \boldsymbol{b_m} \times (\boldsymbol{g}(q0, q1, q2, q3, q4)\boldsymbol{F_m})\boldsymbol{F_m} \tag{140}$$

Where $\boldsymbol{b_m}$ represents the vector that connect the CoG of the body, to the CoGm of the magnet. The fluidic forces are herein considered as the lift and drag forces described in the xy and xz planes of the vehicle, the torques generated by these, that are meant to be applied into the CoV of the vehicle, also in this case the forces need to be translated from the flow reference to the body reference frame, as usual for fluid interactions using the sideslip angle β and the angle of attack α, through the rotation matrices $\boldsymbol{R}(\beta), \boldsymbol{R}(\alpha)$:

$$\begin{aligned} \boldsymbol{F_{fluidic_{body}}} &= \boldsymbol{R}(\beta)\left[-F_{drag_{\boldsymbol{xy}}}(\beta); -F_{lift_{\boldsymbol{xy}}}(\beta); 0\right]^T + \boldsymbol{R}(\alpha)\left[-F_{drag_{\boldsymbol{xz}}}(\alpha); 0; -F_{lift_{\boldsymbol{xz}}}(\alpha)\right]^T \\ \boldsymbol{M_{fluidic_{body}}} &= [x_{CoV}; 0; 0] \times \boldsymbol{F_{fluidic_{body}}} + \left[M_{roll}, M_{pitch}, M_{yaw}\right]^T \end{aligned} \tag{141}$$

$\boldsymbol{F_{fluidic_{body}}}$ represents the fluid actions on the vehicle, these are generated by the lift $F_{lift_{\boldsymbol{xy}}}(\beta), F_{lift_{\boldsymbol{xz}}}(\alpha)$ and drag $F_{drag_{\boldsymbol{xy}}}(\beta), F_{drag_{\boldsymbol{xz}}}(\alpha)$ forces, acting in the $\boldsymbol{x-y}$ and $\boldsymbol{x-z}$ planes. These depend of the sideslip and attack angles of the vehicle through the lift and drag coefficients and through the projection of the cross-section area normal to the fluid relative flow:

$$\begin{aligned} F_{lift_{\boxtimes}}(\boxtimes) &= \frac{1}{2} C_{lift_{\boxtimes}}(\boxtimes) \rho_{fluid} A_{\boxtimes}(\boxtimes) V_{\boxtimes}^2 \\ F_{drag_{\boxtimes}}(\beta) &= \frac{1}{2} C_{drag_{\boxtimes}}(\boxtimes) \rho_{fluid} A_{\boxtimes}(\boxtimes) V_{\boxtimes}^2 \\ A_{\boxtimes}(\boxtimes) &= A_{transv} + \frac{(A_{lat} - A_{transv})}{2} - \frac{(A_{lat} - A_{transv})}{2} \cos(2\,\boxtimes) \end{aligned} \tag{142}$$

Where $\boxtimes$ refers to the considered plane and therefore the considered relative flow angle with respect to the vehicle body reference frame, i.e. $\boxtimes = [(\boldsymbol{x-y}, \beta), (\boldsymbol{x-z}, \alpha)]$. The fluid interaction coefficients for the considered vehicle are those provided by [100], $[M_{roll}, M_{pitch}, M_{yaw}]$ represent the three torques generated by the rotational motion of the vehicle. The gravity action is defined in the fixed frame and needs to be converted into the body frame using the transformation $\boldsymbol{g}(q0, q1, q2, q3, q4)$ already used for the magnetic forces:

$$\boldsymbol{F_{gravity_{body}}} = \boldsymbol{g}(q0, q1, q2, q3, q4)[0; 0; Mg]^T \tag{143}$$

With M mass of the vehicle and g the gravitational acceleration. Since the Z axis is pointing downward the gravity force in the fixed frame is positive. Finally, the buoyancy force, also in this case it is possible to define it in the fixed reference frame and then use $\boldsymbol{g}(q0, q1, q2, q3, q4)$ convert it into the body reference:

$$\boldsymbol{F_{buoyany_{body}}} = \boldsymbol{g}(q0, q1, q2, q3, q4)\left[0; 0; -\rho_{fluid} V_{vehicle} g\right]^T \tag{144}$$

Where ρ_{fluid} represent the density of the considered fluid and $V_{vehicle}$ is the volume of the vehicle. Since this force in not applied to the CoG of the vehicle it'll cause a torque that can be expressed through the vector that connects the CoG to the CoV of the vehicle:

$$\boldsymbol{M_{buoyany_{body}}} = [x_{CoV}; 0; 0] \times \boldsymbol{F_{buoyany_{body}}} \tag{145}$$

With x_{CoV} distance of the CoV from the CoG of the vehicle, along the x axis. The equation of motion can now be written as:

$$\boldsymbol{M\dot{\nu}} + \boldsymbol{C_{coriolis}(\nu)\nu} = [\boldsymbol{F_{fluidic_{body}}} + \boldsymbol{F_{gravity_{body}}} + \boldsymbol{F_{buoyany_{body}}} + \boldsymbol{F_{m_{body}}}; \boldsymbol{M_{fluidic_{body}}} + \boldsymbol{M_{buoyany_{body}}} + \boldsymbol{M_{m_{body}}}] \tag{146}$$

With $\boldsymbol{M}$ inertia matrix, $\boldsymbol{C_{coriolis}(\nu)\nu}$ term that takes into the account the Coriolis actions on vehicle and $\boldsymbol{\nu} = [u; v; w; p; q; r]$. The system absolute velocity and rate of change of orientation is eventually described as follows:

$$\begin{aligned}\left[\dot{X};\dot{Y};\dot{Z}\right] &= \boldsymbol{g}(q0,q1,q2,q3,q4)^T[u,v,w]^T \\ \left[q\dot{0},q\dot{1},q\dot{2},q\dot{3},q\dot{4}\right]^{\boldsymbol{T}} &= 0.5\boldsymbol{s}(p,q,r)[q0,q1,q2,q3,q4]^T\end{aligned} \tag{147}$$

6.4 FLOP control formulation

The model dynamic is described by a full 6d.o.f rigid body motion set of differential equations, plus the terms that describe the position and the attitude of the vehicle into the fixed reference frame. Since the control actuation, comes from coils fixed into the world reference frame, the actuation provided by these, needs to be translated into the body reference frame, through a quaternion transformation. Thus, the system dynamic can be described as:

$$\dot{\boldsymbol{x}} = \boldsymbol{\phi}(\boldsymbol{x}) + \boldsymbol{h}(\boldsymbol{x})\boldsymbol{u} \tag{148}$$

Where $\boldsymbol{h}(\boldsymbol{x})$ represent the transformation from fixed reference frame to body reference frame, while $\boldsymbol{u} = \boldsymbol{F_X}, \boldsymbol{F_Y}, \boldsymbol{F_Z}$ is the vector that contains the forces generated by the gradients, into the three directions of the fixed reference frame. To apply the FLOP formulation a linearization is required, so the term $\boldsymbol{h}(\boldsymbol{x})\boldsymbol{u}$ can be rewritten through a Taylor series expansion centered into $\bar{\boldsymbol{x}}, \bar{\boldsymbol{u}}$:

$$\boldsymbol{h}(\boldsymbol{x})\boldsymbol{u} = \boldsymbol{h}(\bar{\boldsymbol{x}})\bar{\boldsymbol{u}} + \nabla_{\boldsymbol{x}}(\boldsymbol{h}(\boldsymbol{x})\boldsymbol{u})|_{\bar{\boldsymbol{x}},\bar{\boldsymbol{u}}}(\boldsymbol{x}-\bar{\boldsymbol{x}}) + \nabla_{\boldsymbol{u}}(\boldsymbol{h}(\boldsymbol{x})\boldsymbol{u})|_{\bar{\boldsymbol{x}},\bar{\boldsymbol{u}}}(\boldsymbol{u}-\bar{\boldsymbol{u}}) = \boldsymbol{h}(\bar{\boldsymbol{x}})\bar{\boldsymbol{u}} + \nabla_{\boldsymbol{x}}\big(\boldsymbol{h}(\boldsymbol{x})\big)\bar{\boldsymbol{u}}|_{\bar{\boldsymbol{x}},\bar{\boldsymbol{u}}}(\boldsymbol{x}-\bar{\boldsymbol{x}}) + \boldsymbol{h}(\bar{\boldsymbol{x}})(\boldsymbol{u}-\bar{\boldsymbol{u}}) \tag{149}$$

This can be easily written calling $\boldsymbol{C} = \boldsymbol{h}(\bar{\boldsymbol{x}})\bar{\boldsymbol{u}} - \nabla_{\boldsymbol{x}}\big(\boldsymbol{h}(\boldsymbol{x})\big)\bar{\boldsymbol{u}}|_{\bar{\boldsymbol{x}},\bar{\boldsymbol{u}}}\bar{\boldsymbol{x}} - \boldsymbol{h}(\bar{\boldsymbol{x}})\bar{\boldsymbol{u}}$, $\boldsymbol{A} = \nabla_{\boldsymbol{x}}\big(\boldsymbol{h}(\boldsymbol{x})\big)\bar{\boldsymbol{u}}|_{\bar{\boldsymbol{x}},\bar{\boldsymbol{u}}}$ and $\bar{\boldsymbol{B}} = \boldsymbol{h}(\bar{\boldsymbol{x}})$, this leads to the following system:

$$\dot{\boldsymbol{x}} = \boldsymbol{\phi}(\boldsymbol{x}) + \bar{\boldsymbol{A}}\boldsymbol{x} + \bar{\boldsymbol{B}}\boldsymbol{u} + \boldsymbol{C} \tag{150}$$

Where $\bar{\boldsymbol{A}}, \bar{\boldsymbol{B}}$ are going to be updated at each step of the simulation or might be linearized around a specific point $\bar{\boldsymbol{x}}$. The considered system, results to be underactuated, in fact a lack of controllability is exhibited by it, with a degree of controllability that depends on the actual state of the vehicle. This behavior is justified by unobservability of the roll angle as well as its rate and by the strong coupled effects on position and rotation due to the control forces applied to the vehicle, in fact once a force on the y *or* z axis of the vehicle reference system is applied, it affects the sway and yaw motions or heave and pitch motion respectively. The evaluation of the controllability can be done applying the following:

$$Controllability = rank([\boldsymbol{B}\ \boldsymbol{AB}\ \boldsymbol{A^2B}\ \ldots \boldsymbol{A^{n-1}B}\ ]) \tag{151}$$

With n dimension of the state $\boldsymbol{x}$ of the system. For instance, considering the formulation of the dynamic equation through Euler angles, if the system is linearized in the following conditions is evident the lack of controllability:

$$\bar{\boldsymbol{x}} = [\bar{X}, \bar{Y}, -\bar{Z}, 0,0,0,0,0,0,0,0,0]^T \ => \ Controllability = 8$$

$$\bar{\boldsymbol{x}} = [\bar{X}, \bar{Y}, -\bar{Z}, 0,0,0,0.01,0,0,0,0,0]^T \Rightarrow \ Controllability = 10$$

The first case refers to the vehicle in steady state in the $\bar{X}, \bar{Y}$ position floating at the height $-\bar{Z}$, the controllability analysis produces 8 out of 12, meaning that in steady state the Euler angles and the roll rate are not controllable through the magnetic gradients. The second case refers to the vehicle placed in the same position, but while moving with longitudinal speed component, here the controllability test provide 10 out of 12, which means that vehicle is now able to control its pitch and yaw angles as well as its lateral and vertical motion, but it is still unable to control the roll angle and the roll rate, as expected. This last result supports the assertion that using a proper designed trajectory, an ideally built robot, can achieve the final desired position as well as the desired attitude in terms of pitch and yaw angles.

6.5 Experimental setup.

6.5.1 Robot design and build.

The two robot types SSND and SFNU, were fabricated and tested experimentally, these robots are made out of four parts: a spherical magnet, main body, mass balance module, and the cap, as shown in Fig. 72. The permanent magnet (HKCM Engineering e.K.) is a 1-mm diameter NdFeB sphere with a magnetization strength of 0.5 emu.

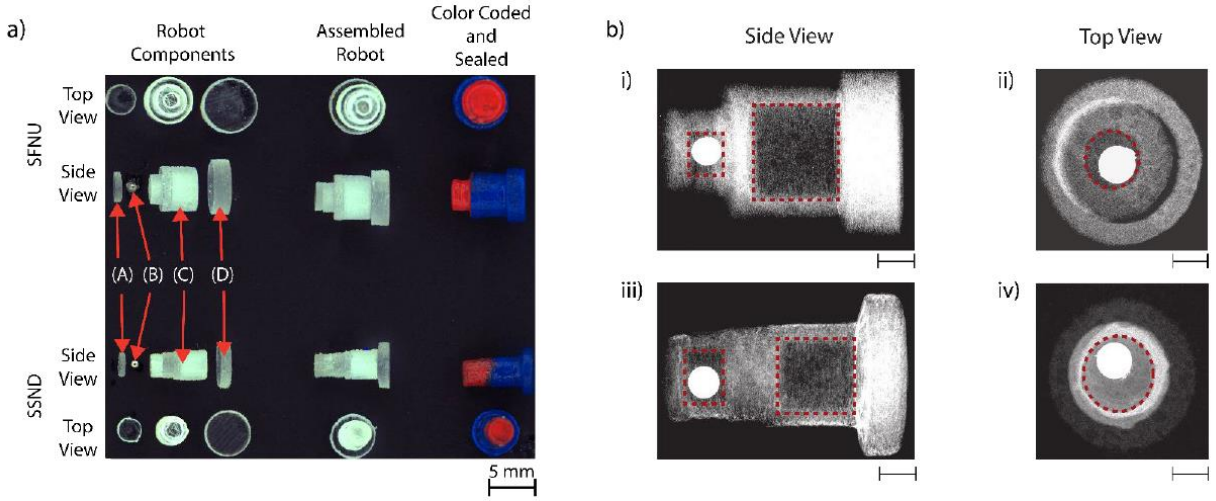

Figure 72: (a) SFNU and SSND type of robot designs consist of four main components: (A) is the magnet cap, (B) is the spherical NdFeB permanent magnet.

Both robot designs are constituted by three main elements: a magnetic actuation cavity where the magnet is placed, an air cavity for density tuning, and a mass-balance part for COM-COV tuning. The robot type, i.e. SFNU-type or an SSND-type, depends on the proper choice of the sizes of these elements. Moreover, the overall design of the robots is meant to be axisymmetric along the major axis of the vehicle, this permits to have equal fluidic interactions regardless the roll angle of the robot. This will improve the performance of the controlled system and will generate an easier and more reliable vehicle's dynamic while moving in a dynamic flow.
The built procedure is common for both robot designs, and requires the following steps, the main body, mass balance module, and the cap are 3D printed in100% VeroClear material with matte option, using a Connex 260 3D printer. These parts are then sonicated in 1 M NaOH bath for 4 hours to

remove fine support residuals. After that, the 3D-printed parts are washed with water and dried for 1 hour under a warm air flow (40°C). After inserting the permanent magnet into its cavity, the separated parts are glued together using cyanoacrylate adhesives. The robot sealing is achieved using a clear lacquer dip coating (Plastik 70, clear lacquer, 74327), the robot is dived for 0.5 s. To reduce the image processing effort while tracking the robot position and orientation, the robot is painted considering a color coding that assign Edding 260 red on the magnetic end and blue on the nonmagnetic end. Then a second layer of clear lacquer is applied by diving again the robot for 0.5 s this process adds a coating sheet on top of the coloring process. After every coating process, the robot is left to dry at room temperature for 2 hours.

Due to the manual manufacturing steps some iterations have been done to determine empirically the best tuning for both SFNU and SSND designs, in fact, the overall density of the robot may vary slightly, because of the imperfections that may occur during the various steps. An experimental characterization is performed over 20 robots, this helps to evaluate the mean mass of the manufactured robots. This result in an average mass of 145.09 mg with a ±1.27 mg standard mass deviation for the SFNU and 71.57 mg with and ±0.44 mg standard mass deviation for SSND robots. The yield rate is around 75% for the aforementioned manufacturing technique. Moreover, the characterization highlighted that the major mass variation stems from the mass balance module, the main body module, and color-coding and lacquer coating with the highest mass variation of 0.84 mg for the main body module of SFNU-type of robot. The mean mass and mass deviations of each manufactured component are reported in the following table:

SFNU	Value	Deviations
Magnet	4.079 [mg]	0.063
Magnet cap	7.232 [mg]	0.104
Main body	59.816 [mg]	0.845
Mass balance module	61.942 [mg]	0.341
Cyanoacrylate	1.528 [mg]	0.423
Color coding lacquer coating	10.489 [mg]	0.530
SSND	Value	Deviations
Magnet	4.036 [mg]	0.051
Magnet cap	3.942 [mg]	0.066
Main body	27.976 [mg]	0.291
Mass balance module	25.976 [mg]	0.331
Cyanoacrylate	0.553 [mg]	0.051
Color coding lacquer coating	9.088 [mg]	0.488

Table 7: SFNU and SSND components masses

The density values of VeroClear material and the bead magnet are measured and used for the marginally balanced robot design. Throughout the various robot shapes that satisfy the previously explained design constraints, the final shape of the robot is chosen to ease the manufacturing and assembly of the robot. To proper select the mass, volume, and COM and COV positions an iterative process is performed done by tuning the length and diameter parameters of upper body, main body, and mass-balance module within the range of 50 to 100 micrometers at each iteration.

The scope of the iterative process on the upper body and on the mass-balance module was to fine locate the position of the CoM and of the CoV, moreover the main body design is defined to tune the air gap module to properly set the density of the robot.
The COM positions are measured by supporting the two ends of the robot and measuring the length and reaction load at one of the two ends. The average COM positions are 4.58 ± 0.06 mm and 4.79 ± 0.07 mm (error reported as standard deviation) for SFNU- and SSND-type robots, respectively. This information is fed to the controller to improve its performance while guiding the vehicle.
Fig. 73 illustrates the robot dimensions that characterize its design, their values both with other major parameters of the robots are reported in table 7.

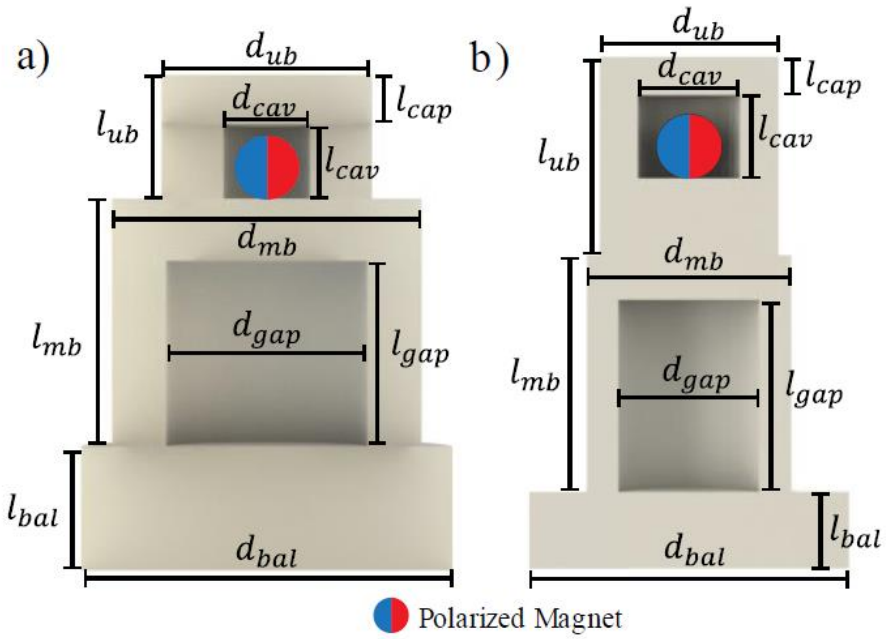

Figure 73: Cross-section view CAD models, with the parametric design dimensions. (a) represents the design for SFNU type of robot, and (b) represents the design for SSND type of robot.

Symbol	Quantity	SFNU	SSND
d_{ub}	Upper body diameter	3.4 [mm]	2.8 [mm]
l_{ub}	Upper body length	2 [mm]	3.1 [mm]
d_{mb}	Main body diameter	5 [mm]	3.2 [mm]
l_{mb}	Main body length	4 [mm]	3.7 [mm]
d_{bal}	Mass balance diameter	6 [mm]	5 [mm]

l_{bal}	Mass balance length	2 [mm]	1.2 [mm]
l_{cap}	Cap length	0.8 [mm]	0.6 [mm]
d_{gap}	Air gap diameter	3.25 [mm]	2.21 [mm]
l_{gap}	Air gap length	3 [mm]	3 [mm]
d_{cav}	Magnet cavity diameter	1.4 [mm]	1.6 [mm]
l_{cav}	Magnet cavity length	1.2 [mm]	1.3 [mm]
m	Total mass	0.1383 [g]	0.0667 [g]
V_r	Total volume	153.25 $[mm^3]$	72.41 $[mm^3]$
σ_r	Density	902 $[kg/m^3]$	921 $[kg/m^3]$
p_{com}	CoM location	4.76 [mm]	4.73 [mm]
p_{cov}	CoV location	4.55 [mm]	4.85 [mm]

Table 8: SFNU and SSND dimensions

6.5.2 Magnetic actuation system.

The target of the experimental activity is to recreate the typical environment inside an MRI machine, including the constant unidirectional field $\boldsymbol{B0}$ and the magnetic gradients, that are actuated accordingly to FLOP control algorithm, and used to move and turn the robot within the fluid.
The system is made out of three main parts as shown in Fig. 74:

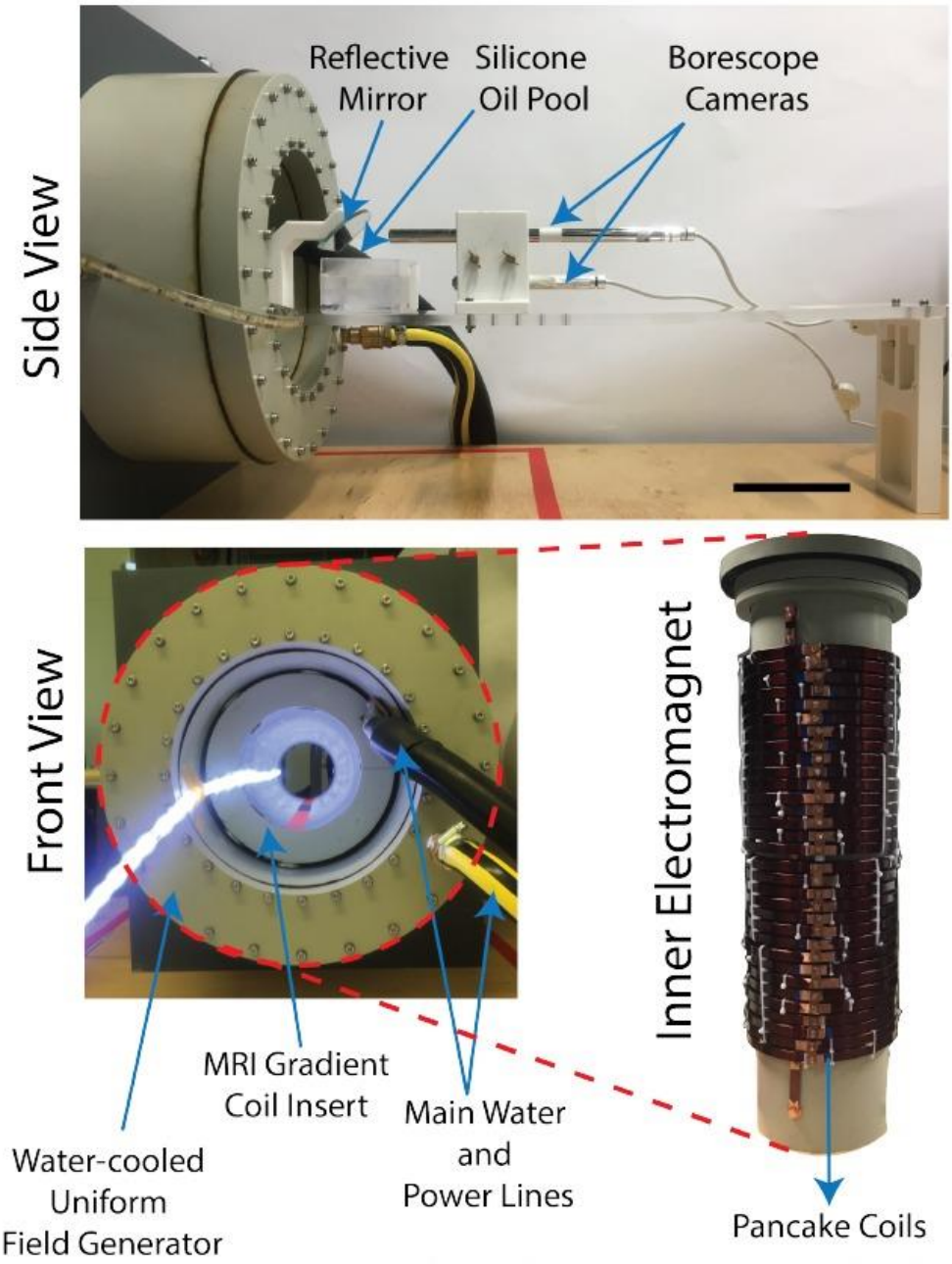

Figure 74: The pseudo-MRI experimental setup consists of a custom-built, water-cooled uniform field generator using pancake coils, and the pool filled with silicone oil, in which the robot moves

- a commercial MRI gradient coil insert,
- a uniform field generator, and
- an experimental stage.

The computer input is fed to the gradient coil insert that generates the magnetic field gradients inside the MRI. The MRI gradient coil insert (BioSpec® B-GA12SL, Bruker) can generate 200 mT/m maximum instantaneous magnetic field gradients and can provide 66 mT/m maximum magnetic field gradient continuously. The maximum continuous magnetic pulling force that can be exerted on the robot with the MRI gradient coil unit is 36 μN.

The uniform constant field $\boldsymbol{B0}$, is generated by a custom-built electromagnet placed around the MRI device to generate the environment common to the MRI device.
The mean value of the magnetic field $\boldsymbol{B0}$ generated by this device in the considered workspace is 31.19 mT, this means that it is strong enough to align the magnetic axis of the permanent magnet placed inside the robot to the *x*-axis.
The field uniformity is 0.73% around the workspace, and the worst-case gradients generated are less than 10% of the maximum continuous gradient strength of the MRI gradient coil insert. The experimental stage insert includes two borescope cameras (ViTiny UM07, eheV1-USBpro), two mirrors, and a 5 x 5 x 3 cm3 experimental silicone oil pool.
The pool and the cameras are mounted on a sliding sledge that locate them at the center of the MRI gradient coil insert unit, where a proper spatial uniformity of the magnetic field gradients is guaranteed. The density of the silicone oil used in experiments is approximately 1000 kg/m3, and the viscosity is 100 cSt. The data regarding the vehicle state coming out from the cameras, as well as the control actions are recorded by the computer.
The digital camera feedback of the two borescope cameras is used rather than MR imaging, these give feedback of the top and side view of the pool, and hence position and orientation of the robot in the horizontal and vertical planes. The color coding is used to detect precisely the position and orientation of the robot. Image processing algorithms are used to extract the 3D position and orientation of the capsule for measurement of experimental results and as input to the FLOP control to generate the control actions. The update rate of the magnetic field gradients is fixed at 10 Hz, which is achievable for an MRI-powered system that do use MR imaging for feedback [24, 25]. Image processing and control loop computations are done by the external master computer and the desired control inputs are sent to the MRI gradient coil insert via an Ethernet connection.

6.5.3 Response of the system to magnetic actuation.

To improve the overall performance of the controlled systems, and to properly tune the parameter of the model provided to the controller, an experimental campaign has been done, this is aimed to characterize the behavior of the robot when specific magnetic pulses are applied.
A rotating magnetic pulling force is applied to the tip of the vehicle to understand the limit of its performance during rotation. When this force is applied, the coupling of the rotation and translation dynamics, make the vehicle perform a circular trajectory.
This campaign analyzes the rotational speed of the robot when open-loop actuation inputs with different strengths and different frequencies are applied.
The results is that the system exhibits an upper limit, in fact when the frequency of the input become too high the robot is no more able to track the circular trajectory in phase with the rotating input. This frequency is referred to as the step-out frequency [36].
This open-loop, continuously rotating magnetic gradients are applied with strengths of 20, 30, and 40 mT/m, and different frequencies of rotation as well. The open-loop pulling force can be described by:

$$\boldsymbol{F}_m = F_m \begin{bmatrix} \cos(2\pi f_0 + \phi_0) \\ \sin(2\pi f_0 + \phi_0) \\ F_{\frac{balance}{F_m}} \end{bmatrix} \tag{152}$$

where $\boldsymbol{F}_m$ is the open-loop magnetic actuation signal, ϕ_0 is the initial orientation of the robot, which determined through image processing, $f_0$is the frequency of the input signal, and t is the actuation time. In order to determine the step-out frequency, a frequency sweep from 0.01 Hz to 0.2 Hz with step sizes of 0.02 Hz is performed. After determining a rough estimate of the step-out frequency, f_0, experiments are then repeated with smaller step sizes (down to 0.005 Hz) to better estimate the step-out frequency. The condition of step-out is defined as the lowest frequency f_0 for which the robot's observed rotational frequency was below of the input frequency f_0 by at least 3%. The observed rotational frequency was calculated as taking a time average of the discretized rotational velocity.
These rotation experiments are conducted in both horizontal $X-Y$ plane and vertical $X-Z$ plane. To balance the position of the robot along the Z axis, a weight/buoyancy compensation force, $F_{balance}$l, needs to be applied. Therefore, pulling force $\boldsymbol{F}_m$ is superposed to this last. Each experiment is repeated 5 times with 5 replicas of each type of robot. The experiment time is set to be the time at which five complete rotations of the circular inputs are complete, or anyway the time at which the robot accidentally hits one of the boundaries of the experimental pool.
The model parameters for the simulators and for the controlled are then determined accordingly to these results, by applying the same procedure.

6.6 Experimental results

6.6.1 introduction to the experimental activity

The FLOP control was applied to the MRI setup, the goal of the experimental activity was to demonstrate that position and orientation of the micro magnetic robot can be controlled even though the dynamic system presents some limitations due to the overall experimental setup, in fact the considered robot exhibits coupled translation and rotation dynamics. This results in a system that cannot easily reach any desired pose even though a model-based sub optimal control is applied, in fact this class of controllers rely on the minimization of the error described through the hyperplane represented by all the elements of the state that have to be controlled. The target for the MRI controlled vehicle is to successfully manage 3D position and 2 Euler angles, since the roll cannot be observed by the experimental setup, i.e. 5 elements (7 when orientation is described through quaternion) of the state have to reach some reference values.
Direct request of minimization of the whole state error might end up into a local minimum of the hyperplane, causing an approximated final pose of the vehicle, that might be far from the desired one. For this reason, and considering the limited maneuverability of the vehicle, especially when the natural static displacement of it is non-neutral due to manufacturing imperfections, a trajectory that properly guides the controlled vehicle toward the desired final configuration is required. The state of the robot is computed with visual feedback from two cameras that observe the workspace from top and side view.
Two different tests were performed, in the first case the activity is carried out considering 9 waypoints where the vehicle has to pass through, they are also arranged to provide a final desired orientation for the vehicle, the aim of this part of the investigation is to understand the ability of the vehicle to pass through waypoints and to understand if a properly designed trajectory can guide the vehicle to reach the desired orientation, by the way to generalize the results obtained with this test a proper technique to define the reference trajectory is required, as will be shown in the second part of the experimental activity.
In the second test a Bezier based trajectories were used, these technique permits to define smoother trajectories, with a higher density of waypoints, this approach will guarantee more robustness of the controlled system and will provide more general results.

6.6.2 experimental test with waypoints

The aim of this experimental activity was to achieve the final pose described in the following table, the trajectory was designed fixing 9 waypoints, in terms of position and orientation.

Position	Value	Orientation	Value
X	0.0103 [m]	Roll	N/A [°]
Y	-0.0351 [m]	Pitch	61 [°]
Z	-0.0088 [m]	Yaw	211 [°]

Table 9: target point and desired orientation

Two experimental tests were carried out, starting from two different position and orientation, as described in the following table:

Position	Value	Orientation	Value
X1	0.0185 [m]	Roll1	N/A [°]
Y1	-0.0324 [m]	Pitch1	88.7 [°]
Z1	-0.0043 [m]	Yaw1	42.8 [°]
X2	0.0103 [m]	Roll2	N/A [°]
Y2	-0.0351 [m]	Pitch2	61 [°]
Z2	-0.0088 [m]	Yaw2	202 [°]

Table 10: Initial conditions

Fig. 75 shows the experimental results in terms of accuracy in tracking the desired trajectory. In both tests the vehicle started from the points indicated by the green triangles, the yellow arrows indicate the sense in which the robot moves along the path, the red dots indicate the reference trajectory waypoints, and the arrival point is indicated with a red dotted cross.

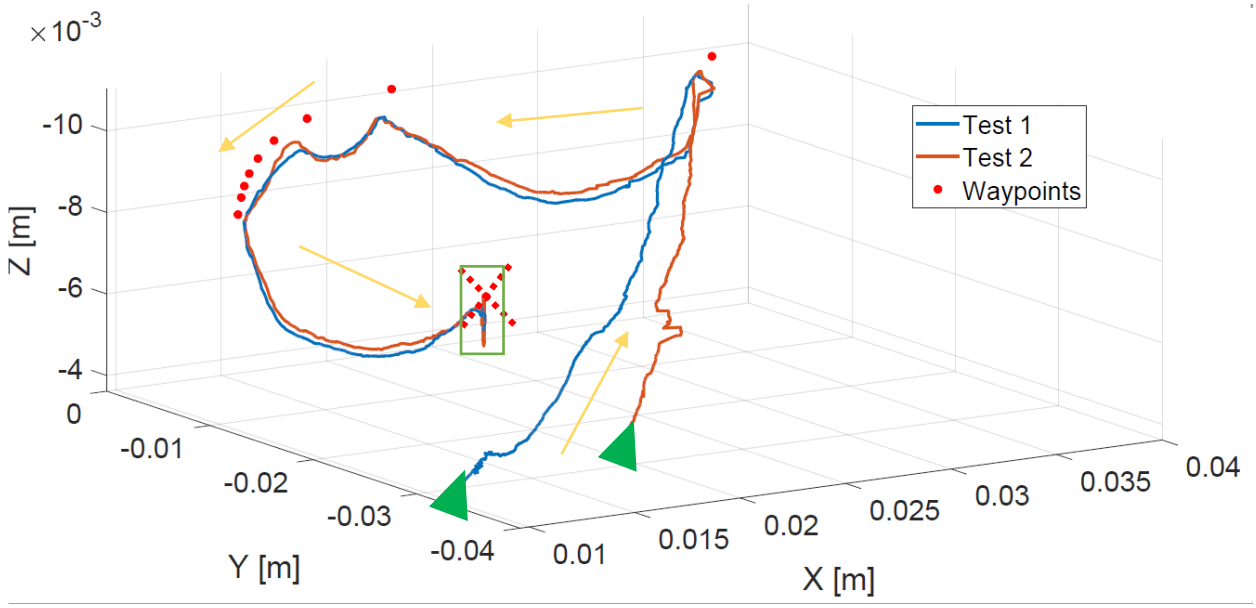

Figure 75: experimental test, performed using few waypoints.

Regarding the accuracy in tracking the trajectory's waypoints, the major misplacement of the vehicle was around 1mm. It's evident the repeatability of the desired trajectory, even starting from different initial condition, in fact the trajectory performed by the vehicle during the second test exhibits only some small deviations from the first trajectory, while tracking the desired waypoints, this support the robustness of the controlled system.
For what regards the orientation, Fig. 76 illustrates the evolution of the yaw and pitch angles during the motion along the reference trajectory, as already stated the goal is represented by reaching the desired final orientation as well as the desired position.
In Figure 76 the blue solid lines represent the results referring to the test 1 while the yellow solid lines refer to the test 2, the red solid line represents the final desired values for yaw and pitch angles. Yaw angle got close to the desired value, with a discrepancy of about 8 [°], the discrepancy is mostly due to error in the measurements, parameters uncertainties for the model provided to the controller and imperfections of the vehicle that causes instability in pitch, that also affect yaw angle.

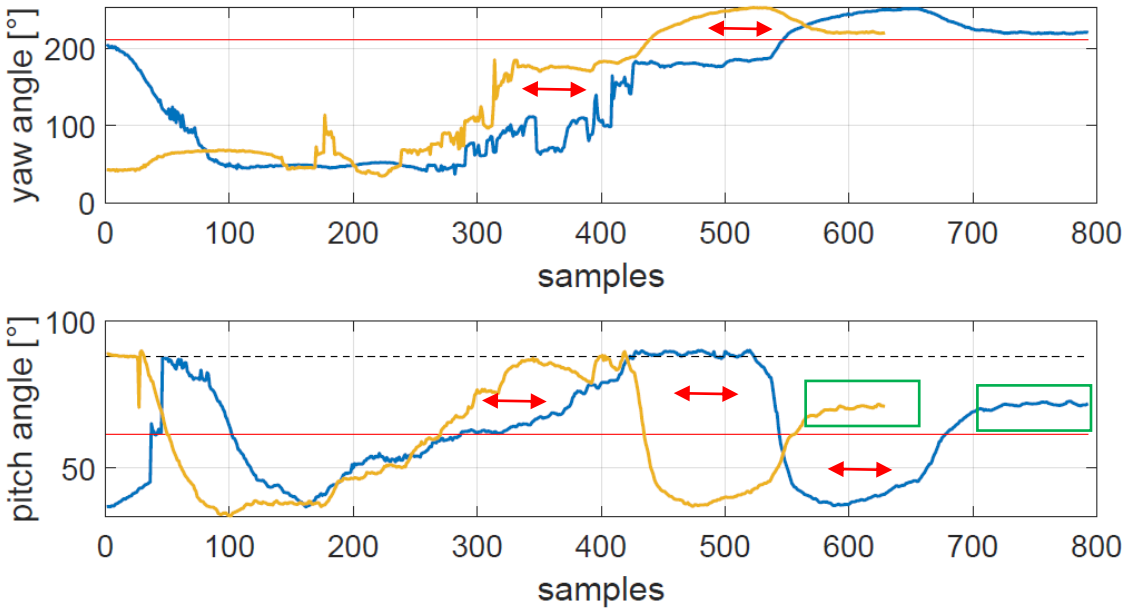

Figure 76: Yaw and Pitch angle evolution.

For the pitch angle, the vehicle exhibits in both tests a misalignment of roughly 9 [°], in this case the major reason of the tracking error, is related to the imperfections in the manufacturing process, in fact a misplacement and or a misalignment of the center of buoyancy with respect to the center of gravity and to the longitudinal axis of the vehicle, results into a non-neutral pitched configuration of the vehicle while in steady state, as shown by the black dotted line in figure 2, that indicates that the preferred pitch angle is about 88 [°], for the considered robot, fluid, and temperature. These added to the coupling of the rotational and translational dynamics of the vehicle, and with the natural tendency of the robot to sink, cause a trade off in reaching the desired height and the desired orientation in terms of pitch angle, this is also shown in the green rectangles in figure 1 and 2, where some small height and pitch oscillations are observed, these are also due to pulsing actuations to control the vehicle, and to fluctuations in state measurements that generate variations in the jacobians involved in the controller algorithm and hence create fluctuations of the provided control actions. These findings suggest that an ideally build robot can definitely track position and desired final attitude, with only some small errors due to noise in the measurements.

Finally, it's interesting to notice the robustness of the controlled system as well as the repeatability of the experiments, these are supported, by the evolution of the yaw and pitch angles during the motion, in Fig. 74, the double-headed red arrows indicate how the profiles exhibits a similar behavior only translated in time, the translation is caused by the different initial point and hence different overall time of acquisition. Beside this shifting the profiles are comparable.

6.6.3 path following of Bezier based trajectory

The experiments are conducted for both the robot types, SSND and SFNU. Four different tests are performed (1) linear path, (2-3) planar path in horizontal and vertical plane and (4) three-dimensional paths, the 2D and 3D path are designed using the Bezier technique, this provides smooth trajectories considering the initial orientation, in which the vehicle is meant to be and the final desired orientation that the vehicle should reach. Here the path-following capabilities are evaluated for both robots and the experimental results are presented in Fig. 77-78-79-80.
In the linear Fig. 77 case the SSND shows a final mismatch in the position of 2 mm below the reference trajectory accordingly to its sinking nature, with a misalignment of 0.17 [°] for the yaw angle and -2.45 [°] for the pitch angle. Similarly, the SFNU robots exhibits a 2.1 mm displacement error above the desired trajectory, due to its natural buoyant behavior, for the attitude this exhibits 5 [°] for the yaw angle and 2 [°] for the pitch angle respectively.

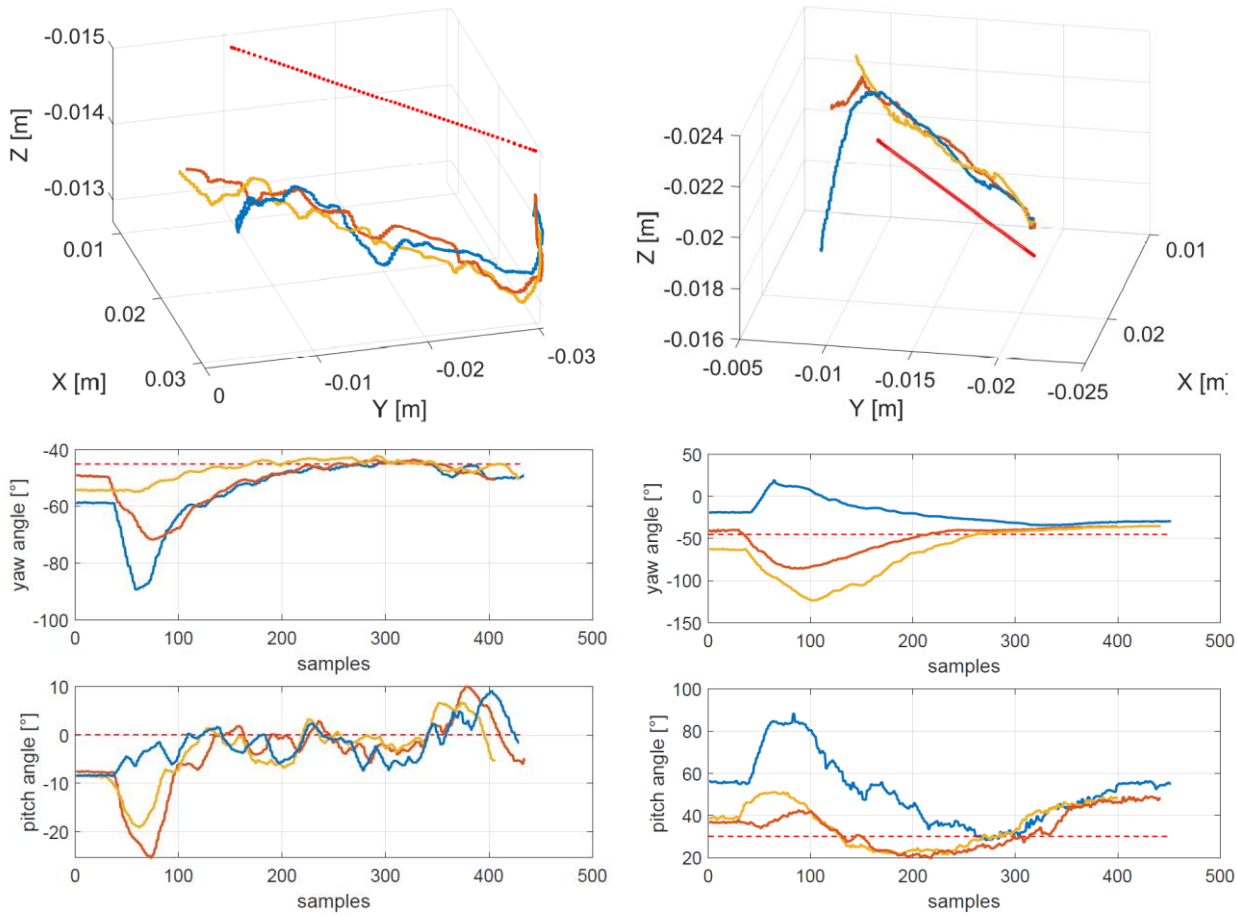

Figure 77: linear trajectory for SSND and SFNU, and attitude.

In the planar case Fig. 78 the SSND's position mismatch is 3.7 mm below the reference trajectory, with a misalignment of 21 [°] for the yaw angle and -2.26 [°] for the pitch angle. While the SFNU

robots shows 2 mm displacement mismatch above the desired trajectory, due to its natural buoyant behavior, for the attitude this exhibits 20.3 [°] for the yaw angle and 27.7 [°] for the pitch angle respectively.

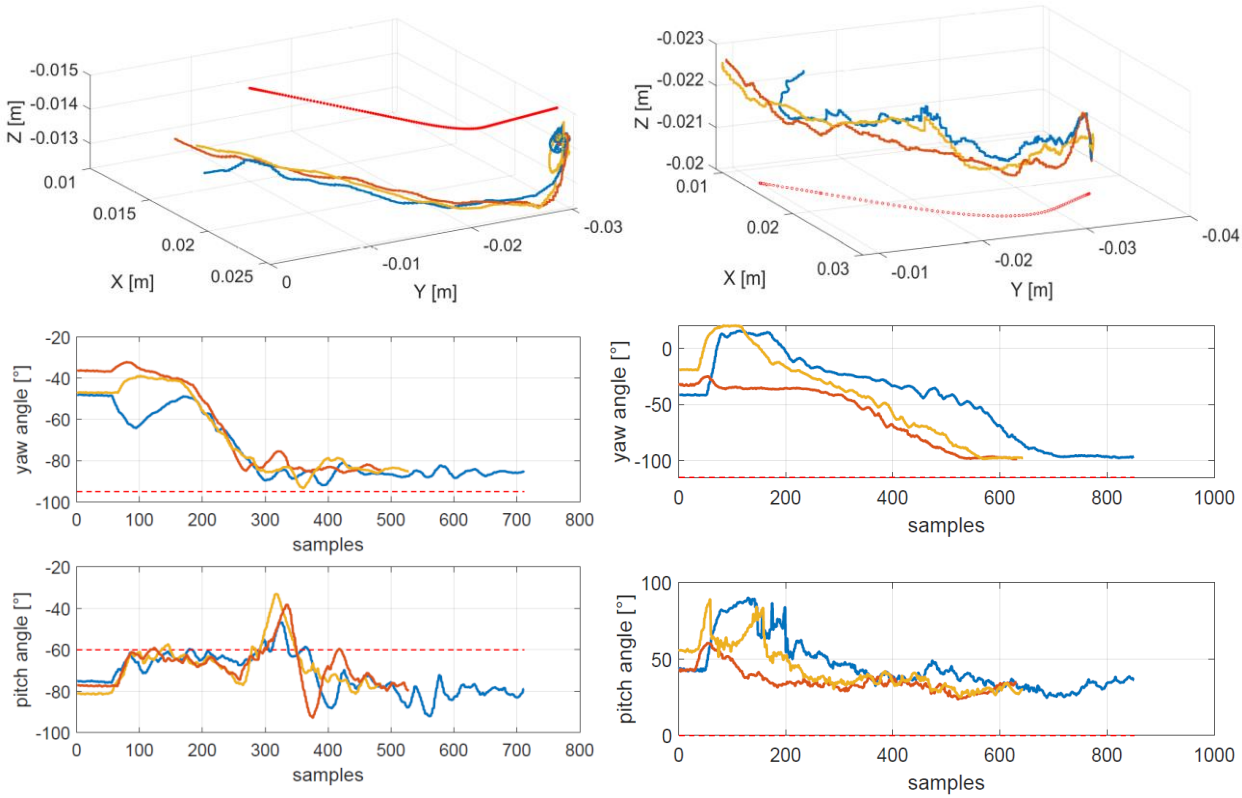

Figure 78: Planar trajectory for SSND and SFNU, and attitude.

In the vertical case Fig. 79the SSND position error is 2.66 mm below the reference trajectory, and a misalignment of −4.08 [°] for the yaw angle and 9.37 [°] for the pitch angle. While the SFNU robots shows 3 mm displacement mismatch above the desired trajectory, due to its natural buoyant behavior, for the attitude this exhibits 0.3 [°] for the yaw angle and 5.22 [°] for the pitch angle respectively.

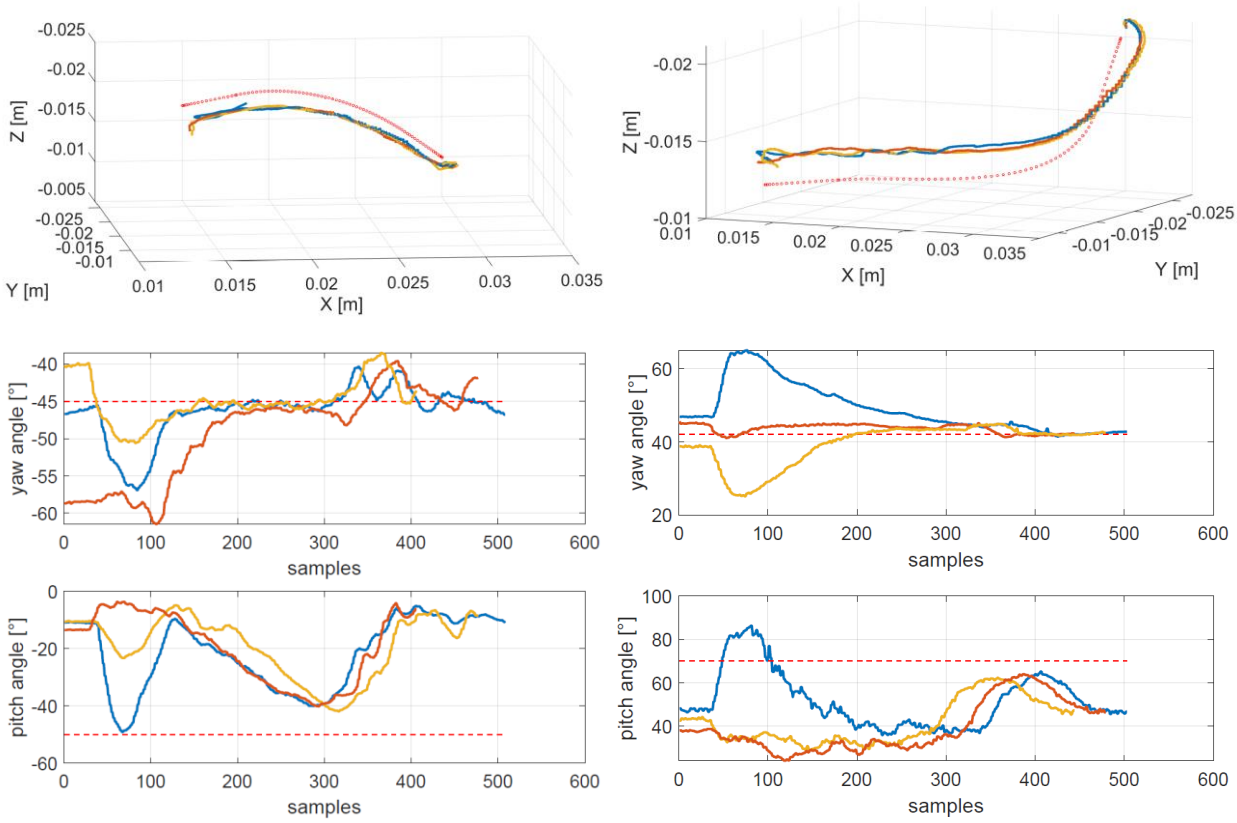

Figure 79: Vertical trajectory for SSND and SFNU, and attitude.

3D case shown in Fig. 80 the SSND position error is 2.73 mm below the reference trajectory, and a misalignment of 46.7 [°] for the yaw angle and −5.6 [°] for the pitch angle. While the SFNU robots shows 2 mm displacement mismatch above the desired trajectory, due to its natural buoyant behavior, for the attitude this exhibits 15.12 [°] for the yaw angle and 13.3 [°] for the pitch angle respectively.

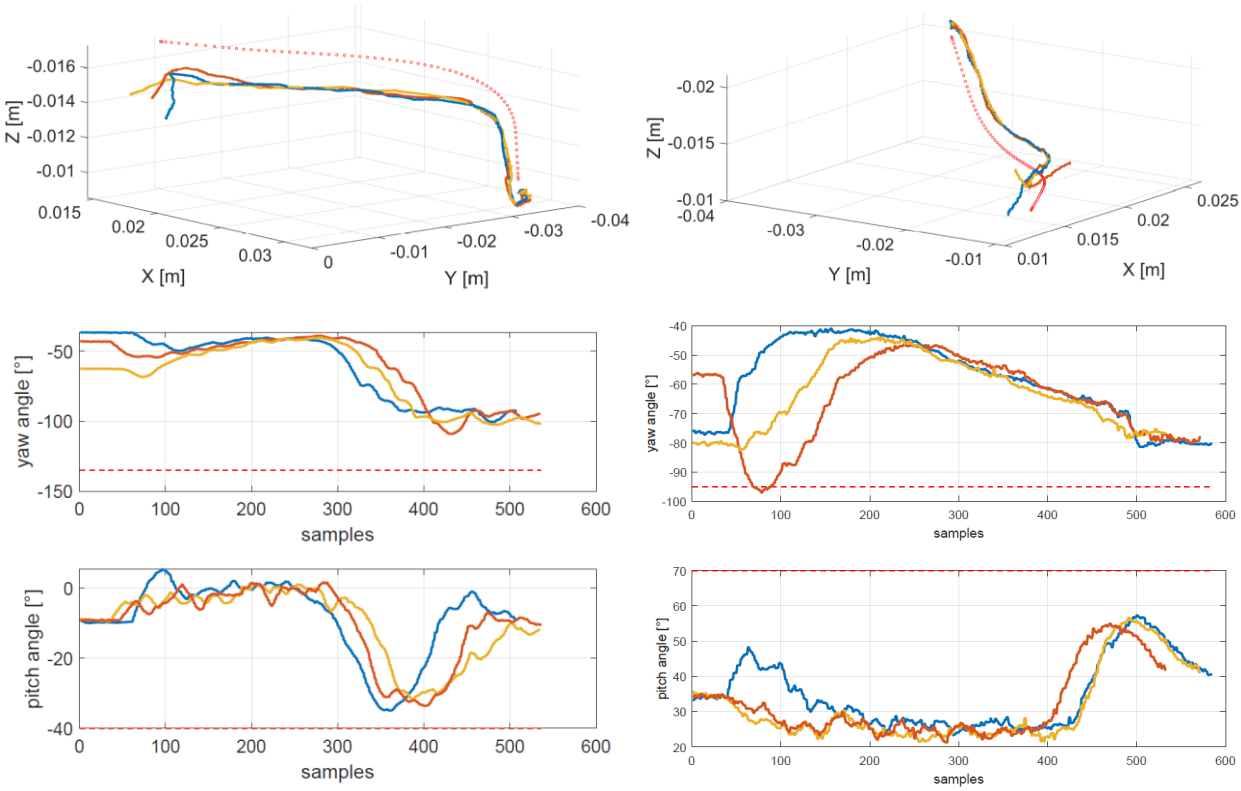

Figure 80: 3D trajectory for SSND and SFNU, and attitude.

Finally, in Fig. 81 some snapshots of the video of the activity are presented.

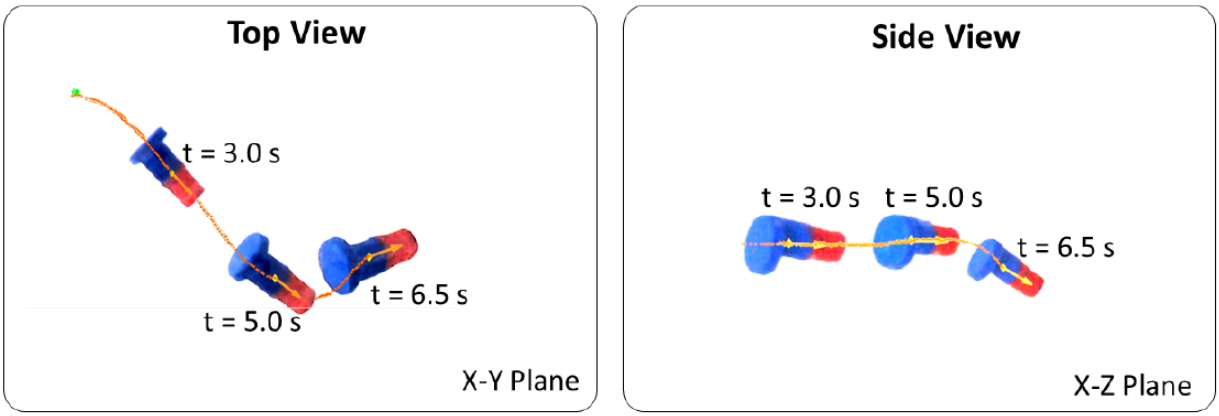

Figure 81: Experimental activity

The FLOP controller is here used for 5-DoF steering of MRI-powered untethered robots. The proposed controller was tested in the with trajectory defined by few waypoints and also with four different smooth paths generated with cubic Bezier technique. The considered setup uses a commercial MRI gradient coil insert. The proposed controller shows the ability to handle the nonlinear and underactuated dynamics, while tracking the smooth paths.
In the first scenario, the vehicle height varies throughout the trajectory due to the lack of waypoints, anyway the controller was able to track this trajectory and reach good performance also in reaching the final desired attitude.

The second part of the experimental campaign wants to investigate the performance in a more general set of cases to understand which the overall performance of the controlled system are, also in this case some mismatches are observed, but the technique supports the possibility to successfully control the 5 d.o.f motion of the vehicle.
The errors observed in the attitude of the vehicles are mostly due to manufacturing errors, that caused the mismatch between the CoM and the CoV locations.
In fact, this mismatch leads to discrepancy between the ideal and actual robot dynamic model, resulting in a natural tendency to assume a pitch angle, -10 [°]for the SSND robot, and 40 [°] degrees for the SFNU robot, when the these are placed stationary within the fluid.
Moreover, the sinking and floating design of the vehicles are responsible for the position mismatch in the vertical plane, since it's not possible to properly control the height of the vehicle independently from its pitch angle, because of the lack of controllability of the robots.
One chance to improve the controller performance is represented by the introduction of time-parametrized trajectories, which include velocity waypoints. These trajectories should consider the robot dynamics and actuation limitations.
Moreover, it has to be underlined that an actuation limitation was present, since the feedback rate used in this study is 10 Hz, which is a conservative choice, a higher feedback rate would potentially increase the controller performance, providing a controlled system capable to perform wilder and more challenging maneuvers.

Chapter 7

Thesis Conclusions

7.1 Conclusions

In this Ph.d. Thesis a new sub-optimal, model-based, feedback controller applied to nonlinear problems is presented. Classical method such Pontryagin's and Bellman's techniques exhibit the main drawback represented by an open-loop solution form. To overcome this issue, this work presents the FLOP method, a new technique which belongs to the family of VFC-Variational Feedback Control. FLOP succeeds to obtain a feedback control law by revisiting the optimality principle of the Pontryagin's method. A local optimality criterion is stated that, instead of optimizing the solution over the entire time interval of observation, uses a set of sub-optimal solutions each minimizing the objective function over a sub-interval of short time duration. The FLOP results, in general, differ from those obtained by the Pontryagin optimal principle.
The FLOP method is tested for different nonlinear dynamic cases to demonstrate the general strategy, also in underactuated cases, like the inverted pendulum and the MRI control of pills sized magnetic robots.
The FLOP method is an innovative approach for nonlinear dynamical system that shows interesting performances also allowing the addition, in the cost function, of some highly nonlinear functions with local effects on the dynamical system.
Moreover, the FLOP produces a new feedback control at low computational cost (when compared, for example, to MPC- Model Prediction Control) even for complex dynamical systems. The method can be applied to a large variety of engineering problems.
The FLOP technique was applied to the control of an autonomous car through emulated through a bike-model, this is part of a research project of the Mechatronic and Vehicle Dynamic Lab of Sapienza, aimed to realize an autonomous vehicle, starting from a production series city car.
Since the FLOP formulation provides the chance to add nonlinear penalty function in the cost function, so that different and simultaneous tasks can be achieved by the controlled system. In the case of the presented bike-model dynamical system, gaussian-like penalty functions are introduced to perform the obstacle avoidance and the carriage maintenance.
One of the main tasks for autonomous vehicle is the steering capabilities, therefore track performance optimization, and highspeed cornering capabilities were investigated and compared with classical LQR strategy. Comparison results are very promising, since the FLOP approach shows better performance respect to the LQR for all the tested velocities. In fact, for each given turning radius, the FLOP reaches higher velocities than the LQR approach. In the dynamical system, a list of emulated sensors was introduced, so that the FLOP driven vehicle is tested under different environmental conditions.
Then the collision avoidance performance was investigated, and the FLOP control proves to be successful when avoiding three different kind of collision with uncontrolled vehicles: (i) frontal collision, (ii) rear-end collision, and (iii) cross collision.
The control performance was also investigated in the case of a marine autonomous rescue vehicle, this vehicle is the result of a joint research industrial projects, given the complexity of the autonomous and rescue actions that it has to perform, a robust control ins needed, therefore the use of the FLOP represents a good chance to take into the account different tasks thanks to the ability to deal with different penalty functions and nonlinear dynamics.

One of the most challenging tests for the FLOP control is represented by the rocket vertical landing, in fact this controlled system, exhibits numerous and strong nonlinear dynamics, such as, aerodynamic actions, CoM motion within the rocket structure, forces generated by the actuators. The algorithm provided good performances in all the parts of flights and in the final landing, there results are also investigated in the presence of wind disturbance and confirmed the good capabilities of the proposed control technique.
Finally, the last test case presented in this thesis, is devoted to investigating the performance of the FLOP, when applied to 5-DoF steering of MRI-powered untethered robots. This research project is developed by The Max Planck Institute for Intelligent Systems (Stuttgart), and has the aim to create a micro magnetic untethered robot for medical applications.
The proposed controller guided the vehicle along various trajectories defined using the Bezier cubic lines, these are meant to bring the vehicle from the initial position and attitude to the final target position with the desired attitude.
The FLOP exhibited good performance in controlling two different types of robots, with misplacements and misalignment that are mostly caused by manufacturing errors.

Appendix A

A.1 MRI Magnetic action

The MRI device generates a uniform magnetic field $\boldsymbol{B}_0$ that aligns the magnet placed in the vehicle body. The action of the field acts on both sides of the magnet, i.e. N and S, generating a couple of forces, that lie on the same line of application, but with opposite sense. These generates a system where, the balances of the total forces acting in the horizontal and vertical directions, are zero, but the system results to be unbalanced in terms of rotation. In fact the system rotates until the field of the magnet is aligned to $\boldsymbol{B}_0$. Once the magnet is aligned, the total NET force, acting on the vehicle, due to the UNIFORM field $\boldsymbol{B}_0$, is zero, as well as the total torque since the opposite forces, acting on the two poles N/S of the magnet are now aligned, hence the lever arm $\boldsymbol{b}$ is zero. In this condition the only way to generate forces applied on the magnet, is introduce variation in space of the magnitude of the acting field, hence the field won't be UNIFORM anymore. This is performed, through the use of external coils that introduce local variation of the magnetic field, i.e. magnetic field gradients in space.

A.2 Magnetism

A charged object produces an electric field **E** which perturbates the space. In a similar manner, a bar magnet is a source of a magnetic field **B**. This can be demonstrated by moving a compass near the magnet. The compass needle will line up along the direction of the magnetic field produced by the magnet, as depicted in Fig. 82

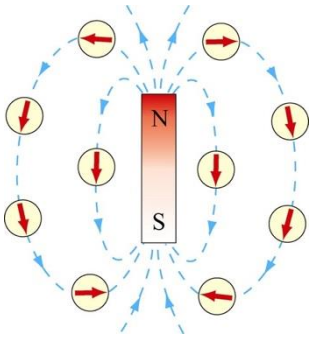

Figure 82: Magnetic field produced by a bar magnet

The bar magnet consists of two poles, which are designated as the north (N) and the south (S). Magnetic fields are strongest at the poles. The magnetic field lines leave from the north pole and enters the south pole. When holding two bar magnets close to each other, the like poles will repel each other while the opposite poles attract Fig. 83.

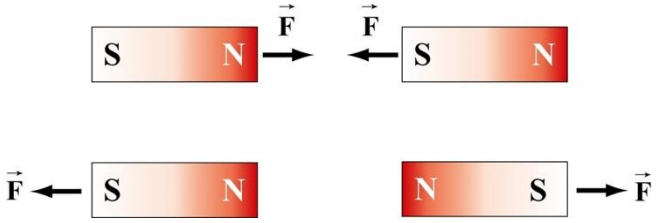

Figure 83: Magnets attracting and repelling

Unlike electric charges which can be isolated, the two magnetic poles always come in a pair. When you break the bar magnet, two new bar magnets are obtained, each with a north pole and a south pole. In other words, magnetic "monopoles" do not exist in isolation, although they are of theoretical interest. How it is defined the magnetic field **B**? In the case of an electric field **E**, it has already been shown that the field is defined as the force per unit charge:

$$\boldsymbol{E} = \frac{\boldsymbol{F_e}}{q} \tag{153}$$

However, due to the absence of magnetic monopoles, **B** must be defined in a different way.

A.3 The Definition of a Magnetic Field

To define the magnetic field at a point, consider a particle of charge q and moving at a velocity **v**. Experimental activity provided the following observations:

1. The magnitude of the magnetic force $\mathbf{F}_B$ exerted on the charged particle is proportional to both v and q.
2. The magnitude and direction of $\mathbf{F}_B$ depends on **v** and **B**.
3. The magnetic force $\mathbf{F}_B$ vanishes when **v** is parallel to **B**. However, when **v** makes an angle θ with **B**, the direction of $\mathbf{F}_B$ is perpendicular to the plane formed by **v** and **B**, and the magnitude of **F** is proportional to sinθ.
4. When the sign of the charge of the particle is switched from positive to negative (or vice versa), the direction of the magnetic force also reverses.

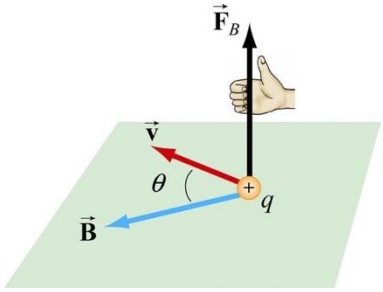

Figure 84: The direction of the magnetic force

The above observations can be summarized with the following equation:

$$\boldsymbol{F}_B = q\boldsymbol{v} \times \boldsymbol{B} \tag{154}$$

The above expression can be taken as the working definition of the magnetic field at a point in space. The magnitude of $\mathbf{F}_B$ is given by:

$$F_B = |q|vBsin\theta \tag{155}$$

The SI unit of magnetic field is the tesla (T):

$$1\ tesla = 1T = 1\frac{Newton}{(Coulomb)(meter/second)}$$

$$= 1\frac{N}{Cm/s} = 1\frac{N}{Am}$$

Another commonly used non-SI unit for **B** is the *gauss* (G), where 1T =10^4 G. Note that $\mathbf{F}_B$ is always perpendicular to **v** and **B** and cannot change the particle's speed *v* (and thus the kinetic energy). In other words, magnetic force cannot speed up or slow down a charged particle. Consequently, $\mathbf{F}_B$ can do no work on the particle:

$$dW = \boldsymbol{F}_B \cdot d\boldsymbol{s} = q(\boldsymbol{v} \times \boldsymbol{B}) \cdot \boldsymbol{v}dt = q(\boldsymbol{v} \times \boldsymbol{v}) \cdot \boldsymbol{B}dt = 0 \tag{156}$$

The direction of **v**, however, can be altered by the magnetic force.

A.4 Magnetic force on a dipole

As previously shown above, the force experienced by a current-carrying rectangular loop (i.e., a magnetic dipole) placed in a uniform magnetic field is zero. What happens if the magnetic field is non-uniform? In this case, there will be a net force acting on the dipole. Consider the situation where a small dipole **μ** is placed along the symmetric axis of a bar magnet, as shown in Fig. 83.

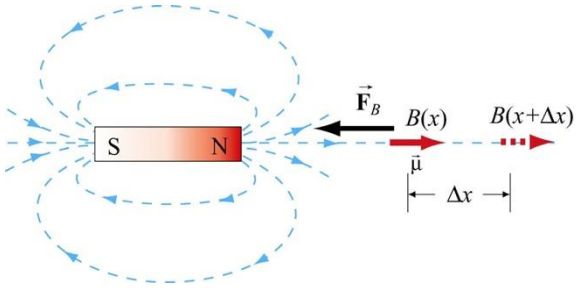

Figure 85: A magnetic dipole near a bar magnet.

The dipole experiences an attractive force by the bar magnet whose magnetic field is non-uniform in space. Thus, an external force must be applied to move the dipole to the right. The amount of force *F* exerted by an external agent to move the dipole by a distance Δ*x* is given by

$$F_{ext}\Delta x = W = \Delta U = -\mu B(x+\Delta x) + \mu B(x) = -\mu[B(x+\Delta x) - B(x)] \tag{157}$$

For small Δx, the external force may be obtained as

$$F_{ext} = -\mu \frac{[B(x+\Delta x) - B(x)]}{\Delta x} = -\mu \frac{dB}{dx} \tag{158}$$

which is a positive quantity since $dB/dx<0$, i.e., the magnetic field decreases with increasing x. This is precisely the force needed to overcome the attractive force due to the bar magnet. Thus

$$F_B = \mu \frac{dB}{dx} = \frac{d}{dx}(\boldsymbol{\mu} \cdot \boldsymbol{B}) \tag{159}$$

More generally, the magnetic force experienced by a dipole $\boldsymbol{\mu}$ placed in a non-uniform magnetic field $\mathbf{B}$ can be written as

$$\boldsymbol{F}_B = \nabla(\boldsymbol{\mu} \cdot \boldsymbol{B}) \tag{160}$$

where

$$\nabla = \frac{\partial}{\partial x}\boldsymbol{i} + \frac{\partial}{\partial y}\boldsymbol{j} + \frac{\partial}{\partial z}\boldsymbol{k} \tag{161}$$

is the gradient operator.

Bibliography

[1] G. Biernson, *"Principles of Feedback Control"*, vols. 1 and 2, John Wiley and Sons, NY, 1988.

[2] H. W. Bode, *"Network Analysis and Feedback Amplifier Design"*, Van Nostrand, NY, 1945.

[3] R. C. Dorf and R. H. Bishop, *"Modern Control Systems"*, Menlo Park, CA, 1997.

[4] P. Gernell, *"Guided Weapon Control Systems"*, 2nd ed. Pergamon Press, NY, 1980.

[5] I. M. Horowitz, *"Synthesis of Feedback Systems"*, Academic Press, NY, 1980.

[6] B. C. Kuo, *"Automatic Control Systems"*, 5th ed. Prentice Hall, Upper Saddle River, NJ, 1996.

[7] K. Ogata, *"Modern Control Engineering"*, 3rd ed. Prentice Hall, Englewood Cliffs, NJ, 1997.

[8] M. J. Sidi, *"Spacecraft Dynamics and Control"*, Cambridge University Press, NY, 1997.

[9] M. Athans and P. L. Falb, "*Optimal Control: An Introduction to the Theory and Its Applications*", Dover, 2006. Originally published in 1963.

[10] E. B. Lee and L. Markus,*"Foundations of Optimal Control Theory"*, Robert E. Krieger Publishing Company, 1967.

[11] D. G. Luenberger, *"Optimal Control"*, Introduction to Dynamic Systems. New York: John Wiley & Sons. pp. 393–435. 1979.

[12] R. W. H. Sargent, *"Optimal Control"*, Journal of Computational and Applied Mathematics. 124 (1–2): 361–371 2000.

[13] A. E. Bryson, *"Optimal Control 1950 to 1985"*, IEEE Control Systems Magazine. 16 (3): 26–33 1996.

[14] D. E. Kirk *"Optimal control theory an introduction*" 1970.

[15] I. M. Ross, "*A Primer on Pontryagin's Principle in Optimal Control"*. Collegiate Publishers. ISBN 978-0-9843571-0-9, 2009.

[16] R. M. Murray *"Control and Dynamical Systems Lectures*" California Institute of Technology 2006.

[17] S. C. Beeler "*state dependent riccati equation reulation of systems with state and control nonlinearities*" NASA and National Institute of Aerospace 2004.

[18] J.D. Pearson *"Approximation Methods in Optimal Control"*, Journal of Electronics and Control, Vol 13, pp. 453-465 1962.

[19] W.L., Garrand, N. H., McClamroch, and L. G. Clark, *"An Approach to Sub-Optimal Feedback Control of Non-linear Systems"*, International Journal of Control, Vol. 5 pp. 425-435 1967.

[20] J. A., Burghart, *"A Technique for Suboptimal Control of Nonlinear Systems",* IEEE Transactions on Automatic Control, Vol. 14, pp. 530-533 1969.

[21] A. Wernli and G. Cook, *"Suboptimal Control for the Nonlinear Quadratic Regulator Problem"*, Automatica, Vol. 11, pp. 75-84 1975.

[22] N.J. Krikelis, and K. I. Kiriakidis, *"Optimal Feedback Control of Non-linear Systems"*, International Journal of Systems Science, Vol 23, pp. 2141-2153 1992.

[23] J.R. Cloutier, C. N. D'Souza, and C. P. Mracek, *"Nonlinear Regulation and Nonlinear H_∞ Control Via the State-Dependent Riccati Equation Technique: Part 1. Theory"*, Proceedings of the First International Conference on Nonlinear Problems in Aviation and Aerospace, Daytona Beach, FL, 1996.

[24] Lee, J.H. and B. Cooley, *"Recent advances in model predictive control"*. In: Chemical Process Control - V. Vol. 93, no. 316. pp. 201–216b. AIChe Symposium Series - American Institute of Chemical Engineers, 1997.

[25] Qin, S.J. and T.A. Badgewell, *"An overview of industrial model predictive control technology"* In: Chemical Process Control - V. Vol. 93, no. 316. pp. 232– 256. AIChe Symposium Series - American Institute of Chemical Engineers, 1997.

[26] Garcia, C.E., D.M. Prett and M. Morari, *"Model predictive control: Theory and practice – a survey",* Automatica, 1989.

[27] Richalet, J., A. Rault, J.L. Testud and J. Papon *"Model predictive heuristic control: applications to industrial processes"* Automatica 14(5), 413–428, 1978.

[28] Cutler, C. R. and B. L. Ramaker, *"Dynamic matrix control a computer control algorithm"* Joint Automatic Control Conference San Francisco, California, 1980.

[29] L. Grüne, J. Pannek *"Nonlinear Model Predictive Control: Theory and Algorithms"* 2011

[30] A. Davies *"Oh look, more evidence humans shouldn't be driving"* Wired 2015.

[31] M. Buehler, K. Iagnemma, and S. Singh, *"The DARPA urban challenge: autonomous vehicles in city traffic",* springer, vol. 56, 2009.

[32] V. V. Dixit, S. Chand, and D. J. Nair, *"Autonomous vehicles: disengagements, accidents and reaction times",* PLoS one, vol. 11, 2016.

[33] Pepe, G., Carcaterra, A., "*VFC - Variational Feedback Controller and its application to semi-active suspensions"*, Mechanical Systems and Signal Processing, 76-77, pp. 72-92, 2016.

[34] Pepe, G., Roveri, N., Carcaterra, A., "*Prototyping a new car semi-active suspension by variational feedback controller",* Proceedings of ISMA 2016 - International Conference on Noise and Vibration Engineering and USD2016 - International Conference on Uncertainty in Structural Dynamics, pp. 231-245 2016.

[35] Pepe, G., Carcaterra, A., "*Semi-active damping by variational control algorithms"*, Proceedings of the International Conference on Structural Dynamic, EURODYN, 2014-January, pp. 1721-1727, 2014.

[36] Pepe, G., Carcaterra, A., "*A new semi-active variational based damping control",* MESA 2014 - 10th IEEE/ASME International Conference on Mechatronic and Embedded Systems and Applications, Conference Proceedings, art. no. 6935611, 2014.

[37] G. Pepe and A. Carcaterra, "*VFC - Variational Feedback Control applied to semi-active car suspensions"*, in NOVEM2015, 2015.

[38] Coppo, F., Pepe, G., Roveri, N., Carcaterra, A., "*A multisensing setup for the intelligent tire monitoring*" Sensors, Article number 576.

[39] Roveri, N., Pepe, G., Carcaterra, A., "*OPTYRE - A new technology for tire monitoring: Evidence of contact patch phenomena"*, Mechanical Systems and Signal Processing, Volume 66-67, 2016, Pages 793-810, 2016.

[40] Roveri, N., Pepe, G., Carcaterra, A., "*On line estimation of rolling resistance for intelligent tire"*, Proceedings of ISMA 2016 - International Conference on Noise and Vibration Engineering and USD2016 - International Conference on Uncertainty in Structural Dynamics2016, Pages 1725-1740, 2016.

[41] Haotian Cao, Xiaolin Song, and Zhi Huang, "*A Switched MPC Lateral Steering Controller Which Considered Tracking Quality and Handling Quality for Autonomous Vehicle"*, SAE Technical Paper 2017-01-1591, 2017.

[42] S. Çağlar Başlamişli , İ. Emre Köse & Günay Anlaç, "*Handling stability improvement through robust active front steering and active differential control"*, Vehicle System Dynamics, 49:5, 657-683, 2011.

[44] Nobuyoshi Mutoh, "*Driving and Bracking Torque Distribution Methods for Front-and-Rear-Wheel-Independent Drive-Type Electric Vehicles on Roads With Low Friction Coefficient"*, IEEE 2012-2-3, 2012.

[45] Haiping Du, Nong Zhang, Fazel Naghdy, "*Velocity-dependent robust control for improving vehicle lateral dynamics"*, Transportation Research Part C 19 454-468, 2011.

[46] Hartl, F. Richard, Sethi, P. Surresh, Vickson, G. Raymond, *"Survey of the maximum principles for optimal control problems with state constraints"*, Society for Industrial and Applied Mathematics, 1995.

[47] R. Bhattacharya, *"OPTRAGEN: A MATLAB Toolbox for Optimal Trajectory Generation"*, 45th IEEE Conference on Decision & Control, 2006.

[48] R. M. Murray, S. Shankar Sastry, *"Nonholonomic Motion Plannig: Steering Using sinusoids",* IEEE transactions on automatic control, 1993.

[49] P. Fiorini, Z. Shiller, *"Motion Planning in Dynamic Environments Using Velocity Obstacles",* The International Journal of Robotics Research, *1998*.

[50] Ji, J., Khajepour, A. Melek, W.W.; Huang, Y. *"Path planning and tracking for vehicle collision avoidance based on model predictive control with multiconstraints"*. IEEE Trans. Veh. Technol, 66, 952–964, 2017.

[51] N. Dal Bianco, E. Bertolazzi, F. Biral, M. Massaro, *"Comparison of direct and indirect methods for minimum lap time optimal control problems",* Vehicle System Dynamics, 2018.

[52] N. R. Kapania, J. Subosits, J. C. Gerdes, *"A Sequential Two-Step Algorithm for Fast Generation of Vehicle Racing Trajectories*", Journal of Dynamic Systems, Measurement and Control, Transactions of the ASME, 2016.

[52] G. Pepe, D. Antonelli, L. Nesi, A. Carcaterra, *"Flop: feedback local optimality control of the inverse pendulum oscillations"*, ISMA2018, Leuven, Belgium, 2018.

[53] T. I. Fossen, *"Handbook of marine craft hydrodynamics and motion control"* 2011.

[54] G. Webb, K. Mikyayev, O. Sokolov, *"A comparative assessment of various methods for recovering reusable lower stages"*, 67th International Astronautical Congress, Guadalajara, Mexico, 2016.

[55] L. Zhang, C. Wei, R. Wu, N. Cui: Fixed-time extended state observer based non-singular fast terminal sliding mode control for a VTVL reusable launch vehicle. Aerospace Science and Technology (2018).

[56] B.Tian, W.Fan, R.Su,Q.Zong, *"Real-TimeTrajectoryandAttitudeCoordinationControl for Reusable Launch Vehicle in Reentry Phase"*. IEEE Transactions on Industrial Electronics 2015.

[57] C.Min, D.Lee, K.Cho, S.Jo, J.Yang, W.Lee, *"Controlofapproachandlandingphasefor reentry vehicle using fuzzy logic*". Aerospace Science and Technology 2011.

[58] H. Chu, L. Ma, K. Wang, Z. Shao, Z. Song, *"Trajectory optimization for lunar soft landing with complex constraints"*. Advances in Space Research 2017.

[59] E. Paifelman, G. Pepe, F. La Gala, A. Carcaterra, *"Control of fluctuations of a tethered un- manned-underwater-vehicle"*. ISMA2018, Leuven, Belgium 2018.

[60] A. E. Bryson, "*Applied optimal control; optimization, estimation, and control"* A Blaisdell book in the pure and applied sciences, ,1969.

[61] L. S. Pontryagin, "*Mathematical Theory of Optimal Processes"* Classics of Soviet Mathematics. Taylor & Francis, 1987.

[62] A. Bacciotti and L. Rosier, "*Liapunov Functions and Stability in Control Theory"* Communications and Control Engineering. Springer Berlin Heidelberg, 2006.

[63] V. Utkin, J. Guldner, and J. Shi, "*Sliding Mode Control in Electro-Mechanical Systems"*, Second Edition Automation and Control Engineering. CRC Press, 2009.

[64] A. Isidori, "*Nonlinear Control Systems II"* Communications and Control Engineering. Springer London, 2012.

[65] A. J. Barry, P. R. Florence, and R. Tedrake, "*High-speed autonomous obstacle avoidance with pushbroom stereo"*. 2017.

[66] O. Khatib, "*Real-Time Obstacle Avoidance System for Manipulators and Mobile Robots"*. 1986.

[67] N. Ding and S. Taheri, *"An adaptive integrated algorithm for active front steering and direct yaw moment control based on direct Lyapunov method,"* Vehicle System Dynamics, vol. 48, no. 10, pp. 1193-1213, 2010/10/01 2010.

[68] X. Yang, Z. Wang, and W. Peng, *"Coordinated control of AFS and DYC for vehicle handling and stability based on optimal guaranteed cost theory,"* Vehicle System Dynamics, Article vol. 47, no. 1, pp. 57-79, 2009.

[69] I. Mehedi and M. S. Islam, "*Moon Landing Trajectory Optimization"*. 2016, pp. 120-286.

[70] H. Chu, L. Ma, K. Wang, Z. Shao, and Z. Song, "*Trajectory Optimization for Lunar Soft Landing with Complex Constraints"*. 2017.

[71] K. J. Åström and K. Furuta, *"Swinging up a pendulum by energy control,"* Automatica, vol. 36, no. 2, pp. 287-295, 2000/02/01/ 2000.

[72] M. F. Hamza, H. J. Yap, I. A. Choudhury, A. I. Isa, A. Y. Zimit, and T. Kumbasar, *"Current development on using Rotary Inverted Pendulum as a benchmark for testing linear and nonlinear control algorithms,"* Mechanical Systems and Signal Processing, Review vol. 116, pp. 347-369, 2019.

[73] D. Yurchenko and P. Alevras, *"Parametric pendulum-based wave energy converter*," Mechanical Systems and Signal Processing, Article vol. 99, pp. 504-515, 2018.

[74] C. Joseph, A. Zaferiou, L. Ojeda, N. Perkins, and L. Stirling, "*An optimal control model for assessing human agility trajectories"*. 2018, pp. 1-10.

[75] S. Jadlovska and J. Sarnovsky, "*A Complex Overview of Modeling and Control of the Rotary Single Inverted Pendulum System"*. 2013, pp. 73–85.

[76] P. Vartholomeos, C. Bergeles, L. Qin, and P. E. Dupont, *"An MRI- powered and controlled actuator technology for tetherless robotic interventions,"* The International Journal of Robotics Research, vol. 32, no. 13, pp. 1536-1552, 2013.

[77] Y.-L. Park et al., *"Real-time estimation of 3-D needle shape and deflection for MRI-guided interventions,"* IEEE/ASME Trans. on Mechatronics, vol. 15, no. 6, pp. 906-915, 2010.

[78] G. S. Fischer, A. Krieger, I. Iordachita, C. Csoma, L. L. Whitcomb, and G. Fichtinger, *"MRI compatibility of robot actuation techniques–a comparative study,"* in International Conference on Medical Image Computing and Computer-Assisted Intervention, 2008, pp. 509-517: Springer.

[79] A. Niebergall et al., *"Real-time MRI of speaking at a resolution of 33 ms: Undersampled radial FLASH with nonlinear inverse reconstruction,"* Magnetic Resonance in Medicine, vol. 69, no. 2, pp. 477-485, 2013.

[80] T. Nakada, *"Clinical application of high and ultra high-field MRI,"* Brain and Development, vol. 29, no. 6, pp. 325-335, 2007.

[81] M. D. Fox and M. E. Raichle, *"Spontaneous fluctuations in brain activity observed with functional magnetic resonance imaging,"* Nature Reviews Neuroscience, vol. 8, no. 9, pp. 700-711, 2007.

[82] P. Vartholomeos, M. R. Akhavan-Sharif, and P. E. Dupont, *"Motion planning for multiple millimeter-scale magnetic capsules in a fluid environment,"* in Robotics and Automation (ICRA), 2012 IEEE International Conference on, 2012, pp. 1927-1932: IEEE.

[83] L. Arcese, M. Fruchard, and A. Ferreira, *"Nonlinear modeling and robust controller-observer for a magnetic microrobot in a fluidic environment using MRI gradients,"* in 2009 IEEE/RSJ International Conference on Intelligent Robots and Systems, 2009, pp. 534-539: IEEE.

[84] G. Kósa, P. Jakab, G. Székely, and N. Hata, *"MRI driven magnetic microswimmers,"* Biomedical Microdevices, vol. 14, no. 1, pp. 165-178, 2012.

[85] A. T. Becker, O. Felfoul, and P. E. Dupont, *"Toward tissue penetration by MRI-powered millirobots using a self-assembled Gauss gun,"* in 2015 IEEE International Conference on Robotics and Automation (ICRA), 2015, pp. 1184-1189: IEEE.

[86] J. Leclerc, A. Ramakrishnan, N. V. Tsekos, and A. T. Becker, *"Magnetic Hammer Actuation for Tissue Penetration Using a Millirobot,"* IEEE Robotics and Automation Letters, vol. 3, no. 1, pp. 403-410, 2018.

[87] O. Felfoul, A. Becker, C. Bergeles, and P. E. Dupont, *"Achieving commutation control of an MRI-powered robot actuator,"* IEEE Transactions on Robotics, vol. 31, no. 2, pp. 387-399, 2015.

[88] A. Becker, O. Felfoul, and P. E. Dupont, *"Simultaneously powering and controlling many actuators with a clinical MRI scanner,"* in 2014 IEEE/RSJ International Conference on Intelligent Robots and Systems, 2014, pp. 2017-2023: IEEE.

[89] G.-Z. Yang et al., *"The grand challenges of Science Robotics,"* Science Robotics, vol. 3, no. 14, p. eaar7650, 2018.

[90] E. Diller, J. Giltinan, G. Z. Lum, Z. Ye, and M. Sitti, Diller, *"Six-degree- of-freedom magnetic actuation for wireless microrobotics,"* The International Journal of Robotics Research, vol. 35, pp. 114-128, 2016.

[91] S. Yim and M. Sitti, *"Shape-programmable soft capsule robots for semi- implantable drug delivery,"* IEEE Transactions on Robotics, vol. 28, no. 5, pp. 1198-1202, 2012.

[92] A. J. Petruska and J. J. Abbott, *"An omnidirectional electromagnet for remote manipulation,"* in Robotics and Automation (ICRA), 2013 IEEE International Conference on, 2013, pp. 822-827: IEEE.

[93] C. Pawashe, S. Floyd, and M. Sitti, *"Modeling and experimental characterization of an untethered magnetic micro-robot,"* The International Journal of Robotics Research, vol. 28, no. 8, pp. 1077- 1094, 2009.

[94] G. Z. Lum et al., *"Shape-programmable magnetic soft matter,"* Proceedings of the National Academy of Sciences, vol. 113, no. 41, pp. E6007-E6015, 2016.

[95] M. Sitti, Mobile Microrobotics. MIT Press, Cambridge, MA, 2017.

[96] W. Hu, G. Z. Lum, M. Mastrangeli, and M. Sitti, *"Small-scale soft-bodied robot with multimodal locomotion,"* Nature, vol. 554, no. 7690, p. 81-85, 2018.

[97] D. Folio, C. Dahmen, A. Ferreira, and S. Fatikow, *"MRI-based Dynamic Tracking of an Untethered Ferromagnetic Microcapsule Navigating in Liquid,"* International Journal of Optomechatronics, vol. 10, pp. 73-96, 2016.

[98] J. B. Mathieu and S. Martel, *"Steering of aggregating magneticmicroparticles using propulsion gradients coils in an MRI scanner,"* Magnetic Resonance in Medicine, vol. 63, no. 5, pp. 1336-1345, 2010.

[99] O. Felfoul, A. T. Becker, G. Fagogenis, and P. E. Dupont, *"Simultaneous steering and imaging of magnetic particles using MRI toward delivery of therapeutics,"* Scientific Reports, vol. 6, 2016.

[100] O. Erin, J. Giltinan, L. Tsai, and M. Sitti, *"Design and actuation of a magnetic millirobot under a constant unidirectional magnetic field,"* in Robotics and Automation (ICRA), 2017 IEEE International Conference on, 2017, pp. 3404-3410: IEEE.